Spring 1989

Low Speed Flowfield Characterization by Infrared Measurements of Surface Temperatures

Ehud Gartenberg
Old Dominion University

LOW SPEED FLOWFIELD CHARACTERIZATION BY INFRARED MEASUREMENTS OF SURFACE TEMPERATURES

by

Ehud Gartenberg
B.Sc. (May 1978), M.Sc. (October 1980) Aeronautical Engineering
Technion, Israel Institute of Technology, Haifa, Israel

A Dissertation Submitted to the Faculty of
Old Dominion University in Partial Fulfillment of the
Requirements for the Degree of

DOCTOR OF PHILOSOPHY

MECHANICAL ENGINEERING

OLD DOMINION UNIVERSITY
April 1989

Approved by:

A. Sidney Roberts, Jr. (Director)

Sushil K. Chaturvedi

Annageri V. Murthy

Gregory J. Selb

Surendra N. Tiwari

ABSTRACT

LOW SPEED FLOWFIELD CHARACTERIZATION BY INFRARED MEASUREMENTS OF SURFACE TEMPERATURES

Ehud Gartenberg

Old Dominion University, 1989

Director: Dr. A. Sidney Roberts, Jr.

An experimental program was aimed at identifying areas in low speed aerodynamic research where infrared imaging systems can make significant contributions. Implementing a new technique, a long electrically heated wire was placed across a laminar jet. By measuring the temperature distribution along the wire with the IR imaging camera, the flow behavior was identified. Furthermore, using Nusselt number correlations, the velocity distribution could be deduced. The same approach was used to survey wakes behind cylinders in a wind-tunnel. This method is suited to investigate flows with position dependent velocities, e. g., boundary layers, confined flows, jets, wakes and shear layers. It was found that the IR imaging camera cannot accurately track high gradient temperature fields. A correction procedure was devised to account for this limitation. Other wind-tunnel experiments included tracking the development of the laminar boundary layer over a warmed flat plate by measuring the chordwise temperature distribution. This technique was applied also to the flow downstream from a rearward facing step. Finally, the IR imaging system was used to study boundary layer behavior over an airfoil at angles of attack from zero up to separation. The results were confirmed with tufts observable both visually and with the IR imaging camera.

To my father, Dr. Alfons Gartenberg.

לאבא ד"ר אלפונס גרטנברג

And the Lord went before them by day in a pillar of cloud to lead them the way and by night in a pillar of fire to give light to them to go by day and by night.

Exodus XIII 21

ויהוה הלך לפניהם יומם בעמוד
ענן לנחתם הדרך ולילה בעמוד
אש להאיר להם ללכת יומם ולילה

שמות בשלח יג כא

ACKNOWLEDGEMENTS

Looking back at the wonderful time I had during my study program, it is my pleasant duty to thank my advisor Dr. A. Sidney Roberts, Jr. for encouraging me to pursue my own path of thought throughout this research, without compromising strongly held views of scientific rigor.

To Dr. Griffith J. McRee, associate dean for research at the College of Engineering and Technology at Old Dominion University, special thanks are due for according me the priviledge of being a part of the select research group he led along with Dr. Roberts. This group of aeronautical, electrical and mechanical engineers monitored by Ms. Debra L. Carraway from the Instrument Research Division, was supported by the NASA Langley Research Center for the development of advanced surface sensors for aerodynamic research. This research group offered its members the unequaled opportunity of doing research in an academic environment and simultaneously having access to the unique facilities at the NASA Langley Research Center.

To Mr. Harlan K. Holmes, head, Electro-Mechanical Instrumentation Branch and Dr. Bruce J. Holmes*, head, Flight Applications Branch, I offer my gratitude for their very generous support throughout my study program under grant NAG 1-735. To Ms. Debra L. Carraway, from the

*Presently, Assistant Chief for Aeronautics, NASA Headquarters, Washington, D.C.

Electro-Mechanical Instrumentation Branch, my thanks go out for her willingness always to lend help. She provided a gravity center for our research group, and many of its accomplishments should be credited to her initiative taking and management skills.

To the members of my dissertation committee, Drs. Chaturvedi, Murthy, Selby and Tiwari, each one of whom helped at times in his own way, many thanks for their special interest in this research.

My thanks to Ms. Rowena Pierce for the expert job she did typing the papers and the reports that originated from this work, and Ms. Diane Riddick for her efficient typing of this dissertation.

Finally, but by no means least, to my family and especially to my wife Rachel my love and gratitude for her patience, sacrifices, encouragement and support.

E. G.
January 1989

TABLE OF CONTENTS

LIST OF TABLES

LIST OF FIGURES

NOMENCLATURE

A	cross section area or circumferential area or constant
c	specific heat or constant in the power function freestream velocity distribution
c_f	skin friction coefficient
c_o	speed of light in vacuum
d	diameter
e	radiation emissive power
F	body force
Gr	Grashof number
h	convective heat transfer coefficient or Plank constant
I	thermal value
i	electrical current
k	thermal conductivity or Boltzmann constant or constant in the power function wall temperature distribution
ℓ	length
m	mass
N	photon emittance number
n	medium index of refraction or degrees of freedom
Nu	Nusselt number
P	number of the coefficients fit in the regression equation
p	pressure

Pr	Prandtl number
$\dot{q}$	heat generation rate
$\dot{q}_o''$	heat flux
R	pipe radius or electrical resistance
Ra	Rayleigh number
Re	Reynolds number
r	radial position
r^2	statistical coeffcient of determination
s	airfoil surface arc length
St	Stanton number
T	temperature
U	freestream velocity
x	distance from the leading edge

Greek Symbols

α	thermal diffusivity or angle of attack
δ	boundary layer thickness
ε	emittance
θ	reduced wall temperature
λ	radiation wavelength or constant in equation B.12
μ	absolute viscosity of the air
ν	kinematic viscosity of the air or photon frequency
ρ	density
σ	Stefan-Boltzmann constant or standard deviation
τ	time

Φ viscous dissipation function

Subscripts

a air

b black body radiation

c value based on chord length

D value based on diameter

f value at film temperature

v constant volume value

w wall or wood

x value based on distance from the leading edge

λ radiation spectral value

∞ freestream property

Superscripts

p value at time p

P constant in the power function freestream velocity distribution

γ constant in the power function wall temperature distribution

Chapter 1

INTRODUCTION

A quarter of a century after infrared imaging systems were introduced commercially, they are still very rarely used in aerodynamic research. The perception of these systems as an exotic tool limited their application to a few specific tasks. This reality is rooted in the history and in the everyday practice of aeronautical engineering. Since the primal interest is on the forces acting on a given body, pressure measurements come out as the natural measurements choice. This traditional approach is very useful in design studies that are mainly concerned with forces and moments impressed on the body by the external flow. However, it has little to offer when it comes to understanding and analyzing the interaction between the body and the viscous fluid that takes place through the boundary layer. When viewed globally, the two views are, of course, interconnected because the geometry of the body and the freestream velocity will determine not only the pressure-dependent forces but also the character of the boundary layer whether laminar, turbulent, or separated. In the case of attached boundary layer flow, its regime, whether laminar or turbulent, will determine the magnitude of the skin friction drag. However, a separated boundary layer completely alters the external flowfield about the body and totally changes the pressure distribution on it. Thus, there is the

need for a complimentary measurement technique that will offer insight into the whole picture of the fluid-body interaction.

In the same way that the pressure distribution reflects the momentum exchange between a fluid and a body, the temperature distribution reflects the energy exchange between the two. The difference is that the energy exchange process is related to all of the interaction aspects related to the external flow, the boundary layer flow and the substrate thermal diffusion. This aspect was recognized a long time ago and led directly to the introduction of hot-wire and hot-film gages for boundary layer research. However, these sensors (like most of the others) can provide information that can be related only to their locations, and this is one of their shortcomings. It is the capability of infrared imaging systems to scan large areas in a dynamic fashion, and produce quantitative results related to the surface temperature that make them an attractive alternative aerodynamic research tool. Unfortunately, conservative thinking played a major role in the failure to recognize the full research potential of these systems. The following literature survey will point to the very few applications the infrared imaging systems have seen. The survey is divided in two parts: aeronautical research establishments and universities. The big gap in financial, manpower and time resources between the two had a clear impact on the span of the research output.

1.1 Research at Aeronautical Establishments

1.1.1 Sweden

It seems that the first use of an infrared imaging system for aerodynamic research was made at the Aeronautical Research Institute of

Sweden by Thomann and Frisk* (1967) which used an IR system to measure surface temperatures on a model in a hypersonic wind tunnel and to deduce heat transfer rates from the data. For reducing the data, the material beneath the model's skin was assumed to be a semi-infinite slab. This allowed to use well-known analytical results from the heat-conduction theory (e.g., Eckert and Drake, 1972, pp. 168-176). This concept and the data reduction method was later adopted with little or no change at all by most of the groups working on this subject. However, Thomann and Frisk were not the first investigators to make the semi-infinite slab assmuption to deduce heat transfer rates from surface temperature measurements. This idea was borrowed from the phase change paint technique which later evolved into the thermographic phosphorescent paint technique. The interested reader can consult Jones and Hunt (1966) and Throckmorton (1972) regarding to the data reduction procedures originating from this technique.

1.1.2 France

The French at the Office National d'Etudes et de Recherches Aerospatiales (ONERA), were the first to realize the potential of infrared imaging systems to detect the laminar to turbulent boundary layer transition in the low subsonic regime (Bouchardy et al., 1983). This application is made possible by the fact that at the transition point there is an order of magnitude increase in the convective heat transfer rate. Thus, the transition line can be seen on an infrared

*Complete citations are found in the alphabetical list of references section.

imaging system display as a jump in the skin temperature going from low values in the laminar zone to high values in the turbulent zone, where the skin temperature is intially at the free stream temperature. Because at very low Mach numbers the temperature differences may not have been high enough to generate a good contrast on the IR thermography, the authors analyzed the raw data by applying digital image processing techniques. The effort was beneficial to other researchers as well, who made successful use of that capability (Schmitt and Chanetz, 1985). Lately, the effort at ONERA is concentrated on developing this method for use in cryogenic wind tunnels that will allow transition studies at higher Reynolds numbers in ground test facilities. A first effort in this direction was to carry-out experiments at 240K. A short and succinct enumeration of the difficulties encountered when making IR measurements in cryogenic environments is given by Seraudie et al. (1988). A further contribution to the use of infrared imaging systems was made by Balageas and Ory (1985), who reviewed the previously mentioned semi-infinite slab assumption and showed in which cases it can lead to significant errors. To refine the calculation methods, a technique was developed that takes into account the curvature of the wing, its skin thickness, as well as the thermal boundary conditions at the back of the skin.

1.1.3 West Germany

According to a survey by Mordoff (1988), the Deutsche Forschungs- und Versuchsanstalt fur Luft-und Raumfahrt (DFVLR) conducts an extensive and systematic experimental program designed to prepare a data base of flow regime characteristics of wings and airfoils. The program includes

both wind tunnel and flight tests (Quast, 1987), the infrared imaging system being the transition detection tool. Laminar flow data were recorded at Mach numbers varying up to 0.7, altitudes up to 10,000 m and sweep angles up to 23 degrees. Further tests are planned to be carried out in order to expand the range of the parameters of interest.

1.1.4 Japan

A study concerning the film cooling effectiveness of injection from multirow holes was carried out at the National Aerospace Laboratory by Sasaki et al. (1979). In this study, an infrared imaging system was used as a visualization means for the spreading of the injection fluid. All the temperature measurements were done by thermocouples and their results were compared with the thermographies in order to determine the cooling effectiveness of the various configurations being tested (simple versus multirow holes). The research was performed in support of jet engines turbine design efforts, but no directly applicable results have been reported.

1.1.5 U.S.A.

Most of the infrared imaging systems applications in aeronautical engineering reported by national laboratories are linked to the Space Shuttle program. The beginning goes back to the initial design phases of the shuttle when the prediction of the heat transfer rates during the entry phase were of major concern. The first experiments were performed by Compton (1972) at NASA Ames. This experimental program was very similar to that of Thomann and Frisk (1967) in Sweden, except for the fact that extensive use of computers was made for both data aquisition and data reduction. However, the bulk of the experiments were carried

out later on at Arnold Air Force Station in Tennessee. The initial study and set-up of the experimental system was done by Bynum et al. (1976). The study, which provided surface temperatures and heat transfer data, was still general in nature, the measurements being performed on a cone and a hemisphere at a Mach number of 8.0. Later, Stallings and Carver (1978) embarked on a program to make heat transfer measurements on Space Shuttle scale models, using an infrared imaging system and the phase-change paint method. Besides the obvious and original contribution to the Space Shuttle design, this group was the first to report the difficulties associated with infrared imaging system measurements. In a very extensive testing program, Boylan et al. (1978) evaluated the influence of the infrared imaging system optics on the overall performance. It was also showed that the system capability to map a step temperature change along the scanning direction is much poorer than across it. Tests were also carried out to determine the system spatial resolution using different size circular targets at the same temperature. Furthermore, an extensive measurement error analysis was carried out based on the work of Carter (1975). From all the aeronautical engineering groups using infrared imaging systems, the group at Arnold Air Force Station probably accomplished the most comprehensive analysis concerning the performance and limitations of this system in wind-tunnel testings. In two other papers, Stallings et al. (1979) and Stallings and Whetsel (1982) repeated some of the findings reported in the previous paper. Using the knowledge and facilities developed at Arnold Air Force Station, Martinez et al. (1978) performed heating experiments and measurements using an infrared imaging system on a 0.040 scale model of the Space Shuttle. These measurements

served the Rockwell Corporation in the design of the thermal protection system of the orbiter and can be considered as one of the very few but nontheless great contributions using an infrared imaging system in aeronautical engineering. Hender and Okabe (1983) made further use of that expertise to carry out heating measurements on a wedge type model made of an elastomer bonded to an aluminium base. It was found that for the wedge configuration, the semi-infinite slab assumption breaks down when deducing heat transfer data. Although the outcome could be predicted a priori, its extent could hardly be so, and for such cases an infrared imaging system may be the cheapest and fastest means to obtain quantitative data.

Two other applications relating to the Space Shuttle concern mapping surface temperatures during the entry phase. In one of them, the temperatures on the windward side of the orbiters were measured with a telescopic infrared imaging system mounted on an airborne observatory. The feasibility analysis was performed by Swenson and Edsinger (1977). Later, Chocol (1979) reviewed that study in the light of the following experiment objectives: (a) determine the actual heating rate distribution on the lower surface, (b) the location of the boundary layer transition, and (c) location and extent of flow separation in front of the control surfaces. Green et al. (1983) give a detailed description of how the system works together with a few representative results. However, no detailed presentation of the results or their processing followed up. Meanwhile, this research was cancelled, on financial grounds. In a second and completely separate experiment, the objective was set to be the measurement of surface temperatures on the leeside of the shuttle. In this case, an infrared

imaging system is mounted in a pod on the tail of the Space Shuttle Columbia, from where it scans the orbiter's wings and fuselage. This experiment is of interest because of the highly vortical nature of the separated flow over the wings which would impinge on the leeside surfaces. The final objective is to compare the measurements with results of CFD codes (Anon, Aviation Week and Space Technology, Dec. 7, 1987). As in the previous case, no results have yet been published from this unique experiment. Contributing to the design of the pod, heat transfer measurements were performed by Nutt (1979). The radiation estimation calculations were done by Myrick and Kantsios (1982); the description of the infrared imaging system is given by Myrick and Throckmorton (1985); and, the overall experiment description is provided by Throckmorton et al. (1985).

Two more noteworthy papers related to infrared imaging applications to flight testing are: one by Brandon, et al. (1988) from NASA Langley Research Center in which results relating to in-flight transition detection as well as mapping a vortex "footprint" on the airplane wing are described. Another paper is by Flaig (1977) from the Naval Air Systems Command, in which an infrared imaging system was used to map exhaust gases from a hovering VTOL aircraft and some helicopters. The results show the very complicated airflow patterns that develop in ground effect and at low speeds. No follow-up of this experiment could be found.

1.2 University Research

Applicable references from universities around the world are very meager. Most of the investigations were done in the United States. It

seems that Champagne et al. (1967) were first to use a microscope-pyrometer to make temperature measurements along a scaled-up hot-wire probe to determine the extent of the heat conduction to the supports. Meroney (1978) used an infrared imaging system to make heat transfer studies on model buildings in a wind tunnel. He proved the concept by estimating convection heat transfer coefficients but didn't proceed further because of lack of a suitable data processing system. Page et al. (1986) used an infrared imaging system to determine the temperature distribution in a heated jet at the stagnation point region. A similar research was done by Carlomagno and De Luca (1986) in Italy expanding the research to an array of jets and determining heat transfer coefficients from the temperature measurements. Finally, Spence (1986) used the infrared thermography to determine heat transfer coefficients on double wedge jet vanes used for missiles thrust vector control.

1.3 Perspective on the Literature Survey

The paucity of works documented in archival journals is a good indication regarding the immaturity of the infrared imaging method in aerodynamic research. Only three works, out of all those reviewed, have been documented in recognized scientific journals (e.g., Int. J. Heat Mass Transfer, J. Fluid Mechanics, AIAA J.). Furthermore, the relatively long reference list reviewed in this chapter is misleading with regard to its usefulness. The papers concerned with the shuttle entry measurements concentrate on technical descriptions of the systems and the projected experiments but give no results. The other papers either go into lengthy descriptions of the infrared imaging sytem itself, or use them to produce artificially colored pictures, while the

quantitative data was either acquired or heavily backed-up by thermocouples. Each one of the references adds a little bit of information, but none of them gives a complete picture, and this is the reason why every single reference that was found was listed. Of all the references, the most useful ones are those of Boylan et al. (1978) from Arnold Air Force Station, Tennessee, and Quast (1987) from DFVLR in West Germany.

1.4 The Present Work

Considering the potential applications of infrared imaging systems in aerodynamic research, there are at least two distinct paths that may be followed. The first and the simplest one is to follow the Reynolds analogy between the heat transfer and the skin friction. Temperature measurements can be performed in order to deduce Stanton numbers and subsequently skin friction coefficients. This approach works in fully developed laminar and turbulent flows, but it is not applicable in the region of the transition itself and in separated flows.

The second approach is more fundamental and goes back to the basics of the convective heat transfer. As is well known, the dimensionless heat transfer coefficient, the Nusselt number (Nu), is usually expressed as a function of the Reynolds number (Re) and the Prandtl number (Pr):

$$Nu = \text{Constant} \cdot Re^{m} Pr^{n} \tag{1.1}$$

For a constant Prandtl number, which is very frequently the case in aerodynamics, Eq. (1.1) can be rewritten as

$$\frac{h\,x}{k_a} = \text{Constant} \cdot \left(\frac{U \cdot x}{\nu_a}\right)^{m}, \quad 0<m<1 \tag{1.2}$$

Let's assume a constant properties flows, as is the case in the subsonic regime where the temperature doesn't change appreciably from place to place. Then, Eq. (1.2) can be expressed

$$h = h\ (U,\ x) \tag{1.3}$$

where h is the local heat transfer coefficient, x is the coordinate location of the point of interest on the configuration surface, k_a is the air conductivity, U is the local freestream velocity and ν_a is the air kinematic viscosity. This expression shows that the local heat transfer coefficient, h, between a surface and a surrounding flow is a function of the freestream flow velocity and the configuration geometry, x, if the air properties remain constant. On the other hand, the heat transfer coefficient h is defined by Newton's law:

$$\dot{q}_0'' = h\ (T_w - T_\infty) \tag{1.4}$$

where q_0'' is the local heat flux, T_w is the local wall temperature and T_∞ is the freestream static temperature.

Equations (1.3) and (1.4) are the basic formulae to be used for aerodynamic research using infrared imaging systems. Measurement of the surface temperature distribution on the body of interest with the IR imaging system, and knowledge of the geometry, the freestream temperature and eventually the heat flux, may provide enough data to deduce useful information about the flow-body interaction. The thrust of the present research utilized this second approach.

With the realization that IR imaging systems can produce more useful data in aerodynamic research than has been generally appreciated, this work explores the extent to which these systems can be made useful in advancing the understanding of aerodynamic flow phenomena. As a

result, the plan of research incorporated specific experimental objectives set out to produce an improved understanding regarding the detection of the low speed viscous interaction characteristics using IR imaging systems. Specifically, the following topics were identified to be pursued:

1. Feasibility and validation studies of the heated wire concept.

   This method calls for placing a very thin and very long heated wire perpendicular to the velocity vector of an airflow of interest. By tracking the temperature distribution along the wire with the IR imaging camera, it is possible to capture the main features of the flowfield. Furthermore, by using appropriate Nusselt number correlations, the velocity distribution perpendicular to the wire may be deduced.

2. Boundary layer development over a body of interest.

   Experiments and model analysis were planned so that by measuring with the infrared imaging system the wall temperatures of an actively heated body immersed in an airflow, the development of the thermal boundary layer can be tracked.

3. Detection of boundary layer flow regimes over airfoils and wings.

   The purpose in this experiment is to expand the applicability of infrared imaging systems to the detection of separation, beyond the detection of transition, e.g., Quast (1987).

The experimental work carried out under this program followed very closely the preceding stated purposes. Chapter 2 contains a brief review of an initial set of experiments that were aimed toward checking

the feasibility of the objectives with regard to the heated wire concept and tracking the boundary layer behavior by surface thermography. Chapter 3 is a short description of the infrared imaging system, emphasizing the IR imaging camera operation principles. Chapter 4 describes the evaluation of the heated wire concept using a laminar circular jet as a test case. Chapter 5 presents the experimental results and an analysis of the laminar, thermal boundary layer, which develops over a flat plate, using surface thermography. Chapter 6 is a study of the boundary layer regimes over a NACA 0012 airfoil from zero angle of attack up to separation, employing also tufts that could be observed both visually and with the IR imaging system. Finally, in Chap. 7 the conclusion from this research are drawn and recommendations for further work are made.

Chapter 2

THE PRELIMINARY EXPERIMENTS

Since the main objective of this research was to extend the use of infrared imaging systems to a few important aerodynamic subjects of interest, the first step was to carry out initial experiments, where the suitability of the measurement technique could be easily judged according to the results. The initial experiments and the results are described in detail in Gartenberg et al. (1987) and only the more interesting results are reproduced here. A review is made of the main ideas behind each experiment and of the way the results were evaluated.

2.1 The Heated Wire Technique

The first concept to be tested was the use of a thin, electrically heated wire as an air velocity detector. The idea was that by measuring temperatures along the wire while it is immersed in a flow with position dependent velocities, one may deduce the local velocities through Nusselt number correlations. This approach is useful when investigating shear flows, jets, boundary layer and confined flows, wakes etc. In such cases, the local heat transfer coefficient is mostly a function of the normal velocity component relative to the wire (Morgan, 1975); but even with this restriction, the method may be extremely useful to map flowfields unintrusively, since a 0.0762 mm (0.003") slightly heated wire will not have any significant influence on the surrounding flow.

Two experiments were performed in this category: mapping of an air jet and mapping of the wake behind a circular cylinder.

In the first experiment, the 0.0762 mm (0.003") heated wire was placed at 30 cm from the exit of a working heat-gun throwing cold air at 2.5 m/sec. The experimental set-up was identical to that shown in Fig. 4.3 with the addition that the wire was electrically heated. The measured temperature distribution along the wire was symmetrical with a minimum at the center of the jet, where the experimentally determined coefficient of heat transfer on the wire was in good agreement with the value predicted by a standard correlation (Morgan, 1975). Although the result was considered physically correct, the opinion was that the heat-gun flow was not controllable enough in order to produce a flow field suitable for a thorough investigation. As a result, the conclusions drawn from this preliminary experiment led directly to the laminar flow jet experiment described in Chap. 4.

In the second experiment, cylinder wakes were mapped using a heated wire placed downstream, and again the temperature distribution was found with the infrared imaging system. The set-up as installed in the 0.9x1.2 m (3'x4') low speed wind tunnel in which the experiments were carried out is shown in Fig. 2.1. A 10 cm diameter cylinder was tested at a Reynolds number of 90,000, the wire being placed at 5 and 10 diameters downstream from the cylinder. A second cylinder, 2 cm in diameter, was tested at a Reynolds number of 18,000, the wire being placed at 8, 16, 24 and 32 diameters downstream. In all cases, the qualitative results were self-consistent and agreed with the physical expectations. A sample result is shown in Fig. 2.2 where the temperature is plotted as a function of the lengthwise wire coordinate.

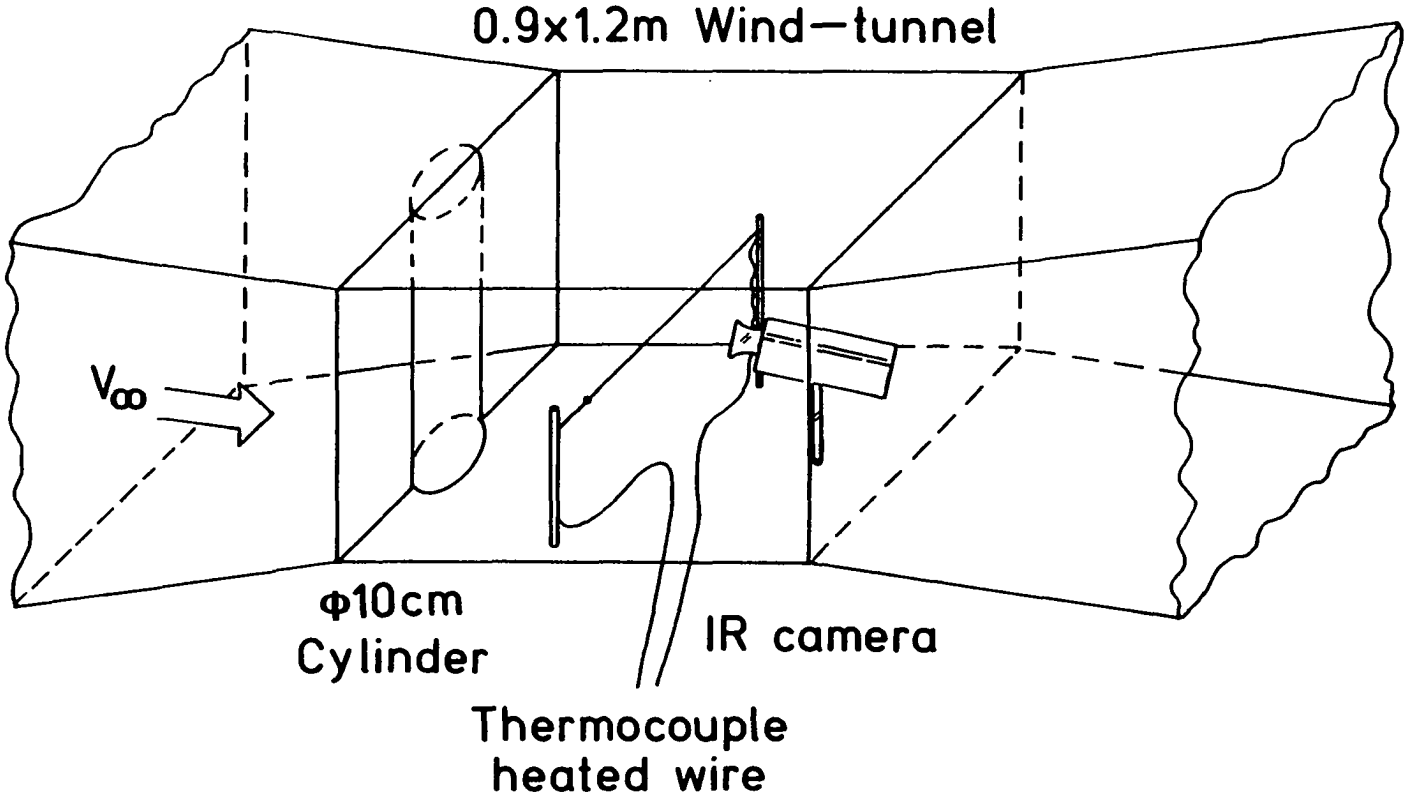

Fig. 2.1 Experimental layout for IR measurements of a heated wire in the wake of a cylinder

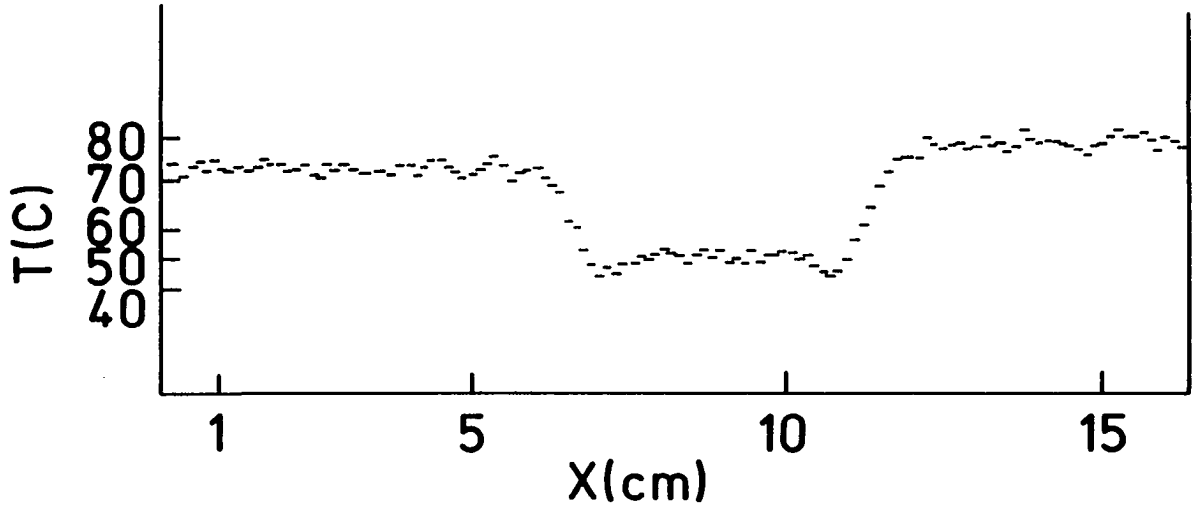

Fig. 2.2 The wake of a 10 cm diameter cylinder as captured on a heated wire placed 5 cylinder diameters downstream.
Re_D=90,000

According to Schmidt and Werner (Schlichting, 1968, p. 298), the heat transfer rate on the leeside of a cylinder, where the flow is separated, is equal to, or higher, than that on the windward side. The behaviour of the heat transfer rate in the separated flow area of the cylinder is dependent on the Reynolds number based on the cylinder diameter. In particular, just after the separation point, there is a jump in the heat transfer rate which is even more sensitive to the Reynolds number. These heat transfer features are of course washed downstream with the flow causing the wake to be a zone of very intense turbulent mixing with peak values at the edges, thus determining the temperature shape along the wire as shown in Fig. 2.2.

An important factor that arose during this stage of the research was the choice of the wire material. From the flowfield point of view, a thinner wire is more desirable. However, for lengths of wire herewith under consideration (tens of centimeters), a too thin wire may break easily. Also, a thin wire may not be resolved by the camera i.e., its surface may not be large enough in order to be projected on the whole area of the camera detector. Therefore, the infrared imaging system wrongly assumes that the photons reaching the detector come from an area which is equivalent at least to the instantaneous field of view of the camera for that focal distance, thus giving false lower temperature readings of the wire. (This aspect of the temperature measurements with the infrared imaging system will be addressed in greater detail in the next chapter).

At this point, it seems that increasing the wire diameter may be a partial solution to the spatial resolution problem of the IR imaging camera but this is not completely true. A larger wire will disturb the

flowfield, and also, as the wire diameter becomes larger, the spurious reflections from the surroundings to the camera start to play an important role in the signal to noise ratio the camera receives. A separate set of experimental runs with a variety of wire sizes revealed that at 0.381 mm diameter (0.015") the signal to noise ratio becomes unacceptably large. For example, the presence of people in the laboratory could be detected through their body heat reflection from the wire into the camera. Later it was found that smaller diameters were also desirable in order to minimize the heat conduction along the wire. Minimization of this factor is essential when velocity information is deduced from the temperature measurements. After trial-and-error experimentations, it was decided that a 0.0762 mm (0.003") diameter Chromel wire would be the best compromise for the present task. At this point yet another problem was to be faced involving the wire surface emittance calibration. The Chromel wire has a highly polished surface with a typical emittance of 0.05. However, using this value to determine temperatures with the IR imaging system will result, as previously noted, in lower than actual values because the wire is unresolved by the camera. In order to get true temperature readings, an "apparent emittance" lower than the actual should be used. The calibration procedure is described in Chap. 4. In this context, it should be emphasized that for optically unresolved targets, the distance from the camera determines the fraction of the instantaneous field of view the target will cover on the focal plane. Therefore, emittance calibrations for unresolved targets are valid only for the specific distance at which they were carried out.

The choice of the wire material should be made after a careful screening of its physical properties: the material should have a high electrical resistivity in order to dissipate enough heat to raise its temperature and be visible with the IR imaging camera. Also, the temperature coefficient of electrical resistance should be low so that the wire will uniformly dissipate the heat lengthwise, even if the temperatures vary locally. The material should be chemically stable, otherwise corrosion may change the emittance, and thus accurate continuous temperature measurements may not be possible. The coefficient of thermal expansion should be low in order to prevent elongation due to the heating that may cause vibrations. The wire thermal conductivity should be low in order to prevent equalization of the temperature along the wire through conduction. Finally, the wire thermal capacitance (the product of the mass per unit length with the specific heat) should be low in order to minimize the temperature time response to changes in local velocities. As already known, all these requirements led to the Chromel wire as the most suitable choice. On an absolute basis there are materials that fit better to the criteria established above. However, they fall into the category of rare metals, and thus their availability and price made their use in this case prohibitive.

Another problem that arose during the heated wire experiments was the background radiation interference. Since (as we have seen previously) the wire is unresolved by the camera, photons originating from the background surface will hit the detector together with the photons from the target wire. The problem is aggravated with increasing background temperature and spatial nonuniformity. To prevent problems

associated with background interference, its surface temperature should be kept at least uniform and preferrably low. All these factors indicate that the actual experiments should be run under the same background conditions at which the calibration was carried out. This is the reason why later, the laminar flow jet experiments (Chap. 4) were carried out against a uniform background made out of cardboard paper held at constant temperature by the air conditioning system of the laboratory.

2.2 Surface Measurements for Boundary Layer Research

A second series of preliminary experiments was concerned with detecting the laminar boundary layer development over a warmed flat plate. The experimental set-up is identical with that shown in Fig. 5.1 except for the fact that the leading edge was curved and not sharp as it should be in order to reproduce a Blasius type flow field. The experiments were carried out in a 0.9x1.2m (3'x4') wind-tunnel. It is a low speed, return circuit wind tunnel driven by a 100 HP electric motor. The surface was warmed by a Constantan wire closely wrapped three times chordwise around the plate with a duct tape covering it in order to ensure uniform emittance and a smooth surface. The original idea was to produce a constant heat flux flat plate. However, it became very quickly apparent that the boundary condition produced is of constant power heating type. The difference between the two is that in the former case a constant heat rate is dissipated into the freestream through the boundary layer, while in the latter the airflow, the surroundings and the substrate share the constant heat rate dissipated by the wires. The measured wall temperature distribution was considered

physically realistic due to its similarity to the constant heat flux case (Gartenberg et al., 1987), except for the fact that after an initial raise with the square root of the distance from the leading edge it leveled off, instead of continuing the initial trend (Kays and Crowford, 1980, p. 151). It was concluded that this behavior was the result of an ever increasing thermal involvement of the substrate, as the laminar boundary layer thickens and the convective cooling becomes less effective. At this stage, it was felt that this experiment should be revisited with a wedge type leading edge that would permit comparison of the experimental with analytic results. Further details are given in Chap. 5.

The last preliminary experiment was to monitor the wall temperature distribution for air flow over a rearward facing step to observe separated flow effects. The rearward facing step was produced by placing a right angle trapezoidal wedge on the flat plate previously mentioned, at 5 cm from the leading edge and parallel to it. The step height was 2 cm. The measured wall temperatures are reproduced in Fig. 2.3. Four features of the results were particularly encouraging. The first was that just at the foot of the step there is a jump in the wall temperature, that can be explained by the fact that at the corner, the flow has no velocity components and therefore, the convective heat transfer there should be minimal. The second feature was that at the point where the reattachment was believed to take place ($x \approx 15$ cm), the temperature passed through a local minimum. It is a well known fact that the heat transfer coefficient in such a flow is the highest at the turbulent reattachment point (Merzkirch et al., 1988), thus explaining the minimum temperature value there. The third feature was that

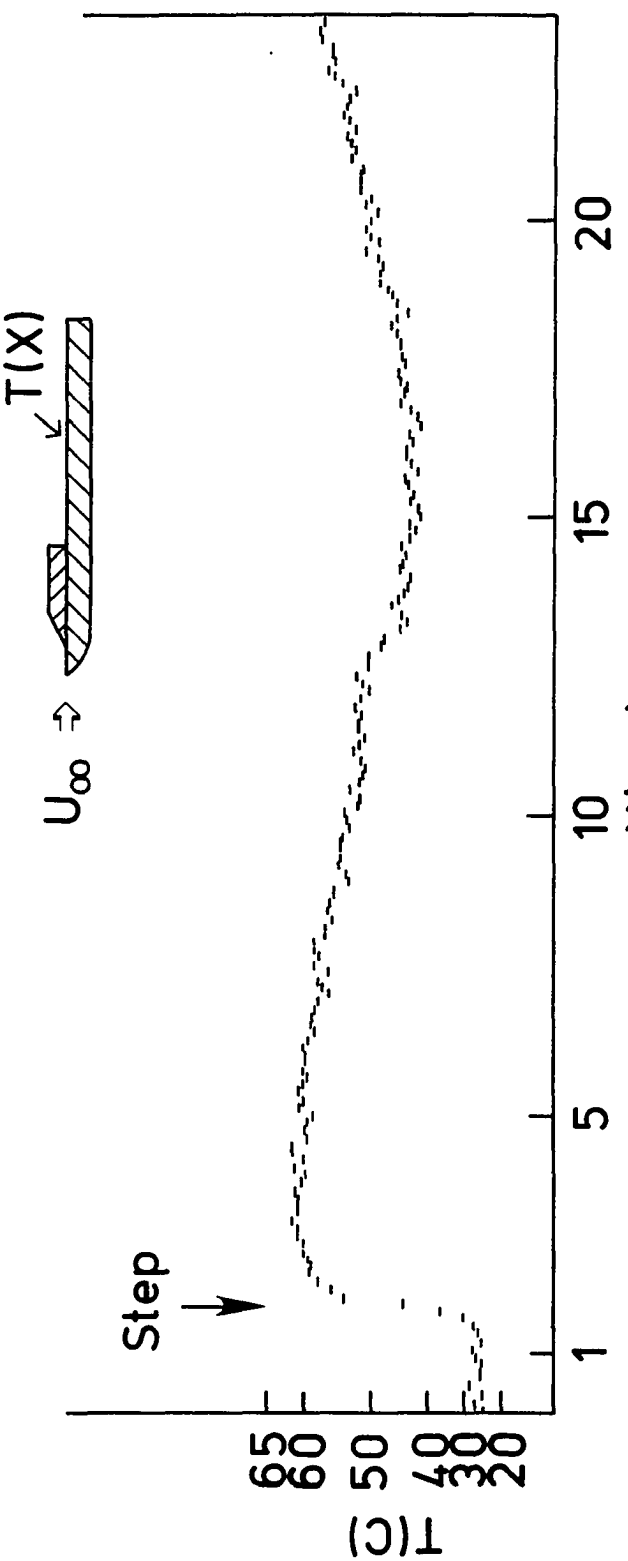

Fig. 2.3 Temperature distribution over a heated plate with a rear facing step. V_{air} =14 m/sec, Step height=2 cm

downstream from the reattachment point, the influence of the development of the turbulent boundary layer can be observed on the wall temperature distribution. The fourth and last feature of this experiment was that the assumed reattachment point occurred between six to seven step heights downstream of the step. For a Reynolds number based on the height of the step of approximately 17500, this result is in excellent agreement with the findings of Eaton and Johnston (1981). The results of this experiment showed that separated flows can be detected with infrared imaging systems by mapping the surface of interest. This conclusion led to the experiment described in Chap. 6 where the footprints of the airflow about a NACA 0012 airfoil were studied all the way from the fully attached regime at zero angle of attack up to the post stall regime.

Before proceeding further with the analysis of the main series of experiments, it is essential to explain the operational principles of the infrared imaging system, in order to understand its limitations from an aerodynamic research point of view.

2.3 Summary

The preliminary experiments carried out at this stage were critical to the definition and continuation of the main research tasks. Not only was it true that the bulk of the work carried out later stemmed directly from this stage, but also most of the instrumentation and measurement interpretation problems encountered when using infrared imaging systems in aerodynamic research, were crystalized during this stage.

Chapter 3

THE INFRARED IMAGING SYSTEM

A measurement system can be useful only to the extent that the operator understands the capabilities and limitations of his device. Although easy to use, the infrared imaging systems are very complex electro-optical devices and their output is influenced by a myriad of factors besides the target surface temperature. Since, in general, aeronautical engineers are not too familiar with these systems, it is the purpose of this chapter to review the main points of interest related to their performance.

3.1 Some Useful References

Infrared imaging systems work on the principles of radiation heat transfer. This type of heat transfer is based solely on the fourth power temperature difference between the body of interest and its surroundings, and takes place through electromagnetic radiation at wavelengths between 0.3μ to 50μ (where $\mu = 10^{-6}$ m), known as the infrared spectrum. As the name implies, the IR imaging systems detect this radiation and through electronic processing of the signals, produce an artificial video picture of the area scanned in which darker shades are associated with lower temperatures and lighter shades with higher temperatures.

The infrared imaging systems used for surface temperature measurements were developed during the sixties as derivatives of the military passive night vision systems. Although the requirements from the two types are somewhat different, the operational principles are the same. Lloyd (1975) gives an excellent overall account of the subject as viewed from his perspective as an engineer who worked for many years on research and development of such systems at Honeywell Inc. In a short note, Ohman gives a clear presentation of the different requirements from an IR system when it is used for night vision imaging versus imaging for temperature measurements, and the inherent changes to be made in the former in order to realize the latter. A state of the art review of infrared detectors is given by Levinstein (1977). Although written twelve years ago, the article is still relevant as some of the detectors described there are still in use. With regard to the quantitative determination of surface temperatures using an infrared camera, Hsieh and Ellingson (1977) propose a method that also includes the surface reflection problem.

Before proceeding with the description of the technical aspects of infrared imaging systems, it is worthwhile to draw attention to the proceedings of Thermosense V (1982), that contains a few papers concerned with the practical aspects of temperature measurements using these systems.

3.2 The Infrared Imaging System

The infrared imaging system used in this investigation was an AGA Thermovision® 782. The basic system consisted of the scanner and a black and white display unit that allows direct or relative temperature

measurements. The output from the scanner can be directly recorded on a modified vidicon recorder (VCR) for later playback. This device was of very little use mainly because of two limitations: frames could not be addressed individually; and a lack of a time base that could be recorded on the tape. The basic system was connected through a data link to a microcomputer BMC IF800 dedicated to the analysis of the thermographies. A Disco® 2.0 software package is used for the image processing and completely occupies a 5 1/4" floppy disk in a read-only storage mode. Up to 36 individual images can be stored on a second floppy disk in a read and write access storage mode. The user has the option to record single images, or an image that is the average of several images, or to record a series of up to 16 images at a time at a frequency of 1.5 Hz or lower. A key feature of this program is the gradual assignment of eight tones of artificial colors (from black through blue, green, red, etc. to white), for corresponding grey shades in the original image, thus producing an artificial sensation of the temperatures in the scanned field. The main advantage of such a system is the cross-hair cursor that can easily be moved on the screen and allows the operator to get precise temperature readings at defined locations of interest. Although the Disco® 2.0 was written specifically for the BMC IF800 computer, and although the latter has a quite obsolete architecture, together they make-up a quite versatile system that offers an abundance of processing options, from which only the main ones have been reported here.

3.3 The Infrared Imaging Camera

The infrared imaging camera converts electromagnetic thermal energy radiated from the scene contained in its field of view, into electronic

video signals. These signals are electronically amplified and transmitted to the black and white display unit where the signals are further amplified, and the resulting image is displayed on the screen. The camera, or the scanner, comprises the following main subsystems:

(a) Electro-optical scanning mechanism

(b) Infrared detector attached to a liquid nitrogen Dewar flask

(c) Control electronics and preamplifier.

As can be seen in Fig. 3.1, the scanning mechanism consists of two mutually perpendicular prisms. The horizontal one rotates at three rps. Its optical output is passed to the vertical one which rotates at 300 rps. Thus, we get the "lines" and the "columns" of the scanned scene, which is called a field. Each field has 70 active lines (100 all together) and 130 active columns. For visual display reasons, the vertical and horizontal motors are synchronized in such a way that four fields produce one interlaced frame. With a scanning rate of 25 fields per second, 25/4 completely interlaced picture frames per second are thus obtained. The output from the vertical prism is focused onto the single element semiconductor detector, which is located in the wall of a Dewar chamber, and is maintained at 77K by liquid nitrogen. The detector produces an electronic output proportional to the incoming infrared radiation. After amplification, the signal is sent via a cable to the display unit, where absolute or relative temperature measurements can be made.

Throughout this research, the data was aquired only in the "field" mode, to take advantage of the higher scanning rate associated with that

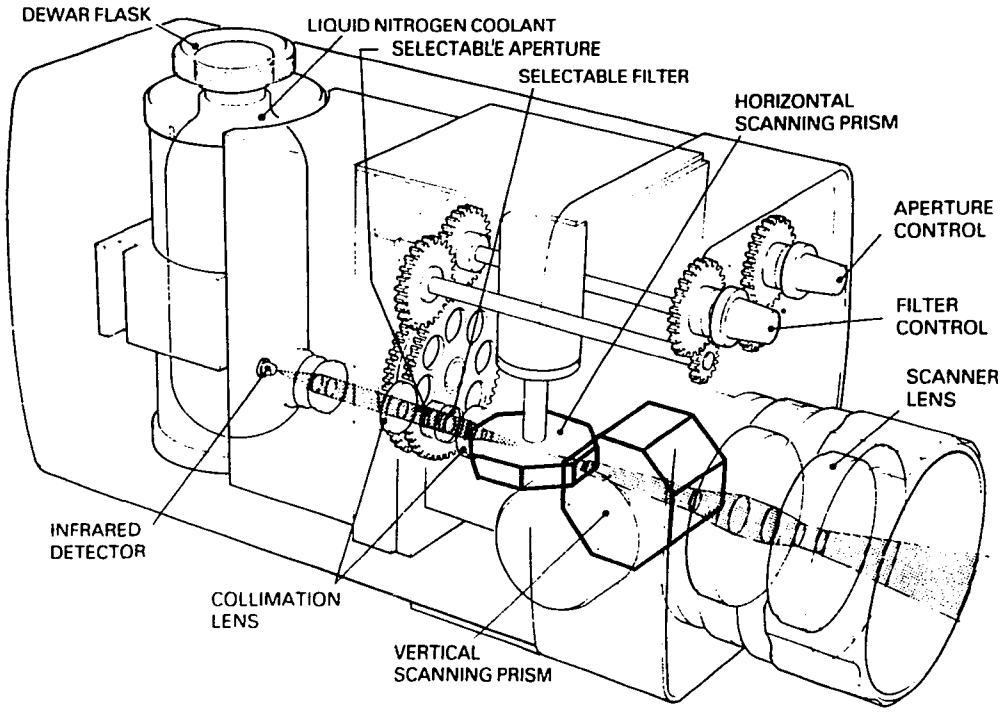

Fig. 3.1 Infrared imaging camera cutaway
AGA Thermovision® 782

mode (25 images per second). More information about the system and the way it operates can be found in the AGA Thermovision® 782 Operating Manual (1984).

3.4 Physical Aspects of the Camera Operation

The operational characteristics of an IR imaging camera are largely dependent upon the detector characteristics and performance. Each kind of detector has its own narrow range of detection in the IR spectrum according to its chemical composition. Therefore, it is important to find out a priori whether the expected targets do have a radiation component that matches the detector characteristics. Secondly, since the atmosphere does not transmit the IR radiation all along its spectrum, the matching of the detector has also to fit the "atmospheric windows". This is the term used to denote the wavelength of IR radiation for which the atmosphere is transparent. In the present case, the sensor is made of Indium Antimonide (InSb), which is classified as a semiconductor element with a spectral response in the 1.7 to 5.8 μ range. However, the spectral response of the camera (as a system) is purposely reduced to the 3.5 to 5.6 μ due to the special coatings of the objective lens. Its operational temperature detection range is between -20°C to 850°C. The field of view (FOV) of the objective lens of the camera is 20°. The area projected at any one time on the detector is subtended by an angle of 0.0035 radians, which is also called the instantaneous field of view (IFOV). With a scanning rate of 25 fields per seconds, each field having 100 lines and 130 columns, the scanning rate is 325,000 IFOV/sec, or 3 μ sec per IFOV. With a time constant of approximately 0.2 μ sec (Levinstein 1977), the InSb detector matches the

camera needs. Since the camera design probably started from the detector characteristics, it is clear that they are the bottleneck for the upper limit of the scanning rate.

The InSb is a linear photon counting photovoltaic detector. These detectors are sensitive to the number of photons hitting them (rather than their energy), once their energy exceeds the energy threshold of the semiconductor material. In general, the effect of cooling the detector is to decrease this cut-off wavelength. The calibration curves of the IR imaging camera can be derived directly from the Planck's formula (Sparrow and Cess 1978, p.6)

$$e_{b\lambda}(T) = \frac{2\pi hc_o^2}{n^2 \lambda^5 [\exp(hc_o/n\lambda kT)-1]} \qquad (3.1)$$

where $e_{b\lambda}$ is the spectral emissive power of the black body radiation, h is Planck's constant, k is Boltzmann's constant, c_o is the speed of light in vacuum, n is the refraction index of the medium, λ is the respective wavelength and T is the absolute temperature. When Planck's formula is divided by the energy of a single photon $h\, c_o/\lambda = h\nu$ we obtain the spectral photon emittance for a blackbody $N_{\lambda b}$

$$N_{\lambda b} = \frac{2\pi c_o}{n^2 \lambda^4 [\exp(hc_o/n\lambda kT)-1]} \qquad (3.2)$$

From here, one gets directly the formula commonly used to express the calibration curve behavior,

$$I = \frac{A}{C \exp(B/T-1)} \qquad (3.3)$$

where I is the "thermal value" corresponding to temperature T and A, B, and C are constants (AGA, 1984). The thermal value I is measured in isothermal units (IU) which is a practical unit of measurement. The relationship between the thermal value and the received photon flux is linear. However, the relationship between the thermal value and the object temperature is obviously non-linear.

Finally, it should be mentioned that the radiation coming from a certain spot to the detector has three components: object radiation, reflected radiation and atmospheric participation. The camera has no way to distinquish between the three, and its output is an "integrated" one. It is indeed the duty of the operator to account for the various contributions causing the final output signal. As a corollary, it can be said that the measurement of temperatures using infrared imaging techniques is not a method that can be applied without expert attention to detail.

3.5 The Resolution Problem

The essence of a successful design for an infrared imaging system lies in the answer to the resolution problem. This problem has two aspects: the minimum resolvable temperature difference and the slit response function.

The minimum resolvable temperature difference (MRTD) is the result of a standardized test designed to evaluate the camera performance in this respect. The test target is a plate with four slits of varible width which is placed in front of another uniform plate. The temperature of both plates is independently adjustable. By varying the width of the slits and recording the respective temperature difference between

the plates, where the pattern becomes indistinquishable to the camera, one obtains a graph as shown in Fig. 3.2. The lowest point of the curve is the temperature difference at zero slit spatial frequency and represents the system sensitivity. The test is usually run at 30C, and for the present system, this sensitivity is about 0.2C. A second parameter is the highest possible resolution, which can be represented by a vertical line that is asymptote to the rising curve. To understand this behavior, one must understand the slit response function (SRF) of the camera. As it can be seen in Fig. 3.3a, the test target in this case consists of a temperature adjustable plate covered by another plate with a slit of a variable width. As the slit width is increased, so is its angle as viewed from the detector. This angle can be less, equal or greater than the field of view of the detector which is called the instantaneous field of view (IFOV). Slits that are smaller than the IFOV are called unresolved. When the camera scans an object that is unresolved, the radiation falling on the detector comes partially from the target and partially from the surroundings. As a result, as shown in Fig. 3.3b, the signal modulation from an unresolved slit is smaller than one coming from a resolved slit. As the slit width increases, so does its angle and the signal modulation, until the detector response reaches a plateau characteristic to resolved targets, as shown in Fig. 3.3c.

With the above background information, the behavior of the curve for the minimum resolvable temperature difference, shown in Fig. 3.2 may be understood. As the slits frequency increases, the modulation of each individual slit decreases, and one needs a higher temperature difference between the two plates in order to get a minimum modulation of the signal, enough to be detected by the detector.

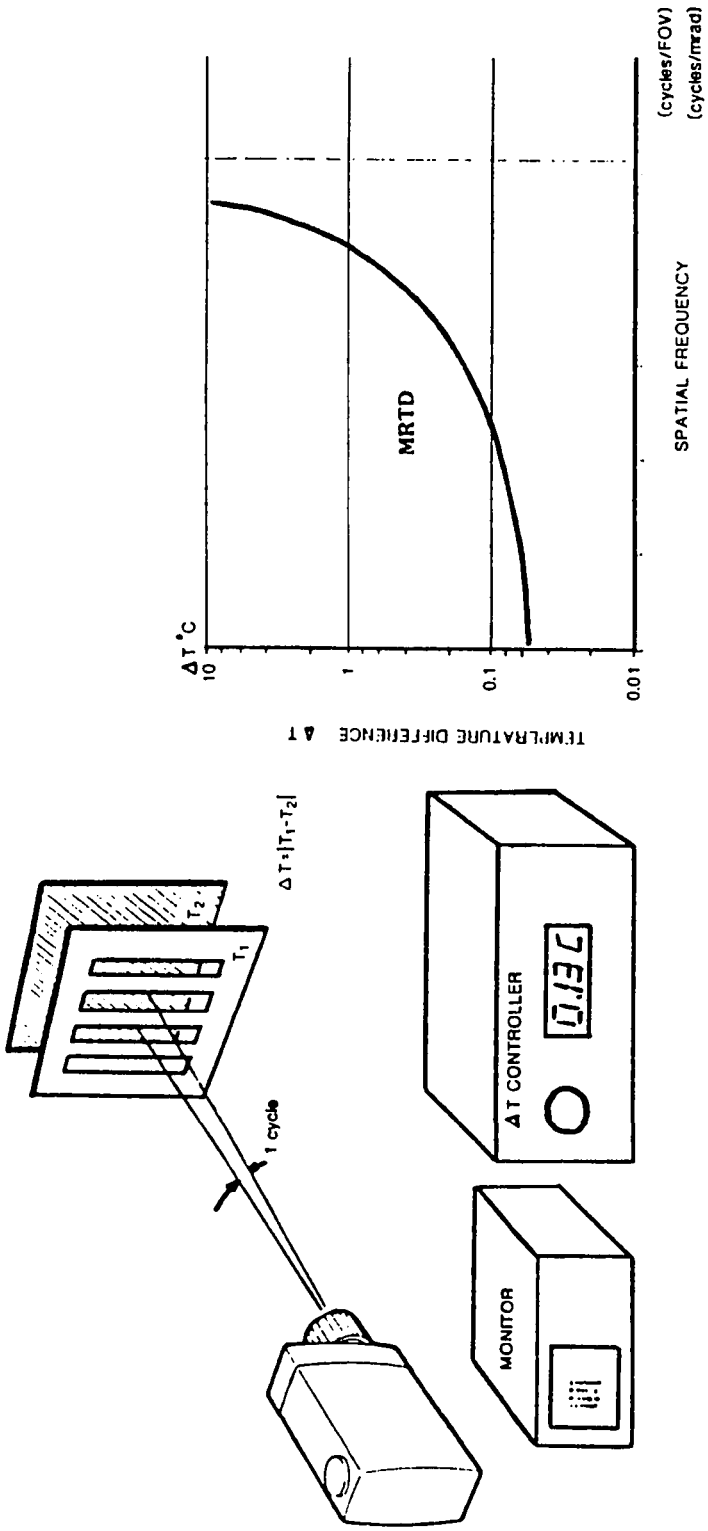

Fig. 3.2 The minimum resolvable temperature difference test set—up and result (after Ohman)

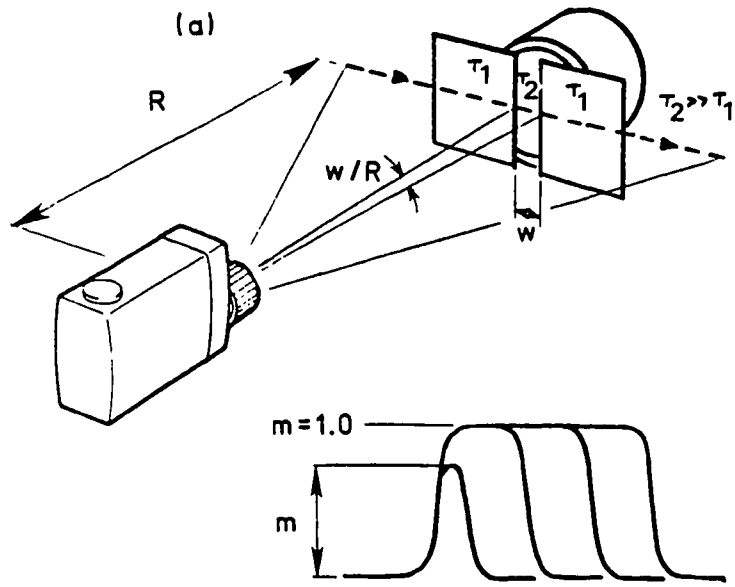

(b) LINE SCAN VIDEO SIGNAL

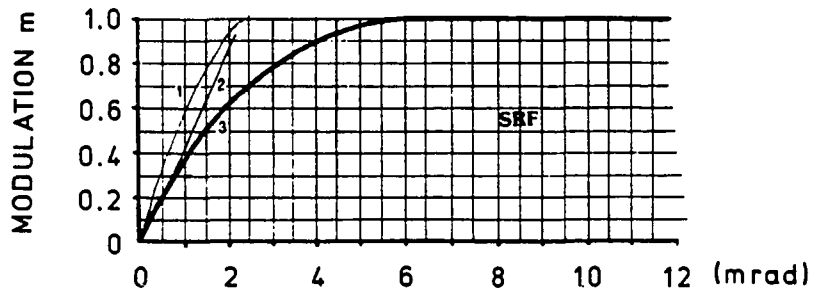

(c) SLIT ANGLE w/R

1) Ideal SRF for circular detector
2) Ideal SRF for square detector
3) Typical measured SRF

Fig. 3.3 The slit response function test set-up and results (after Ohman)

From the practical point of view, this behavior suggests that the IR imaging camera may have difficulty in tracking high gradient temperature fields. Visually, this may be explained in the following way: Let's approximate the temperature distribution of a target by a series of constant temperature strips. As the temperature gradient increases, the width of these strips decreases and therefore their individual modulation decreases. Thus, as the IR imaging camera scans such an object, the error of the measurement will increase. In fact, the graph showing the dependency of the error in the measurement of a high gradient temperature field will look very much like that in Fig. 3.2, with the abscissa representing the gradient of temperature and the ordinate representing the mesurement error.

Before concluding this chapter, it is well to remember that the infrared radiation includes diffraction behavior, which is typical to electromagnetic phenomena. This means that the signal modulation will not be full even if the target is just resolved, since energy from the surroundings will still reach the detector. As a rule of thumb, the target area to be scanned for full modulation should be at least three times that of the instantaneous field of view (IFOV).

3.6 Summary

Use of infrared imaging systems requires the understanding of their principles of operations in general and the characteristics of the specific system which is placed in service. These systems do not measure the temperature of the object being scanned. Rather they have a voltage output which is proportional to the photons number coming from the target and hitting the detector. This input may be attenuated by a

multitude of factors, among them the surface emittance and the atmospheric attenuation. Therefore, in extracting quantitative data from system readings, it is the responsability of the experimenter to account for all the possible influences that may have influenced the result. Also, it was shown that the IR imaging systems may experience difficulties in mapping high temperature gradient fields.

Chapter 4

THE LAMINAR FLOW JET EXPERIMENT

Following the promising preliminary evaluation, the next step was to assess the capability of the IR imaging method to produce relevant quantitative results. For this purpose the research was focused on the mapping of a laminar flow air jet using the heated wire concept, which is shown in Fig. 4.1. The ordered behavior of this flow offered the convenience of comparing well understood experimental and theoretical results. The measured temperatures were used in conjunction with heat transfer correlations in order to deduce the air velocity distribution within the jet. In particular, this flowfield offered the opportunity to test the capability of the system to map high gradient temperature distributions.

4.1 The Experimental Set-up

In this experiment, the infrared imaging camera scanned the temperature distribution along a thin, electrically heated Chromel wire, a small part of which was placed diametrically at the exit of a pipe from which a laminar flow air jet discharged into the atmosphere. The camera was placed at a distance of 0.5 m from the wire. At this distance, it has a spatial resolution of 0.0034 radians and its field of view was 15x15 cm. As shown in Fig. 4.2, the Chromel wire, 0.0762 mm in diameter (0.003"), was part of a Chromel-Constantan thermocouple assembly that offered the opportunity to perform in-situ calibration for

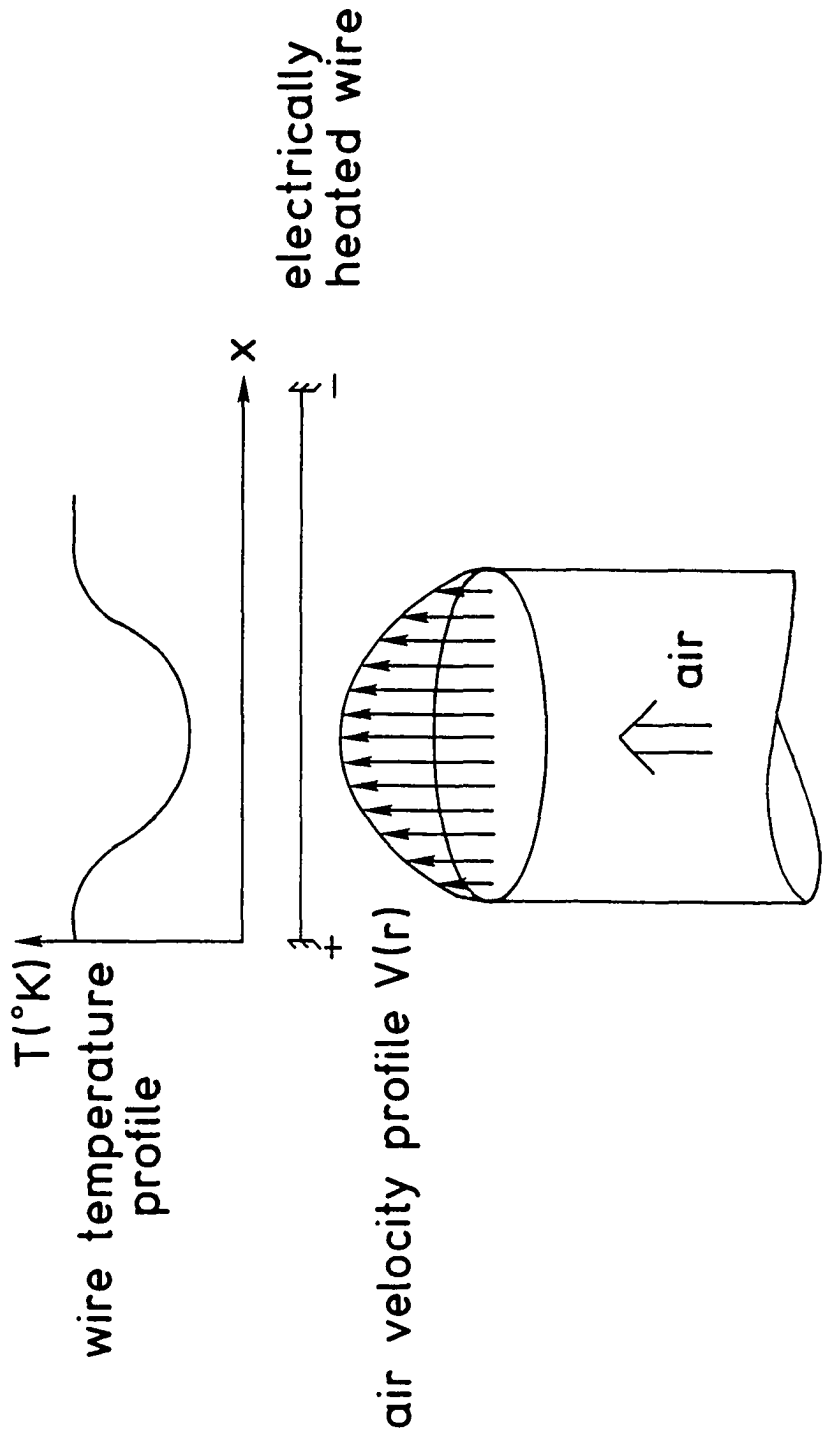

Fig. 4.1 Enlarged schematics of the heated wire laminar flow air jet experiment

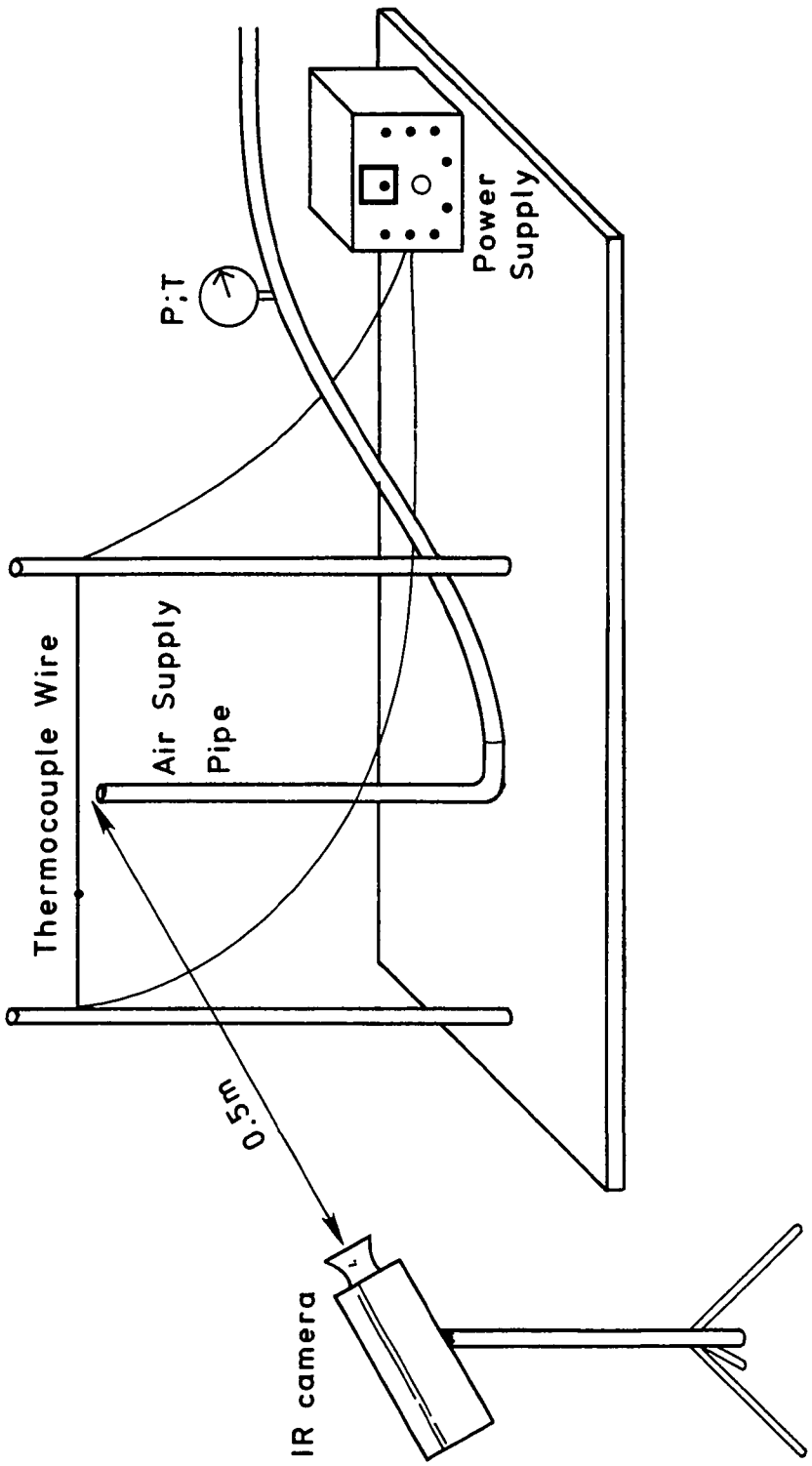

Fig.4.2 Set—up for the heated wire laminar jet experiment

the surface emittance value. The knowledge of this value is critical when the objective is to determine surface temperatures and air velocities from infrared thermographies.

Calibrations for surface emittance properties are usually quite tedious processes. As shown in Fig. 4.3, the calibrations were performed by aiming a working heat-gun at the wire segment including the thermocouple junction, thus getting a direct reading of the wire temperature. Previously, the heat gun position was carefully adjusted in order to get locally a uniform (flat) temperature distribution of the wire in the region adjacent to the thermocouple junction, within ±0.2°C. The hot air temperature distribution in that region was double checked for uniformity, independently, with another thermocouple, and the mean hot air temperature was measured with a mercury thermometer. The accuracy of each of these devices was ±0.2°C. In parallel, the wire was thermographed by the AGA system and the temperature of the Chromel wire adjacent to the thermocouple junction was analysed with the Disco II® software on the dedicated microcomputer. The emittance input of the wire was adjusted until the temperature result from the computation equaled that of the thermocouple readout. Since the Disco II® computer program that was used to analyze the thermographies could read only emittance values down to two decimal digits, recourse was made to the atmospheric transmittance factor to finally adjust the emittance value. This result was checked with another software package supplied by AGA and run on an HP-41 CV programmable calculator with identical results. Thus, for the 0.0762 mm (0.003") diameter Chromel wire at 0.5 m distance from the IR imaging camera and moderately overheated (say around 350K), this apparent emittance has a value of 0.0244, as

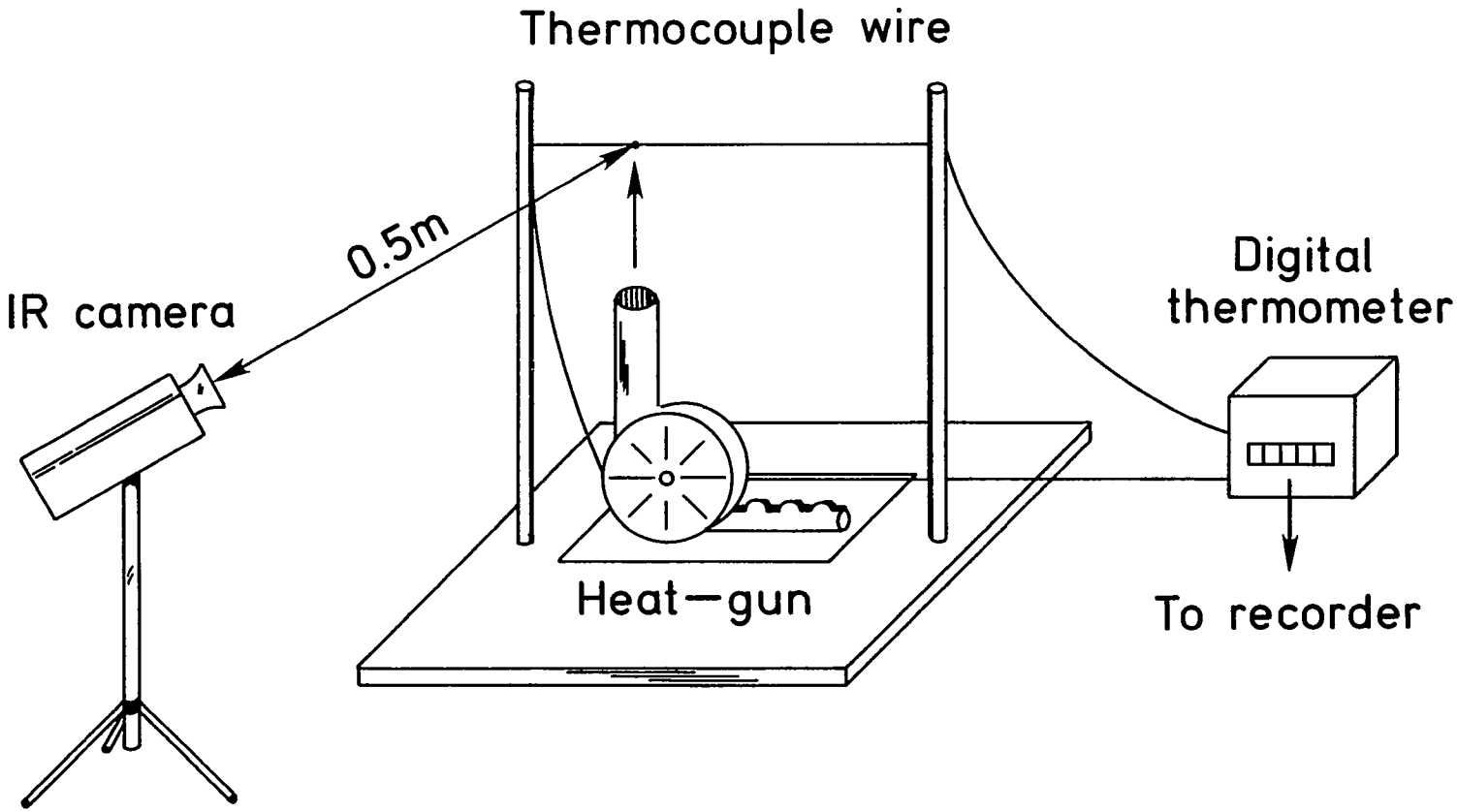

Fig. 4.3 Set—up for wire emittance calibration.

indicated by the HP 41 CV calculator run program. With the Disco II® software, the emittance value was set at 0.03 and the transmittance at 0.82, to get an equivalent apparent emittance value of 0.0246. The sequence of steps for one such wire calibration is given in Table 4.1.

The Chromel wire length was 40 cm and the Constantan wire length was 10 cm. The thermocouple assembly was hung between two vertical bars 50 cm apart. The length to diameter ratio of the Chromel wire was 5250:1, so that the influence of the heat conduction (on the central area of interest) to the supports can be neglected. The wire was heated by a D.C. electric current passing through it. A cardboard screen was placed behind the wire to provide a uniform background for the IR imaging camera (see Sec. 2.1). As shown in Fig. 4.2, the pipe exit was placed at 2 mm distance from the heated wire, at the center of the Chromel section. The air-supply pipe had a 13.3 mm (0.545") internal diameter, a 15.9 mm (0.625") outer diameter and a straight section of 80 cm, thus getting a length to diameter ratio of 60. The nominal mean air velocity in the pipe was about 2 m/sec, and the corresponding Reynolds number based on the pipe diameter was about 1700, which is well under the critical Reynolds number of 2300. The length of the straight section was considered enough to provide fully developed laminar flow inside the pipe, just before its mouth. According to an approximate analysis by Schiller (Schlichting, 1968, p. 231) a length to diameter ratio of 49 could be considered satisfactory for the actual Reynolds number. According to another analysis by Langahaar (Kays and Crawford, 1980, p. 67), this design is acceptable within a margin of 5% off the ultimate coefficient of friction for fully developed flow. Three fine-mesh screens, (each rotated at 45° with respect to the others) were

Table 4.1 Calibration of the Apparent Wire Emittance with the Disco II® Computer Program

T_{wire} (°C) actual	Emittance Disco II®	Transmittance Disco II®	T_{wire} (°C) Disco II®	Emittance apparent
75.4	0.05	1.00	56.1	0.050
75.4	0.04	1.00	61.4	0.040
75.4	0.03	1.00	69.4	0.030
75.4	0.03	0.90	72.3	0.0270
75.4	0.03	0.85	74.0	0.0255
75.4	0.03	0.83	74.8	0.0249
75.4	0.03	0.82	75.2	0.0246
75.4	0.03	0.81	75.5	0.0243

placed at the entry of the straight section of the tube in order to break down any large vortices or non-uniformities that might exist in the flow. The air was supplied by a standard 100 psi low-pressure system (of the type that is commonly in use in laboratories and workshops). The air mass-flow rate was adjusted using a pressure regulator and by taking total pressure and temperature measurements upstream from a sonic nozzle with the suitable correction for its discharge coefficient. The throat diameter of the nozzle was 0.8 mm (0.0315"), and the nominal absolute air pressure upstream the nozzle was 304510 N/m^2 (31 psig). This pressure was adjusted to account for the nozzle discharge coefficient and variations in the air temperature, to get a nominal centerline velocity of 4 m/sec, determined from Pitot-tube measurements (see Sec. 4.3).

4.2 The Experiment Description

The experiments were carried-out at four different levels of heating corresponding to dissipation rates of 3.47, 4.71, 6.17 and 9.33 watts/m of Chromel wire. The area of interest i.e., that part of the wire that was directly cooled by the air jet, was about one tenth the field of view of the IR imaging camera. This design was made purposely to evaluate the system's capability to resolve localized temperature changes in the field of view.

For each separate experiment, nine consecutive frames were taken at a rate of 0.7 Hz and their average was stored as a single frame on the computer's diskette for later analysis. During each experiment, the range and level of the camera were carefully set according to the target luminosity in order to minimize the background noise, and at the same

time to prevent the detector from being under or overexposed (saturated) to the target photons. In either case, the output ceases to be proportional to the fourth power of the target temperature.

4.3 The Flowfield

As previously explained, the wire was placed at the mouth of a pipe designed to produce a laminar flow, implying a parabolic velocity profile inside the pipe. However, the behavior at the exit of the pipe can hardly be assumed the same, due to the viscous interaction between the flow and the still surrounding air. This interaction causes the well-known entrainment effect which affects the flow velocity profile especially at its periphery. Since the air velocities near the pipe wall fall to extremely low values that are difficult to measure, an attempt is made to estimate the velocity profile perpendicular to the wire. According to Blevins (1984, p. 231) a circular jet is fully laminar for Reynolds numbers up to 1000 and fully turbulent for Reynolds numbers above 3000. This Reynolds number is based on the diameter of the nozzle from which the jet issues. Regardless of the jet type of flow, whether laminar or turbulent, both of them exhibit the same type of behavior with regard to the main parameters of interest: the jet width increases linearly with the axial distance (X) while the centerline velocity decreases with inverse proportionality to the axial distance (1/X), see Schlichting (1968), p. 686. To this, it must be added that in both cases the flow pattern fully establishes itself only after a certain distance downstream from the pipe exit. In this case of intermediate Reynolds number of 1700, the distinction between laminar and turbulent jets is more of a semantic matter. The difference is

whether one assumes the transition to be an "entrainment" phenomenon (laminar) or a "mixing" one (turbulent). Therefore, and for these experiments only, further reference will be made simply to "the circular jet". It is assumed that the coreflow is very much like the one in the pipe, the fractional change in the centerline velocity at the wire being of the order of magnitude of 10^{-3} relative to the nominal velocity in the pipe. This assumption was supported by measurements of the coreflow at the mouth of the pipe performed with a static Pitot-tube connected to a U-shaped glass manometer inclined 85.3° from the vertical. The measured core velocity distribution versus the parabolic velocity profile is shown in Fig. 4.4. At the periphery, the jet will experience an enlargement due to the mixing effect. The magnitude of this singular enlargement cannot be predicted in a straightforward way from the theory. Due to mathematical boundary conditions required for solution, it may be assumed that the jet issues from a round slit in an infinite wall. One of the techniques to match the theory with the reality is to assume the nozzle moved back with the wall a "virtual" distance that is calculated through a suitable matching criterion. For example, it can be done by matching the volumetric rate of flow between the actual jet and the assumed one (Blevin, 1984, p. 232). This analysis indicates that the actual flowfield behavior around the wire lies somewhere between the parabolic and the circular jet velocity profiles. The two normalized velocity profiles, parabolic versus circular jet, are shown for comparison in Fig. 4.5, where the positions of the indicated points on the theoretical parabolic distribution coincide with the actual temperature measurement locations as shown in Figs. 4.6 and 4.7 with an error smaller than 2.7% (These figures will be discussed in detail in

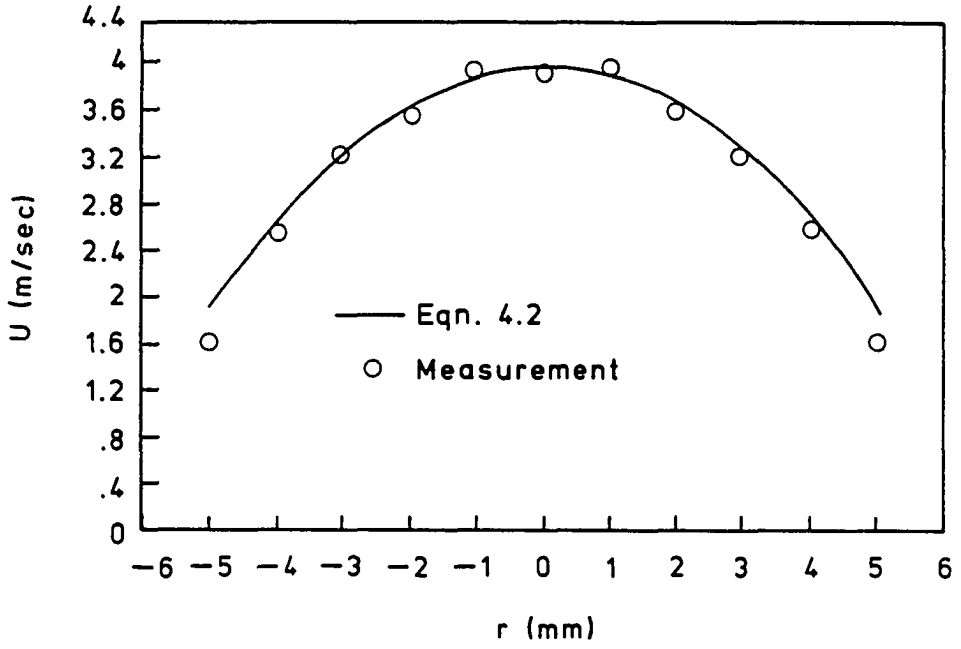

Fig. 4.4 Laminar flow jet experiment: Parabolic velocity distribution vs. Pitot—tube measurements

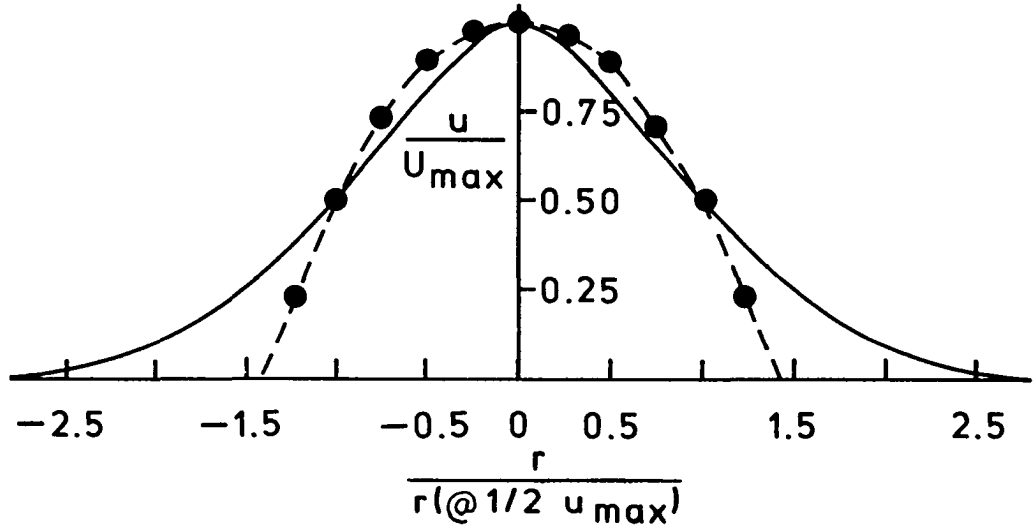

Fig. 4.5 Comparison of the normalized velocity distribution in a circular turbulent jet with a fully developed laminar flow in a pipe (parabolic distribution).

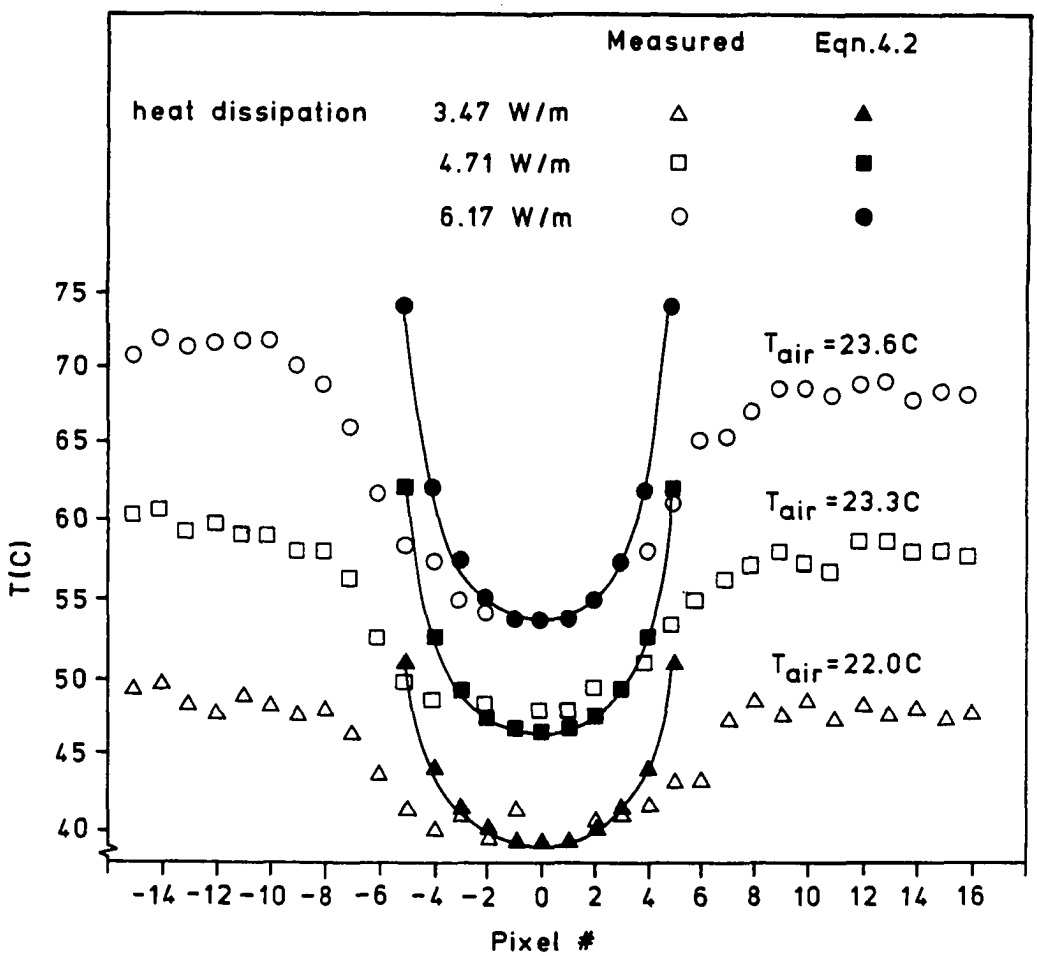

Fig. 4.6 Heated wire temperature distribution when exposed to a laminar jet. (lower heating rates) 1 pixel=1.154mm

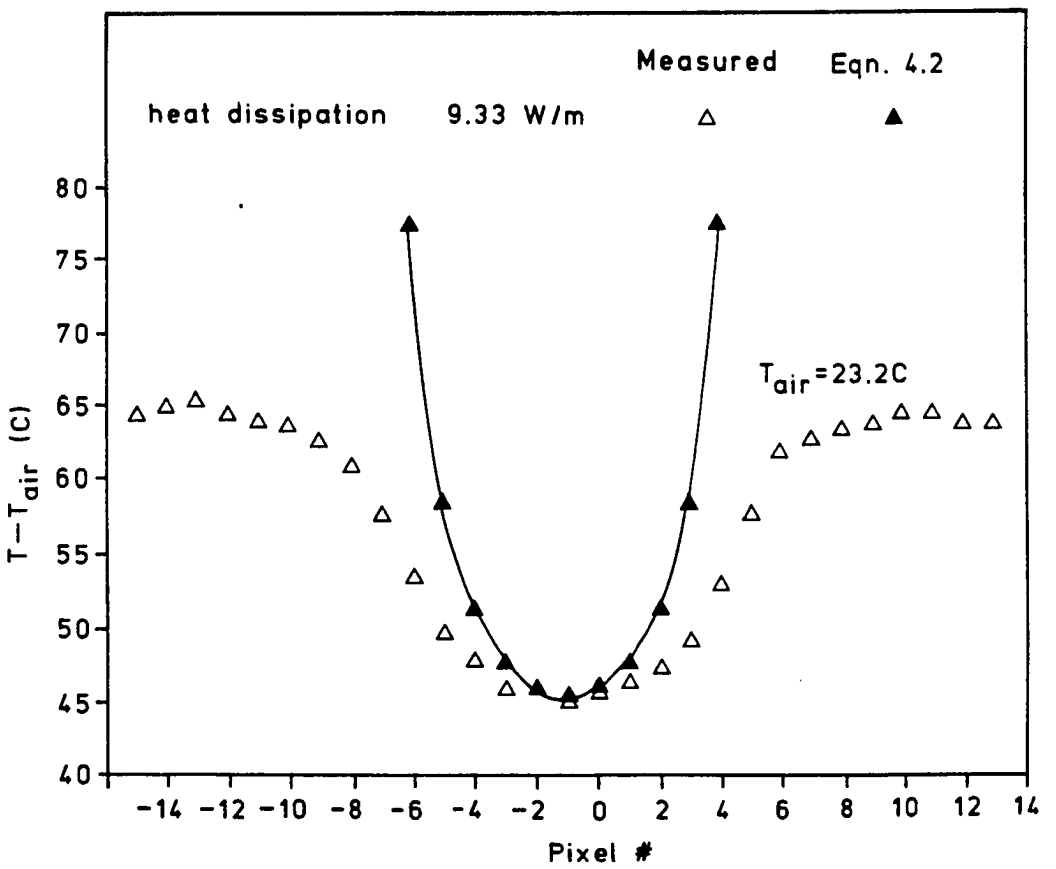

Fig. 4.7 Heated wire temperature difference distribution when exposed to a laminar jet. 1 pixel=1.154 mm. (highest heating rate)

the next section). This comparison suggests that the uncertainty with regard to the actual flow velocity may be too large at the two (symmetrical) most peripheral points and the data there should be treated cautiously. Another point emerging from Fig. 4.5 is that the effective radius of the circular jet flow is about 1.8 times the radius of the pipe. This fact is directly supported by the experimental evidence presented in Figs. 4.6 and 4.7 where the cooled section of the wire is larger than the internal radius of the pipe. Assuming that the extent of the cooled section is an indication of the extent of the actual flowfield, it can be inferred that the capability of the infrared imaging system to map the core as well as the entrained flow regions is demonstrated. Indeed, if one assumes the flow velocities to be approximately the same in all four experiments, the cooled section of the wire length indicating the jet width will be the same too, under the assumption of negligible radiation and conduction. Hence, the "wavelength" of the wire exhibiting a varying temperature distribution will be the same in all four experiments. The validity of this assumption is examined next.

4.4 Results and Discussion

The raw data of the initial experiments at the three lower heating rates are presented in Fig. 4.6. The darkened symbols are given for comparison and represent the expected temperature distribution along the section of the wire directly exposed to the laminar flow. The respective temperatures were predicted from the relation,

$$Nu = 0.795\ Re^{0.384},\quad 1 < Re < 35 \tag{4.1}$$

which is a cross-flow correlation deduced by Morgan (1975) through statistical analysis of some 200 independent experimental and theoretical studies. Although Eq. (4.1) refers to two-dimensional flows, and the circular jet is a three-dimensional flow, it is still possible to use this equation in the present application because the wire diameter is almost three orders of magnitude thinner than the jet. Thus, it is assumed that the wire is on the plane of symmetry of the jet, where the flow, locally can be assumed two-dimensional. The air velocities to be used in Eq. (4.1) were calculated assuming parabolic velocity distribution as predicted by the viscous-flow theory

$$U(r) = U_{max} \left[1 - \left(\frac{r}{R}\right)^2\right] \tag{4.2}$$

where $U(r)$ is the local air velocity inside the jet, U_{max} is the maximum air velocity at the center of the pipe, r is the radial coordinate and R is the internal radius of the pipe. In this case, U_{max} = 4 m/sec. The final result that correlates the temperature difference between the heated wire $\Delta T(r)$ and the airflow (see Appendix A, Eq. A7) is given by

$$\Delta T(r) = \frac{\dot{q}}{0.795\pi\, k_a} \left\{\frac{\nu_a}{2U_{max}\left[1 - \left(\frac{r}{R}\right)^2\right]R}\right\}^{0.384} \tag{4.3}$$

where $\dot{q}$ is the electrical heat generation per unit length of wire, k_a is the heat conductivity of the air and ν_a is the kinematic viscosity coefficient of the air. The Reynolds number at the computed points varied roughly between 4 to 20. Figure 4.6 indicates that increasing the wire overheat value improves the signal to noise ratio and the resulting acquired data is better correlated. The quantitative evidence is presented in Table 4.2 where r^2 is the (statistical) coefficient of

Table 4.2 The coefficient of determination r^2 for the temperature measurements made with the infrared imaging system using the heated wire technique at various levels of heating rates, exposed to a circular jet.

Experiment #	Heating rate [w/m wire]	r^{2*} [%]
1	3.47	41.0
2	4.71	53.1
3	6.17	80.1
4	9.33	98.2

*Adjusted for degree of freedom.

determination (see Appendix A, Eq. A.4). On the negative side, high overheating may cause changes in surface emittance, excessive wire elongation (with resulting vibrations) and thermal contamination of the flow. Thus, the overheat value should not be set to exaggerated values. A second observation relates to the fact that the measured temperature values systematically depart from the expected values according to Eq. (4.3.). These trends become more evident in the data from the experiment with the highest heating level presented in Fig. 4.7, where the wire temperature difference is graphed in order to make the results more meaningful for heat transfer evaluations.

Since the correlation given by Eq. (4.1) accounts only for the forced convective heat transfer, the magnitudes of the other two heat transfer modes, namely conduction and radiation, were estimated in order to assess their influence on the results. The radiation effect was found to be negligible. Because of the moderate wire overheat values, the emittance was assumed constant and, according to Kirchhoff rule, the absorbtance could be taken to be the same as the emittance (Eckert and Drake, 1972, p. 612). Thus, even for an overheat of, say, 80K above the room ambient the radiation effect turned out to be three orders of magnitudes lower than the generated heat. In order to estimate the possible heat conduction contribution, the measured temperature profile of the experiment with the highest overheat was approximated by a polynomial function that indicated a maximum temperature gradient of 2524K/m. With a mean wire thermal conductivity of 50 w/mK, the conductive loss for a wire element between two adjacent sampling points is still two order of magnitudes lower than the generated heat and the influence of this mechanism can be discarded too.

Table 4.3 presents in a tabular form the departure of the Nusselt number as deduced from the temperature and heating rate data of experiment #4 from the Nusselt number as predicted by Eq. (4.1), and assuming the parabolic velocity distribution inside the jet. The positive departure values exhibited by the results raises the suspicion that the infrared imaging system may have difficulty in accurately mapping high gradient temperature fields. Stallings and Whetsel (1982) came to a similar conclusion using a similar camera (Thermovision® 680) to map the temperature variation along a bar with an almost constant temperature gradient. Their data show that while the system could track temperature gradients of 109K/m (5R/in) with a ±1% error, at 262K/m (12R/in) this error increased to -1.5%, but they did not pursue this issue to determine the dependency of the error on the temperature gradient of the measured field, as may be done in the present circumstances.

In this case, it will be easier to evaluate the influence of the temperature field gradient on the measurement accuracy, because of the position dependence of the temperature gradient along the wire. For this, it was assumed that the actual wire temperature distributions could be approximated by a cosine-type function between $X = 0$ at the maximum wire temperature and $X = \ell/2$ at the minimum wire temperature (0 and π radians respectively). This approximation function was suggested by the experimental data shape. While doing this, it was assumed that the temperature measurements are essentially correct in regions with no sharp gradients (Stallings and Whetsel, 1982). The approximating functions are presented in Appendix A3. The final result is presented in Fig. 4.8, where the estimated error in the measured Nusselt number

Table 4.3 Nusselt number comparison for the laminar flow jet using the heated wire technique for experiment #4 (highest overheat).

Pixel #	Re* [Actual]	Nu(correlation) [= 0.795 $Re^{0.384}$]	Nu [Actual]	$\frac{Nu(act)-Nu\ (cor)}{Nu(cor)}$ [%]
0	17.018	2.361	2.384	0.9
+1	16.508	2.333	2.357	1.0
-1	16.508	2.333	2.337	0.2
+2	14.976	2.248	2.312	2.9
-2	14.976	2.248	2.337	4.0
+3	12.423	2.092	2.268	8.0
-3	12.423	2.092	2.244	7.3
+4	8.892	1.840	2.180	18.4
-4	8.892	1.840	2.163	17.6
+5	4.297	1.397	2.029	45.2
-5	4.297	1.397	2.009	43.8

*Decreasing Reynolds number coincides with increasing temperature gradient due to the velocity distribution of the flowfield. (See Figure 4.7 and Appendix A3)

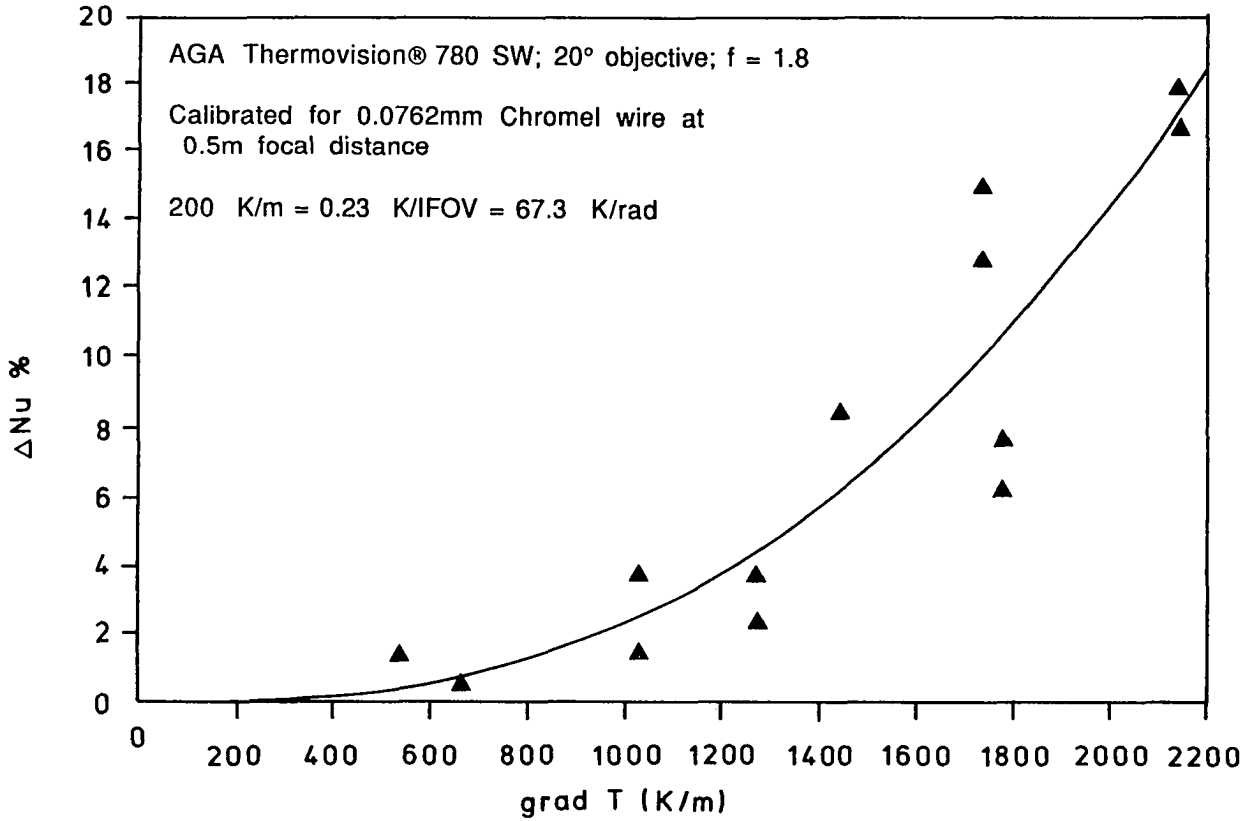

Fig. 4.8 Error in the experimental Nusselt number due to the IR camera limitation in tracking the high gradient temperature distribution, IFOV=0.0034 rad

relative to the expected values from Eq. (4.1) are shown versus the temperature gradient along the wire at the location of measurement. The Nusselt number error shown in Fig. 4.8 was uniformly adjusted by the difference between the experimental and the correlation values found at the point with zero temperature gradient. This small discrepancy (see Fig. 4.7) was assumed to be a systematic error applying all along the set of data belonging to the same experiment. The data points for Fig. 4.8 were taken from the last two experiments (with the higher heating rates) were the signal to noise ratio was previously found to be high enough to produce well correlated data. Data points for the two most peripheral points in each experiment, to which reference was made previously, have been excluded. The line in Fig. 4.8 should not be interpreted as the regression curve on the data points. It is rather shown there with the purpose of indicating the trend of the findings. The conclusion of this analysis is that Nusselt numbers values deduced from the IR imaging system temperature measurements will always be higher than the actual ones. The explanation lays in the fact that the heating rate is known and constant, the dissipation is effected solely by convection, and the actual wire temperatures are higher than the measured ones. Therefore, Nusselt numbers that are deduced based on this kind of information should be corrected to actual values by substrating the error inherently associated with this type of measurements.

One question that remains open on this issue is whether the infrared camera limitation to track high temperature gradients is a function of the absolute value of the gradient itself (K/m), or of the variation of the temperature in the instantaneous field of view (K/IFOV

or K/rad). To answer this problem, it would be necessary to undertake another set of experiments, deviating from the objectives set-out for this research. However, the resemblance between Figs. 4.8 and 3.2 relating the minimum detectable temperature difference is remarkable. Indeed, the prediction made on the basis of the IR imaging camera operational characteristics about its inability to accurately resolve high temperature gradients turned out to be true.

The quantitative estimation of the performance of the infrared imaging system is a very difficult task. The first difficulty refers to the reliability of the heat transfer data chosen to be the reference. As Morgan points out, "The percent coefficient of variation of the Nusselt number for a given Reynolds number for the experimental data varies from 10% to 29% depending on the Reynolds number, whereas that for the various correlations varies from 10% to 46%". Based on the present measurements, and referring only to those performed in near zero temperature gradient regions, it was found out that the experimental Nusselt number based on infrared imaging system measurements could further vary by as much as 3.3% from the predicted one by Eq. (4.1) to which Morgan's remark refers. The second difficulty refers to the fact that the experimental data set resulted from a series of processes on the raw (detector) signal, that practically nothing is known about the transfer function operating on it. First, there is the IR imaging camera, then its accompanying analog processor and finally the computer digitizer and its software. (Several attempts to get some information about these transfer functions from the suppliers were not answered). Therefore, there is no choice left but to look at this system as a "black box" and to assess its performance by controlled experiments,

even though this task is double complicated because of the uncertainty induced at the same time by both the measurement apparatus and the reference data. In any case, the trend in Fig. 4.8 shows that the accuracy of the deduced Nusselt numbers from temperature measurements performed with the infrared imaging system is adversely influenced by the existence of a temperature gradient at the location of interest. It also confirms that this system may be able to track accurately temperature variations up to about 350 K/m which is in good agreement with the findings of Stallings and Whetsel (1984). Furthermore, according to the evidence presented, at high temperature gradients the indicated temperature is always lower than the actual one. This suggests that it is possible to produce a calibration curve similar to Fig. 4.8 and use it to correct the experimental measurements prior to processing the data.

The uncertainty with respect to the accuracy of heat transfer correlations is further emphasized by the results measured on the uncooled portions of the wire. Although the free convection heat transfer was out of the scope of the present study, it was interesting to observe that on those segments, the predicted Nusselt number as regressed by Morgan, grossly underestimates the actual heat transfer process, as it is shown in Table 4.4.

The verity of the present findings are indirectly supported by Fand et al. (1977) where it is shown that as the Rayleigh number (Ra = Gr Pr) decreases, the discrepancy between predictions based on Morgan's correlations and the data obtained increases. It may reach as much as 30% for Ra numbers as low as 300. In the present case, the Ra numbers were even lower, typically 10^{-3}.

Table 4.4 Mean temperature difference between the heated wire under free convection and the ambient air as a function of the wire heat dissipation.

$\dot{q}''_o$ (w/m wire)	ΔT predicted (K) Nu-Gr corr.*	$\Delta\bar{T}$ (K) Experimental
3.47	65	25.6
4.71	86	34.5
6.17	110	44.8
9.33	161	63.9

*See Appendix A2 item 3.

The deduction of the velocity profile from the measured temperature profile through Nu-Re correlations is also possible. This time, the process is reversed and assuming the correct correlation is available, the known differential temperature is used to calculate the velocity that would produce it. This approach is schematically shown in Fig. 4.9 and quantitatively described in Appendix A2 item 5. The results for the first two experiments (lower heating rates) are presented in Fig. 4.10 while the results for the last two experiments (with the highest heating rate) are presented in Figs. 4.11 and 4.12. For the predicted velocity values, Eq. (4.3) was reformulated to express the local jet velocity U(r) in terms of the local temperature difference $\Delta T(r)$ between the heated wire and the air

$$U(r) = \frac{0.909\ \nu_a}{R}\left[\frac{\dot{q}}{\pi\ k_a\ \Delta T(r)}\right]^{2.604} \qquad (4.4)$$

Once again the reader is reminded that the two most peripheral points in each graph should be regarded more as a mathematical feature (arising from the assumed parabolic distribution) than an actual physical reality. A comparison between Figs. 4.10-4.12 only emphasizes how important is in this case to get well correlated temperature measurements before proceedings with the data processing (see Table 4.2). The explanation of the higher scatter of the deduced velocities (Fig. 4.10) than that of the temperature data from which they were deduced (Fig. 4.6) lies in the behavior of the Nu-Re correlations. These correlations assume a behavior like, $Nu \sim Re^n$ $0 < n < 1$. In the former case one gets $\Delta T \sim U^{-n}$ while in the latter $U \sim (\Delta T)^{-1/n}$, thus causing the deduced velocity behavior U to be quite sensitive to the scatter of the temperature measurements. In spite of this fact the results of the

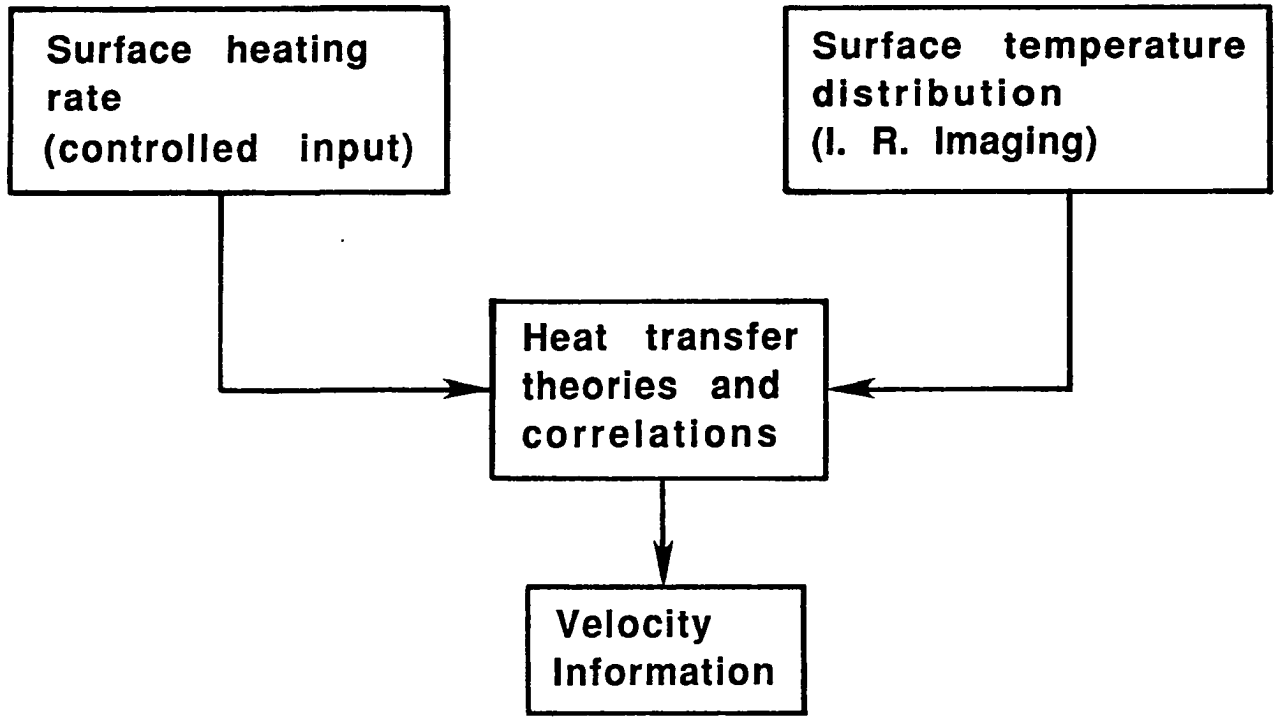

Fig. 4.9 The concept of flowfield velocity deduction through Infrared Imaging of the surface

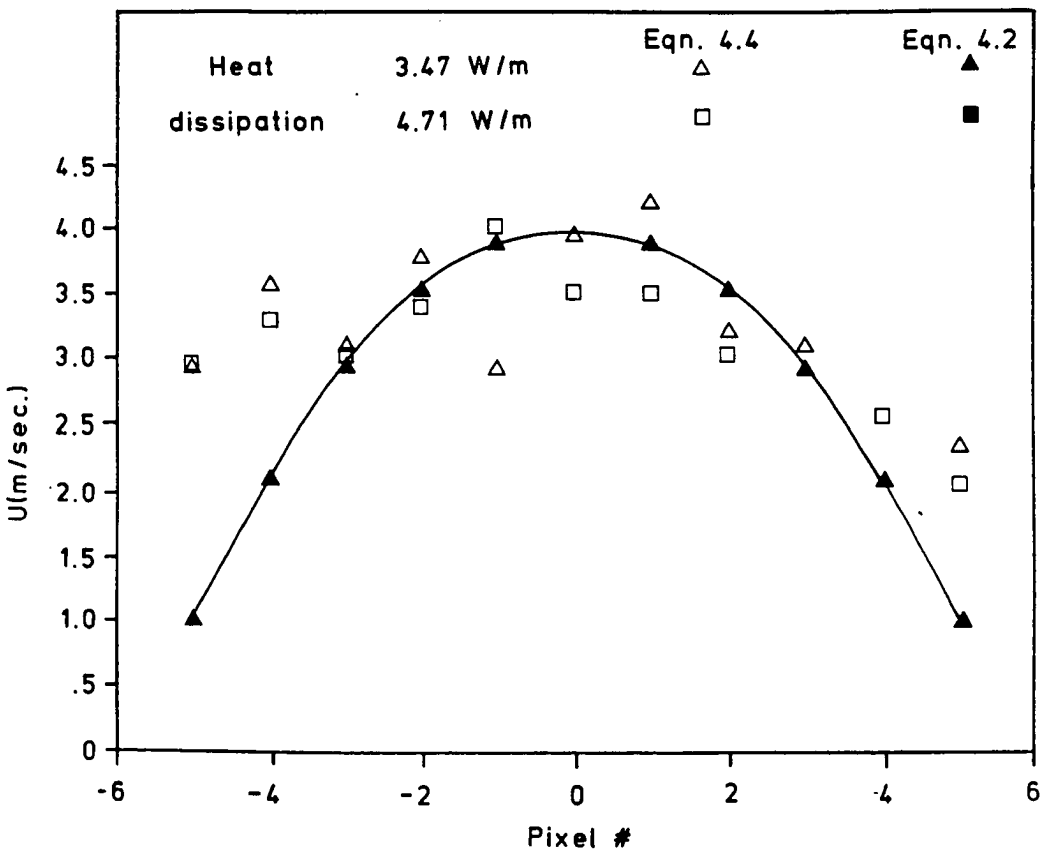

Fig. 4.10 Velocity profiles as deduced from the heated—wire laminar—jet measurements (lower heating rates)

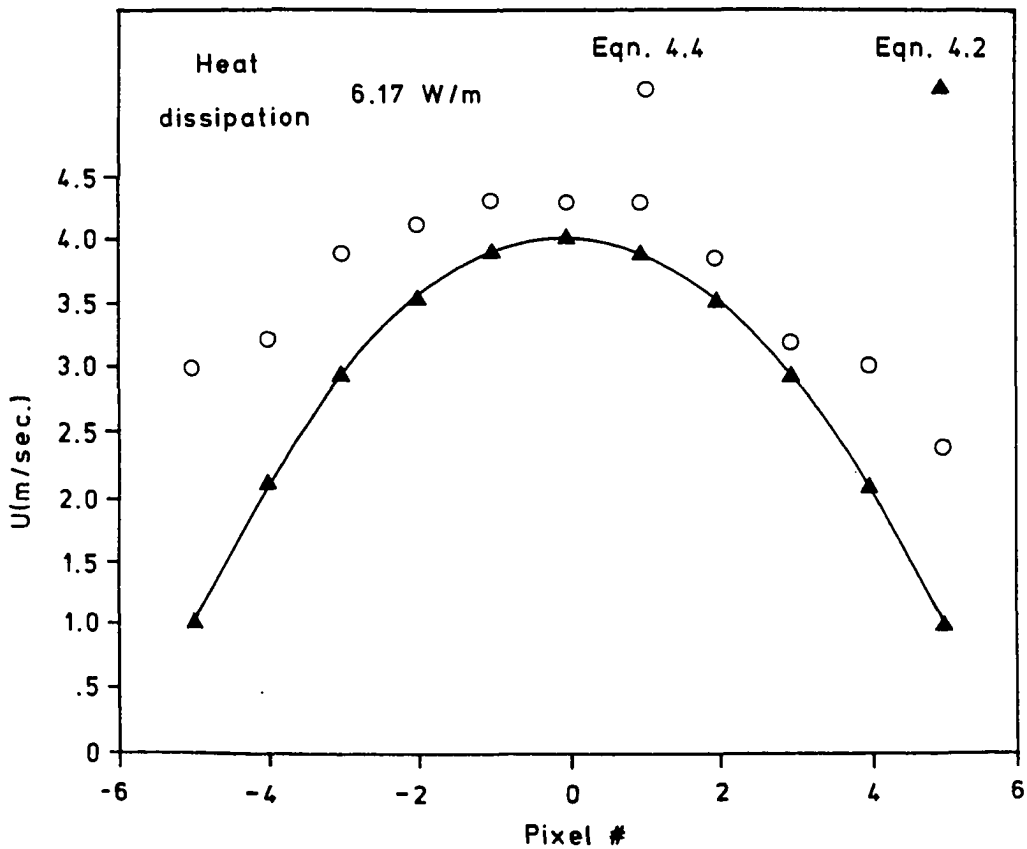

Fig. 4.11 Velocity profile as deduced from the heated—wire laminar—jet measurements (intermediate heating rate)

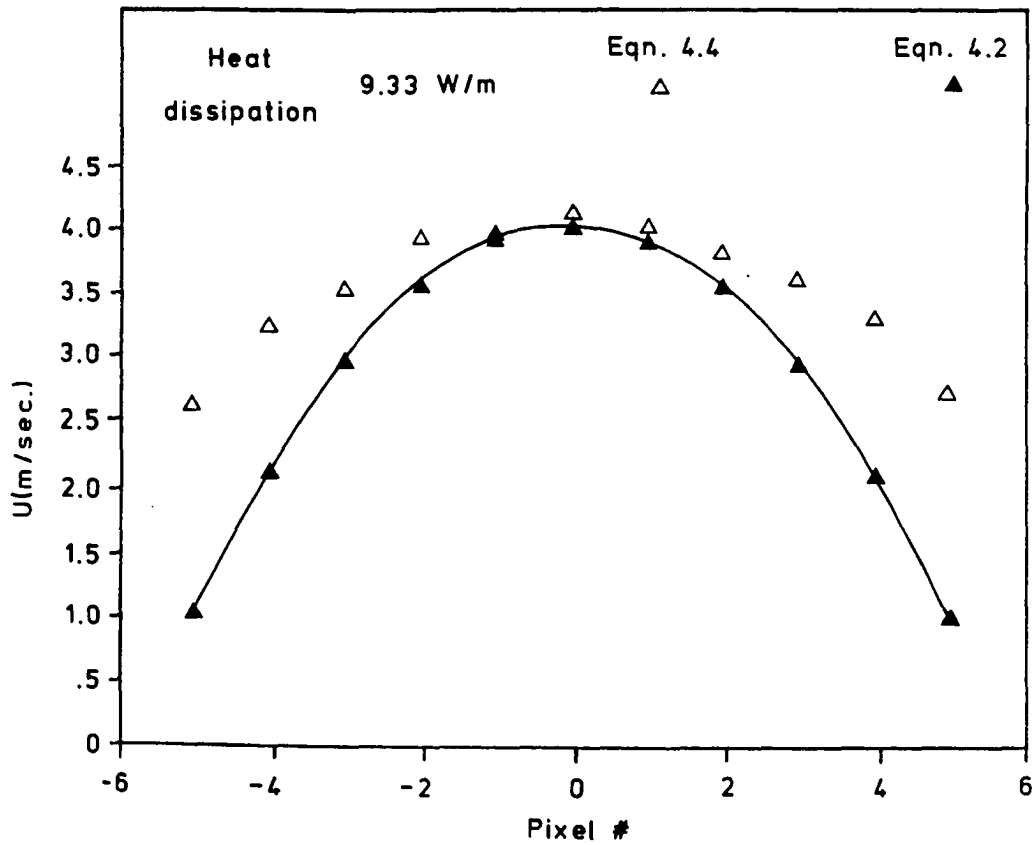

Fig. 4.12 Velocity profile as deduced from the heated—wire laminar—jet measurements (highest heating rate)

experiments with the higher heating rates (and thus the best correlated data) prove that the concept of deducing velocity information is viable.

The encouraging aspect of this approach is that as the Reynolds number increases with the velocity, so does the heat transfer coefficient, on a power law basis (Morgan, 1975). The net result of this feature is to increase substantially the accuracy of the velocity predictions from the temperature measurements.

4.5 Summary

This set of experiments showed that using an infrared imaging system, one can detect local temperature variations, and hence Nusselt number variations, that may occur over a very limited portion of the camera's field of view. The concept proved to be applicable in the core region of the flow as well as in the entrained part of it. The capability of accurately tracking temperature variations was found to be in this case as high as 350 K/m. A question still to be answered is whether or not this limit is set by the actual value of the temperature gradient, or by the variation of the temperature in the field of view of the IR imaging camera. The inverse approach of using temperature measurements in conjunction with heat transfer correlations to deduce local velocities was shown to be possible in principle. This method shows promise for use in aerodynamic research: (1) provided the wire overheat is high enough to get good signal to noise ratio measurements, (2) the temperature gradient problem is solved by appropriate calibrations, and, (3) more accurate forced convective heat transfer correlation may be found. The last condition should be viewed not only in the perspective of this particular research, but in the wider context of

better understanding the complexity of convective heat transfer processes.

Chapter 5

THE FLAT PLATE EXPERIMENT

Following the heated wire experiments that essentially involved only one mode of heat transfer namely convection, the attention turned to a more general type of experiment in which all three modes were involved. The choice was a laminar flat plate experiment which was designed to measure surface temperatures on an actively heated surface subjected to a uniform free-stream flow. The purpose was to produce an "aerodynamic" target whose temperature distribution as measured by the infrared imaging system could be assessed by analytic results from velocity and thermal boundary layer analysis.

5.1 The Experimental Set-Up

The target flat plate measured 32 cm. chordwise, 90 cm. spanwise, was made of wood, and had a sharp leading edge of the type assumed in the Blasius analysis of the boundary layer. The IR imaging camera was placed laterally at 55 cm. from the target, behind a second plate (parallel to the first one), with a circular hole through which the camera could view the target. This was done in order to prevent the vortices shedded from the camera from interfering with the flow over the target plate. The experiments were carried out in a 0.9x1.2 m (3'x4') low speed wind-tunnel, where the entire assembly was placed vertically as shown in Fig. 5.1. The zero angle of attack of the plates was determined by using a cylindrical two-hole differential pressure probe

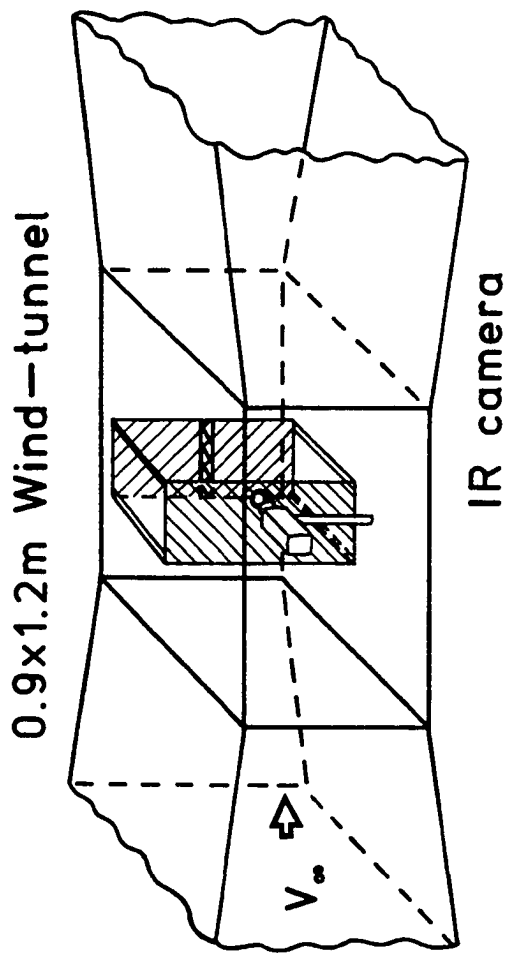

Fig. 5.1 Layout for IR surface measurements of a heated flat plate in a uniform freestream

connected to a U-shape glass manometer. In order to eliminate errors associated with geometrical misalignments, the zero angle of attack was established from the mean of two readings, with the pressure probe at its normal position and then rotated 180° around its axis. Separately this measurement was done with a vane-type indicator working on the weathercock stability principle. The accuracy of both devices was established to be within 0.5°.

The target flat plate was placed in the wind-tunnel at +0.5 degree angle of attack in order to be on the safe side regarding separation. The active heating of the target plate was achieved locally, at one third of the span, by wrapping chordwise a 0.00397" Constantan wire three times around the plate at 2 mm pitch, and connecting it to a power supply. To ensure uniform surface texture, roughness and heating, these wires and the entire surrounding area in the field of view of the camera were covered chordwise with three adjacent strips of 2" wide duct tape. At 85 mm. from the leading edge, a Chromel wire was soldered to the Constantan wire and its lead was taken straight to the back of the plate through a very small hole that was drilled in the wood. As shown in Fig. 5.2, this layout permitted the experimenter to carry-out emittance calibrations of the duct-tape surface by providing the true surface temperature. Hence, the Constantan wire played a dual role in this experiment, either as a heating element when connected to the power supply, or as a thermocouple element when connected to a digital thermometer. The desired function was selected by switching between the two circuits.

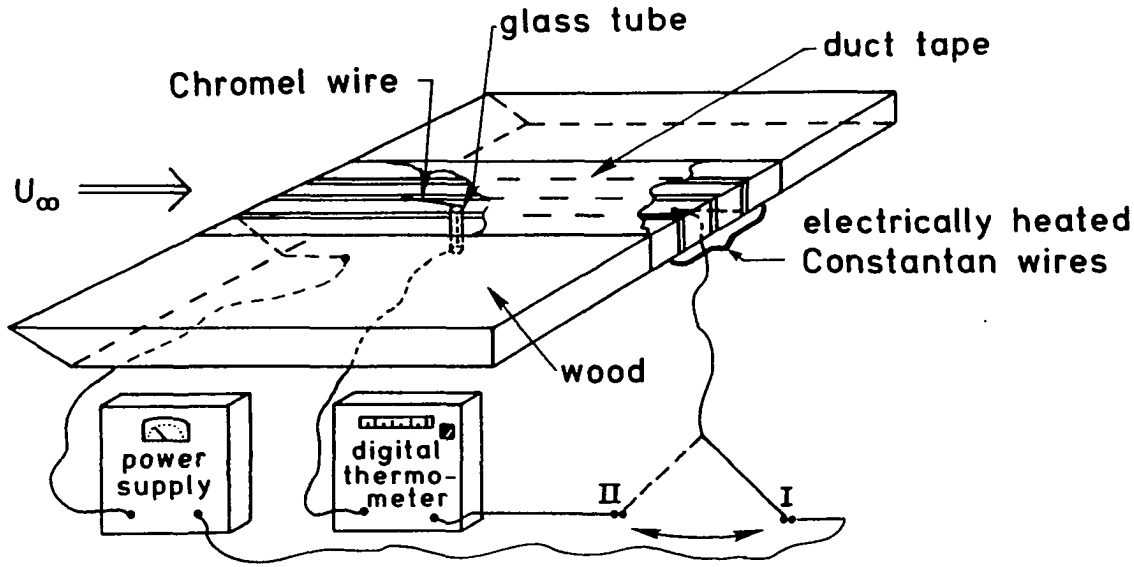

I ELECTRICAL HEATING CIRCUIT
II TEMPERATURE MEASUREMENT CIRCUIT

Fig. 5.2 Cutaway of the heated flat plate

5.2 The Experiment Description

The guiding rule in performing these experiments was to make them as short as possible. There were two reasons for this; one, concerning the wind-tunnel operation, the other concerning the substrate participation in the heat transfer process. Since the wind-tunnel used in this experiment is of closed circuit type, the longer the operation period the higher is its air temperature. At room temperature, the initial rise of the air temperature in the wind-tunnel is about 1.2°C/min. This phenomenon has a negative influence on the heat transfer process from the flat plate to the fluid and in general is disruptive to infrared measurements. The other concern was that long periods of heating, would affect the substrate to an unknown degree resulting in long cooling times between runs and irreproducible results. In this respect, the thermocouple used for emittance calibrations proved to be of significant help, in establishing the substrate initial conditions for each test.

According to the above mentioned guidelines, a typical experiment would run for less than one minute with the time split between the following steps.

(1) Wind-tunnel starting and achieving steady-state operation (approx. 15 secs.)

(2) Turning-on the power supply, and recording of the data. Turning-off the power supply (approx. 20 secs.)

(3) Keeping the wind-tunnel running to cool the plate (approx. 15 secs.) and stop its operation.

The working point of the various systems participating in this experiment was determined in previous runs. The nominal test conditions were established to be:

(1) Wind tunnel air speed: 21 m/sec

(2) Electric current through the heating wire: 345 mA. Total resistance of the heating wire: 135 Ω

A total of 20 tests were performed. Of these, eleven tests were recorded. Since the results of all the runs were very much alike, only the last three were picked-up for data analysis. The reproducibility of the results ensured that no further benefit would have come out of analyzing more profiles, except perhaps to establish a statistical variation measure for the data set.

5.3 Results and Discussion

The chordwise temperature profiles as obtained from the last three runs are shown in Fig. 5.3. The data in Fig. 5.3 was extracted from computer stored thermographies, an example of which is shown in Fig. 5.4. Note the longitudinal (chordwise) temperature distribution under the thermography and the latitudinal (spanwise) temperature distribution at three different stations along the chord, to the right of the thermography. The wind-tunnel air temperature for runs 1 and 2 was 28.6°C and for run 3, was 29.0°C. The actual wind tunnel air velocity was 20.9 m/sec during all three runs. The camera's field of view in this configuration was 16.5x16.5 cm, and the Reynolds number of that area of the plate scanned by the camera varied between zero (at the leading edge) to about 217000. This means that the phenomena addressed should be all under the laminar boundary layer regime, Re_{crit} = 500,000.

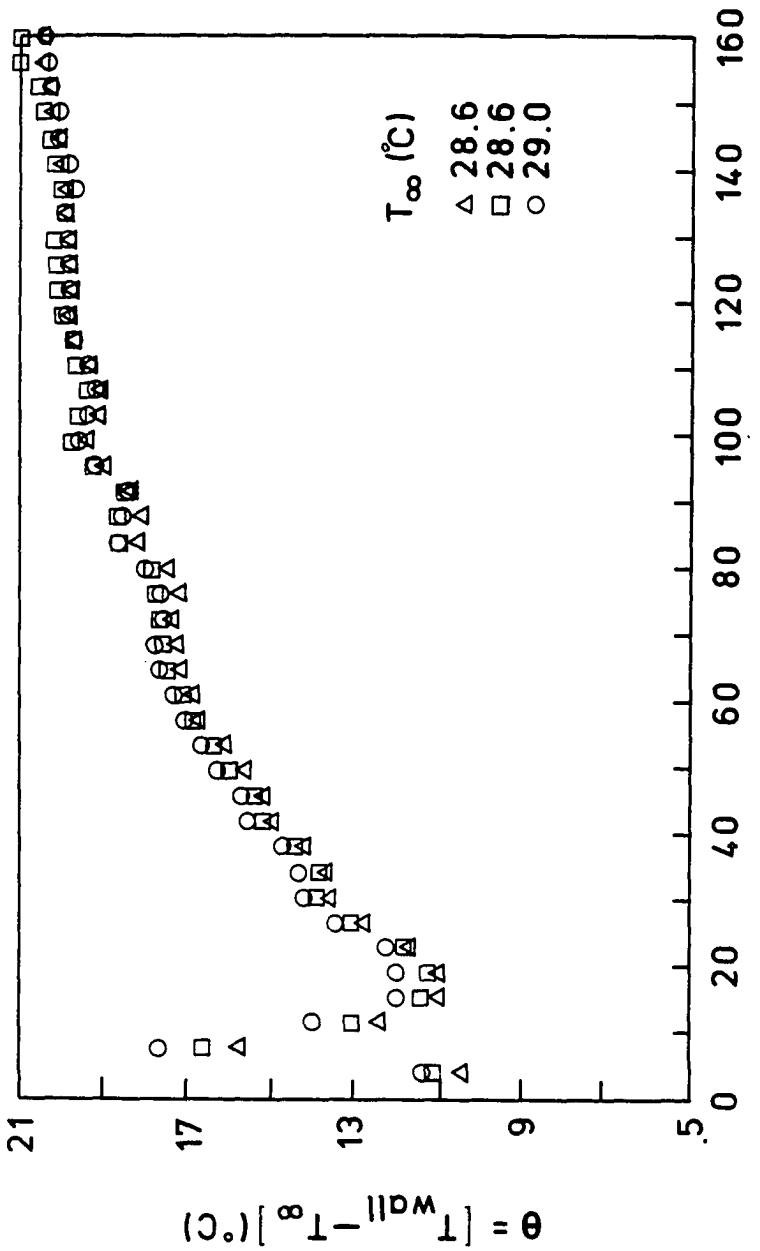

Fig. 5.3 Constant power heated flat plate experiment: adjusted temperature profile vs. distance from leading edge, $Re_X = 1.233 \times 10^6$ X(m)

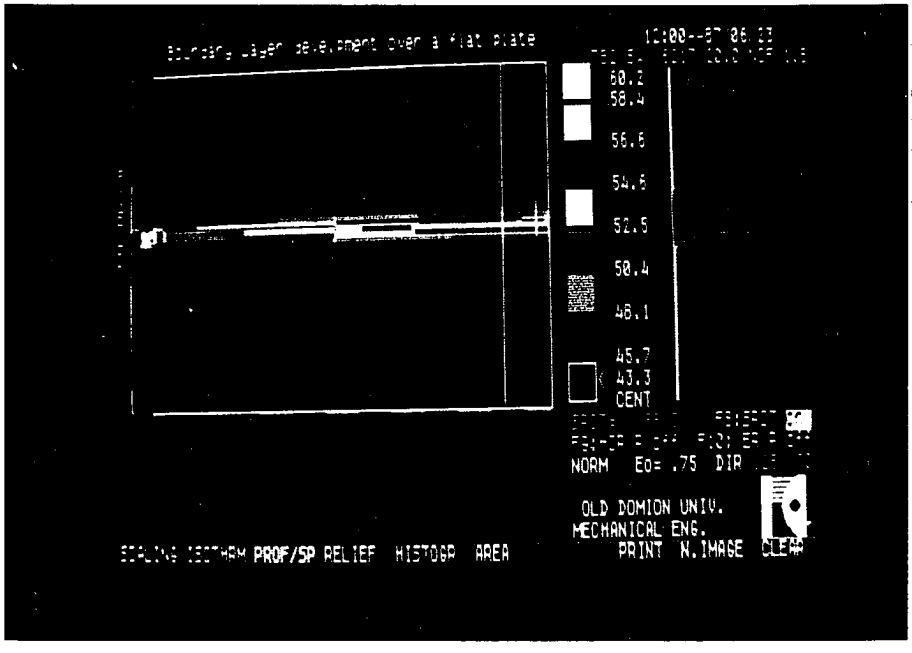

Fig. 5.4 Constant power heated flat plate experiment DISCO II® output with longitudinal and latitudinal temperature distributions. Air flows from left to right

The data as presented in Fig. 5.3 displays the temperature profile along the plate reduced by the airflow temperature, versus the chordwise coordinate. A first evaluation of these profiles reveals the following:

(1) The information gathered from all three runs was quite reproducible, and the data points obtained from the different experiments almost coincide.

(2) The general qualitative behavior of the surface temperature distribution meets the expectations based on the laminar boundary layer theory, i.e., a temperature rise proportional to the square root of the distance from the leading edge.

(3) The leading edge experiences an abrupt increase in its temperature, due to its sharpness. This geometrical feature causes a finite amount of heat to be absorbed by a theoretically infinitesimal substrate mass, with the consequent real increase in temperature. The effect is further augumented by the fact that the heating wires being wrapped around the plate, the leading edge is well heated from all around its contour.

(4) The temperature distribution exhibits some irregularity around the coordinate x=8 cm. This is the region where the thermocouple junction was placed, a fact that caused a slight "bumpiness" (about 0.1 mm high and 8 mm long streamwise), on the overlaying duct tape surface. This geometrical feature initiated a directional emittance factor, which is usually lower than its normal counterpart, especially in the range of local inclination between 60° to 90° (Sparrow and Cess, 1978, p. 55). This effect, not being

taken into account by the system's software, is ultimately (and falsely) interpreted as a local drop in temperature.

As a result of these considerations, it was decided to proceed with the analysis of the experiments, using only the data points starting at the coordinate x = 1.9 cm from the leading edge (the first 1.52 cm from the leading edge were ignored). The numerical values of these coordinates resulted from the fact that the data was extracted at each third consecutive pixel, which on the plate is equivalent to 3.8 mm.

In search for a model against which the experimental results can be evaluated, the physical reality suggests using the flat plate laminar boundary layer model with constant heat flux at its surface as the prescribed boundary condition. The model, assuming a general heat flux distribution chordwise and its analytical solution, was formulated by Klein and Tribus (1952). When simplified to the constant heat flux assumption, the solution reads

$$\Theta(x) = 2.2019 \frac{\dot{q}_o''}{k_a} Pr^{-1/3} \left(\frac{\nu_a}{U}\right)^{1/2} x^{1/2}$$

$$= \text{const} \cdot x^{1/2} \qquad (5.1)$$

where $\theta(x)$ is the difference between the local wall temperature and the freestream air static temperature, $\dot{q}_o''$ is the wall heat flux, k_a is the air conductivity, Pr is the air Prandtl number, ν_a is the air kinematic viscosity, U is the freestream air velocity and x is the distance from the leading edge. According to this model, when the flat plate temperature distribution corrected by the ambient air temperature is plotted against the square-root of the distance from the leading edge, the slope of the line is an indication of the heat flux convected into

the airstream. When this plotting is done for the present case, as shown in Fig. 5.5, its analysis shows that although the data is well correlated (r^2 is 0.945 with a variance of 0.38) the assumed linear behavior of the data is not uniform all along the coordinate scale. A closer look suggests one linear regression for the first 14 stations and another for the last 18 stations, leaving 6 stations in between as a transition zone. Following this approach, the variance of the data goes down, for the first group to 0.1 and for the second group to 0.05, which is significantly better. The question is what causes this change in the pattern behavior. An answer lies in the actual physical process taking place with this experimental set-up and its departure from the assumed model (see Eq. 5.1). As shown in Fig. 5.6, the theory assumes a flat plate "pumping" a constant amount of heat flux into the airstream. For a desired constant value of this heat flux, a certain prescribed temperature distribution should be maintained (or obtained) in order to compensate for the fact that the boundary layer thickens and heats up streamwise. In this case, the constant heat generation rate is shared mainly by two participating media, the wooden substrate by conduction and the airflow by convection. Heat transfer by radiation is also taking part, but is insignificant. Since the air cooling by convection is more effective on the forward part of the plate, (due to the thin boundary layer), the heat transfer by conduction to the substrate is less than on the aft part of the plate, where the boundary layer is thick and the convective heat transfer is much poorer. The estimation of the boundary layer behavior will show that between the first and the last station of the first data group, it thickens by 90% (from 0.60 mm. to 1.15 mm) while with respect to the second data group, it continues to

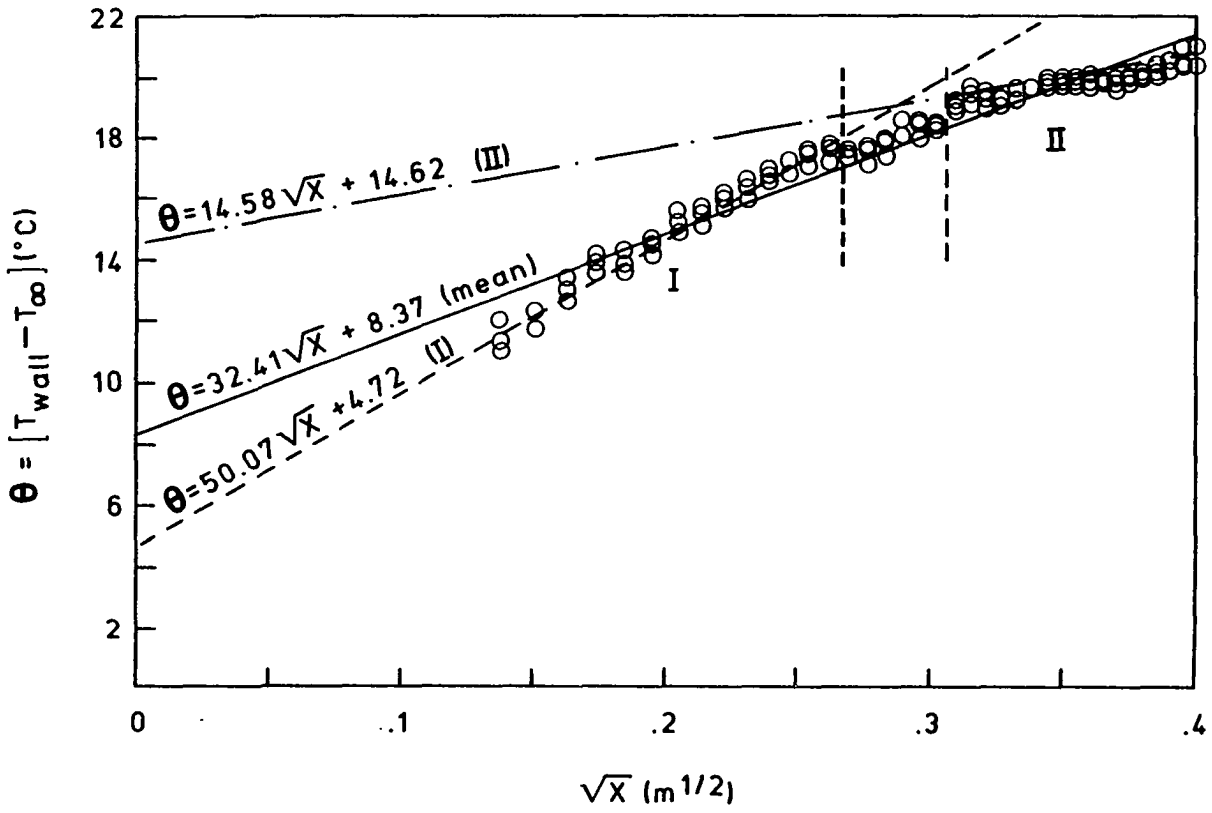

Fig. 5.5 Constant power heated flat plate experiment: adjusted temperature profile vs. square—root of distance from the leading edge. $Re_x = 1.233 \times 10^6 X(m)$
Data points of three different experiments.

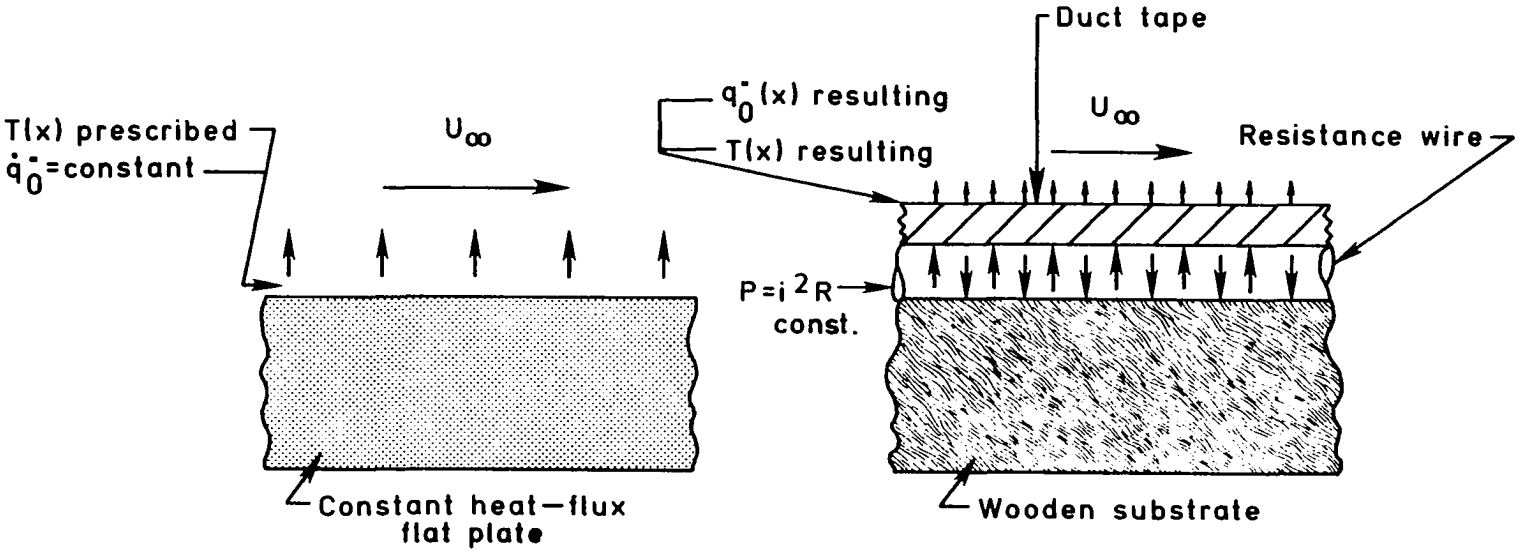

Fig. 5.6 Heated flat plate experiment: comparison between the theoretical constant heat flux model and constant power reality.

thicken but only by 30% (from 1.35 mm. to 1.75 mm.) (see Appendix B, Eq. B7).

Looking more attentively at Fig. 5.5, one may further observe that the general trend of the slope of Θ vs. $x^{1/2}$ is to decrease gradually from the leading edge downstream, at the same time that the overheat of the substrate is going up. This feature is an additional evidence to the ever increasing participation of the substrate due to the gradual decreasing effectiveness of the convective cooling, and it happens in spite of the fact that the wood qualifies as a heat insulator.

The thermal energy analysis performed on the flat plate is summarized in Table 5.1. The convective heat transfer was calculated from the temperature regressions given in Fig. 5.5. It is a superposition of the heat flux as generated by a constant temperature distribution (Kays and Crawford, 1980, p. 139)

$$Nu_x = 0.332\ Pr^{1/3}\ Re_x^{1/2} \qquad (5.2)$$

(where Nu_x is the local Nusselt number, Pr is the air Prandtl number and Re_x is the local Reynolds number), and a constant heat flux as deduced from Eq. 5.1. Thus, the regressions of Fig. 5.5 present two aspects of the convective heat transfer. The first is contained in the point of intercept of the regression line with the Θ-axis and is indicative of the level of overheat of the substrate that can be accounted for through Eq. 5.2. The second is contained in the slope of the regression line, and is indicative of the variation in the chordwise temperature distribution, that in this case can be accounted through the constant heat flux model as given by Eq. 5.1.

Table 5.1 Mean values analysis of the heat dissipation modes on a flat plate heated at constant wall power generation placed in an airstream at zero angle of attack $Re_x = 1.233 \times 10^6 \times (m)$.

Data points	x	$\dot{q}''_{o\ conv}$	$\frac{\dot{q}''_{o\ conv}}{\dot{q}''_{o\ gen}}$	$\dot{q}''_{o\ rad}$	$\frac{\dot{q}''_{o\ rad}}{\dot{q}''_{o\ gen}}$	$\dot{q}''_{o\ cond}$	$\frac{\dot{q}''_{o\ cond}}{\dot{q}''_{o\ gen}}$
	(1)	(2)		(3)		(4)	
All	1.9 → 159.9	767	18%	82	2%	3335	80%
1st group	1.9 → 68.5	930	22%	73	2%	3181	76%
2nd group	95.2 → 159.9	546	13%	103	2%	3535	85%

(1) distance from the leading edge (mm)

(2) based on Eqs. (5.1) and (5.2) (W/m^2)

(3) based on Eq. (5.9) mean value (W/m^2)

(4) $\dot{q}''_o$ conducted = $\dot{q}''_o$ generated - ($\dot{q}''_o$ convected + $\dot{q}''_o$ radiated), mean value (W/m^2)

conv - convected

gen - generated

rad - radiated

cond - conducted

The quantitative evaluation of the experiment shows that the mean electrically generated power was 949 W/m^2. Locally, along the centerline wire, where the temperature measurements were made, the value of the electrically generated power was 4184 W/m^2 (see Fig. 5.4). As the balance of energy analysis shows (see Table 5.1), the highest value of the mean heat flux convected into the air along that wire was 930 W/m^2. This value is of the same magnitude to the solar heat flux at the earth surface. Therefore, this heating is thought to affect the boundary layer on the flat plate no more than it occurs in reality over the wing of an airplane.

5.4 The Infrared Imaging System as a CFD Codes Validation Tool

The interaction between a solid body and a surrounding flowfield of different temperature has both a momentum and an energy exchange aspect. The former is responsible for the velocity distribution around the body while the latter is responsible for the heat flux distribution over its surface. This heat flux will continuously change the temperature distribution of the body substrate and particularly of its surface. Thus, in general, even under steady flow with constant free-stream temperature conditions, the surface temperature distribution of a body may remain time dependent for significant periods of time.

Since the prediction of aerodynamic and aerothermal loads by computational means is and will be one of the main research topics in aerodynamics, there is a clear need for an experimental method to provide data for comparison and validation of the CFD codes. Viewed from this perspective, the infrared imaging systems are ideal tools for such tasks since they do not require instrumented models, nor any

specialized instrumentation conduits in the wind tunnel or on the tested aircraft.

From a general stand point of view, the complete calculation of the interaction between an arbitrary body and the fluid flow requires the following steps: first, the Euler equation

$$\rho \frac{D\vec{U}}{Dt} = \vec{F} - \text{grad } p \tag{5.3}$$

is solved for the external flow, yielding the flow velocity distribution around the body. Here, this equation is given in the incompressible flow formulation where, $\vec{U}$ is the air velocity vector, ρ is the air density, D/Dt is the total derivative operator, $\vec{F}$ is the body force and, p is the pressure.

Next, the Navier-Stokes equation can be solved, perhaps in boundary layer approximation. This equation differs from the Euler equation by the inclusion of the viscous terms $\mu \nabla^2 \vec{U}$. Again, in the incompressible flow formulation it can be expressed as

$$\rho \frac{D\vec{U}}{Dt} = \vec{F} - \text{grad } p + \mu_a \nabla^2 \vec{U} \tag{5.4}$$

where ∇^2 stands for the Laplacian operator and μ_a is the air viscosity. Now with the velocity distribution known around the body, one may solve the energy equation for the temperature distribution in the flow field. Once again invoking the incompressiblity argument and assuming constant properties flow, the energy equation as derived from its internal energy formulation can be expressed in terms of the air temperature field as

$$\rho c_v \frac{DT}{Dt} = k_a \nabla^2 T + \mu \Phi \tag{5.5}$$

where c_v is the air specific heat at constant volume, k_a is the air thermal conductivity, T is the air temperature and, Φ is the viscous dissipation function (Schlichting, 1968, p. 254).

All the above mentioned equations with the addition of the continuity equation, can in principle be solved for the five parameters that uniquely determine the flowfield behavior namely $\vec{U}$, p and T. For the present purposes, the energy equation solution is of the main interest, since it is the temperature gradient of the air in the boundary layer at the wall that determines the heat flux into the body through the Fourier heat conduction law

$$\dot{\vec{q}}_o'' = - k_a \text{ grad } T \tag{5.6}$$

where $\dot{\vec{q}}_o''$ is the heat flux. In order to obtain the temperature distribution on the body surface, it must be remembered that its surface is the solid boundary with respect to the fluid. Therefore, the heat conduction equation

$$\frac{\partial T}{\partial t} = \alpha \nabla^2 T \tag{5.7}$$

where α is the thermal diffusivity of the substrate, must be solved for the solid body in order to determine the surface temperature distribution. Boundary conditions do play a special role. For example, besides the convective heat transfer, heat sources, sinks and thermal radiation effects may occur at the solid boundary.

The convection effect is more conveniently expressed through the Newton law

$$\dot{q}_o'' = h (T_w - T_\infty) \tag{5.8}$$

rather than through the Fourier conduction law. Usually, the combination of the two laws is used to determine the convective heat transfer coefficient h, as a function of the difference between the solid wall temperature T_w and the air freestream temperature T_∞.

The radiation heat transfer obeys the well known Stefan-Boltzmann equation

$$\dot{q}_o'' = \varepsilon \sigma T_w^4 \tag{5.9}$$

where σ is the Stefan-Boltzmann constant and ε is the radiation surface emittance factor.

Schematically, this procedure is summarized in Fig. 5.7, which shows why, in general, this process is unsteady even for steady state flow conditions. The evolving nature of the temperature field of the substrate continuously changes the temperature gradient in the boundary layer and the resulting heat flux.

Once the body surface temperature distribution is predicted, it is possible in principle to construct a synthetic temperature distribution of the body surface, as it is assumed that it will be produced by the infrared imaging system in a test run at identical conditions with those of the calculation. Still to be remembered at this stage is the fact that the configuration geometry, the model material and its finish, and the IR imaging camera specifications, all these factors influence the final thermographic experimental result, and they should be taken into account when computing and synthesizing the predicted temperature distribution (Gartenberg and Roberts, 1988).

Hence, through a complete set of aerodynamic and heat transfer calculations, it is possible to come up with computed results that are

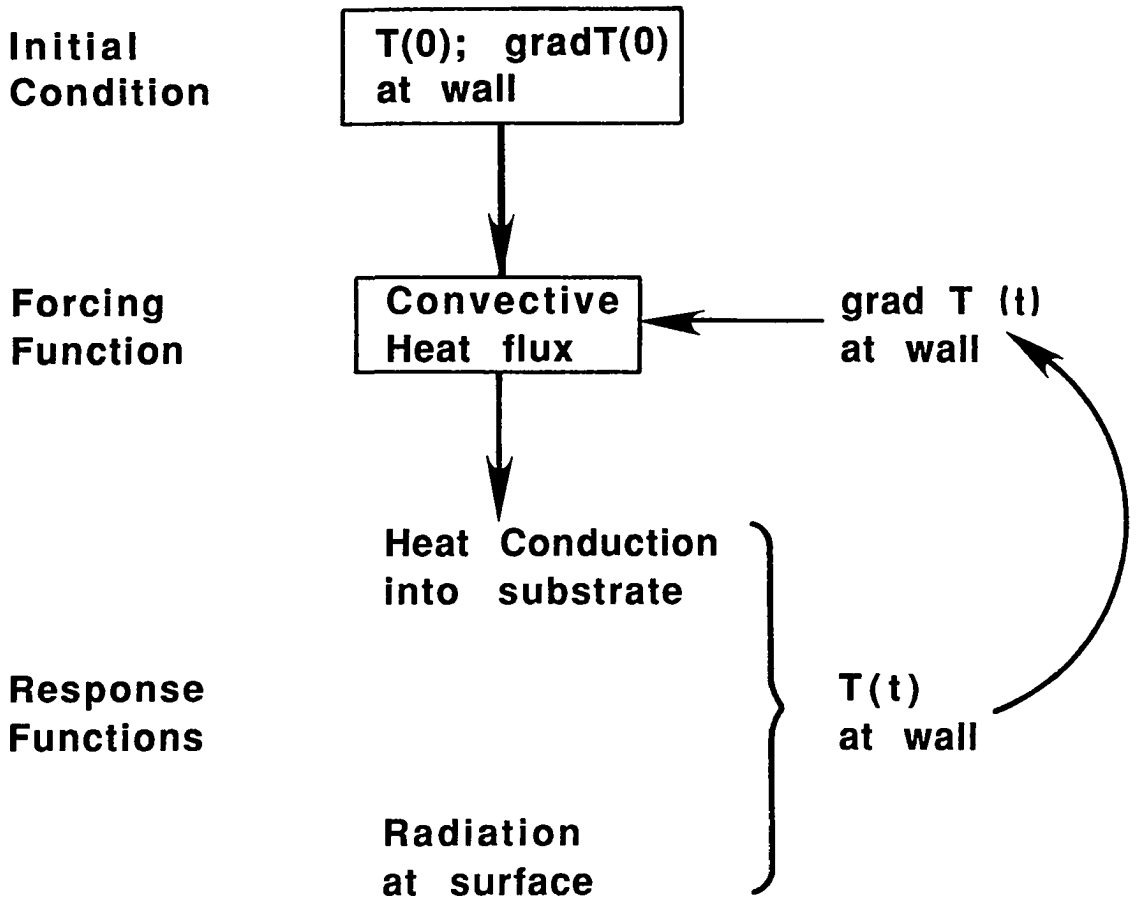

Fig. 5.7 The closed loop of surface temperature distribution in a body–airflow interaction

relatively easy to compare with experimental data obtained as thermographies. The whole concept is presented in Fig. 5.8, and a first step toward demonstrating the comparative results is shown in a subsequent section.

5.5 A Two-Dimensional Model of the Flat Plate Experiment

The flat plate experiment described in the first half of this chapter, was considered ideal for an attempt to validate the concept discussed in the previous section. Several factors contributed together to establish this estimation. The most important one related to the fact that the geometry being very simple, the boundary layer flow, the heat conduction into the substrate and the heat radiation are mathematically well understood and no major difficulties could be foreseen with the modeling and solution of the problem.

The following decisions were taken as a part of the modeling process:

1. The temperature distribution of the flat plate is calculated by a two-dimensional finite difference method of solution.

2. For the surface nodes, the temperature change is deduced from an energy equation, of the type,

$$\frac{\partial T}{\partial t} = \frac{1}{m \cdot c} \Sigma \dot{q} \qquad (5.10)$$

where m is the mass of each finite differencing control volume, c is the specific heat of the substrate, and $\Sigma \dot{q}$ is the balance of energy on that element summing up the contributions by conduction, convection, radiation and generation.

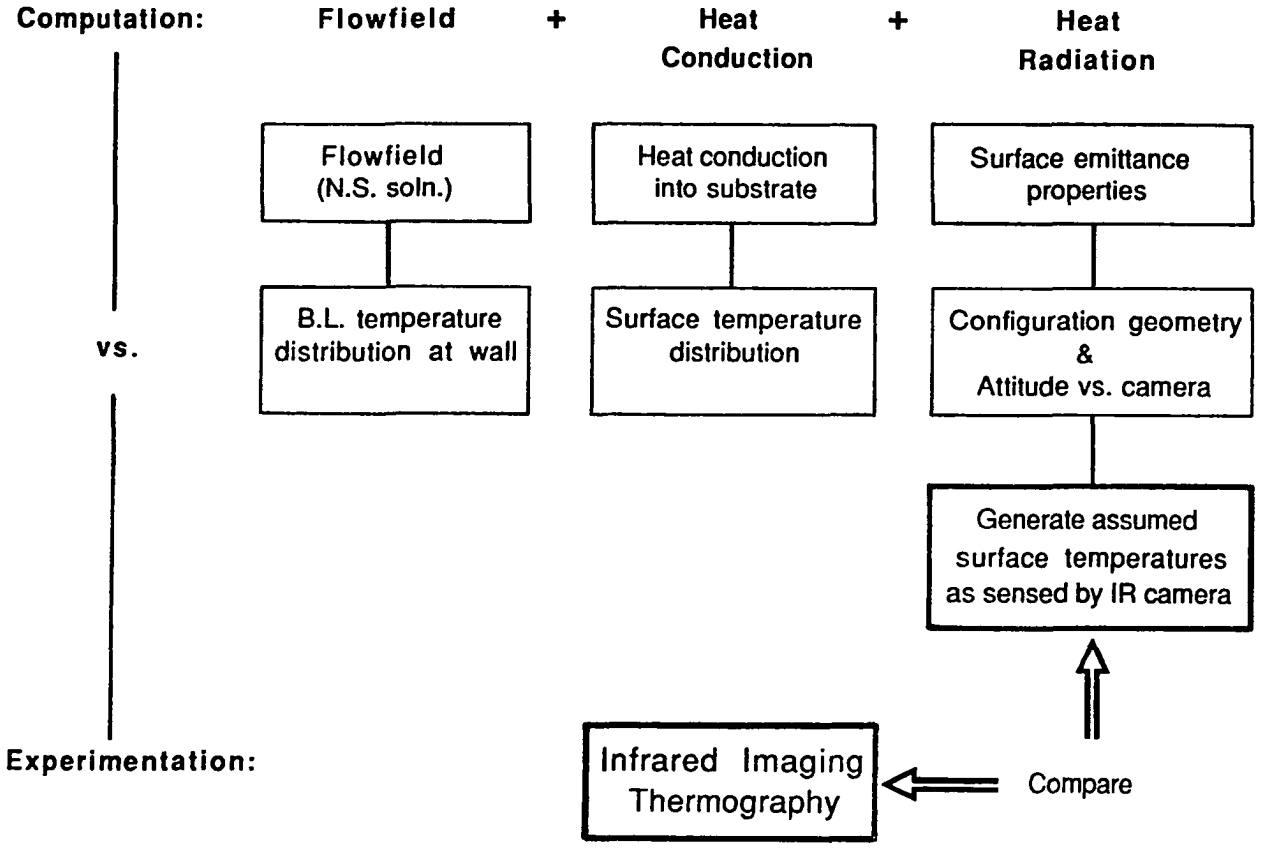

Fig. 5.8 Proposed method for infrared imaging evaluation of aerodynamic calculations

3. For all the interior nodes, the temperature change is calculated from the transient heat conduction equation:

$$\frac{\partial T}{\partial t} = \alpha \nabla^2 T \qquad (5.7)$$

4. An explicit, forward-difference technique is chosen for the algorithm formulation, which invokes a marching-type solution strategy in space and time.

5. The heat radiation from the flat plate is accounted for through the Stefan-Boltzmann Eq. (5.9).

6. The convective cooling of the flat plate is calculated using results from the boundary layer theory. Specifically reference is made to:

   (a) For the upper and lower surfaces, use of the constant free-stream velocity flow along a semi-infinite plate with arbitrarily specified surface temperature (Kays and Crawford, 1980, p. 148).

   (b) For the leading edge wedge surface, use of the heat transfer for constant-property laminar boundary-layer flows with power-function free-stream velocity and wall-temperature variations, as developed by Levy (Burmeister, 1983, pp. 308-309).

7. Uniform heating applied all around the surface of the flat plate.

Figure 5.9 summaries the various aspects of the model, and a detailed account of the working formulae is given in Appendix B3.

The greatest problem encountered in putting this heat transfer simulation to work was the assessment of the substrate physical

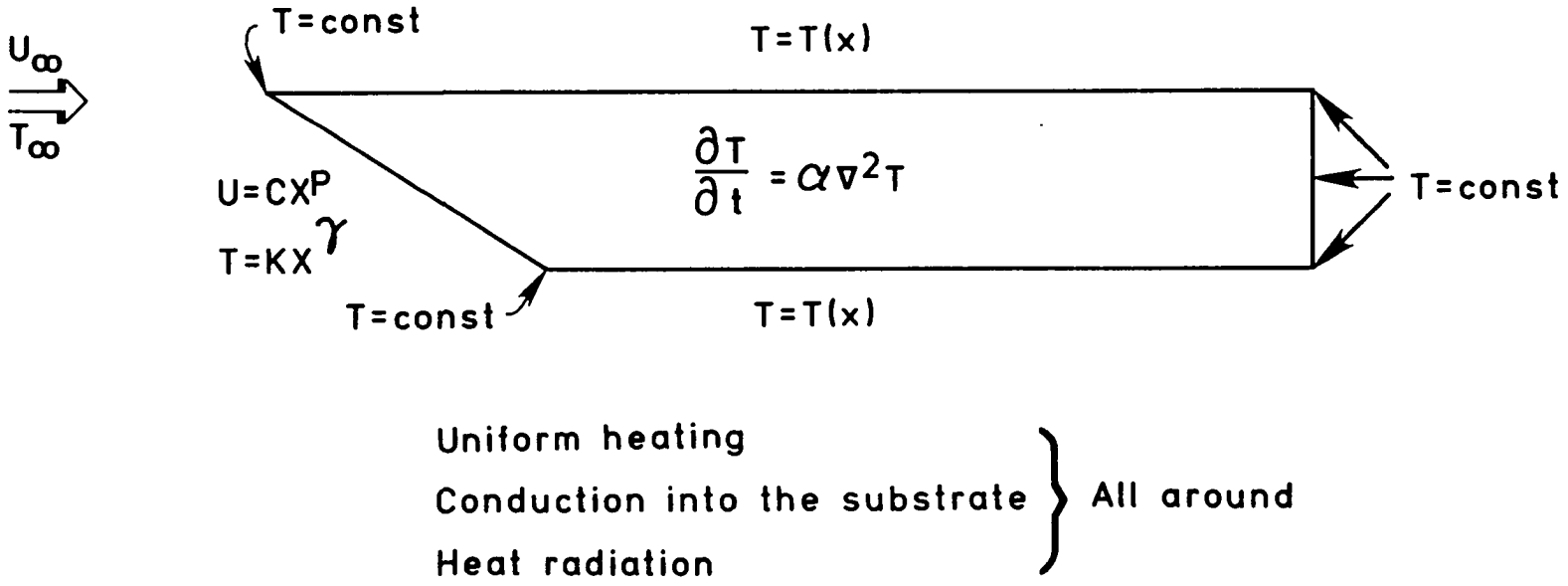

Fig. 5.9 Heat transfer models and assumptions used to calculate the surface temperature distribution for the flat plate experiment

properties. Generally speaking the wood was identified as pine (probably yellow pine). However, the leading edge (the first 40 mm) was made of green wood, while the rest of plate was made of cured wood. The references that have been consulted with regard to wood properties gave widely different values for its physical constants. The only issue agreed upon between the various references was that inside the group of so called "softwoods" (fir, pine, spruce) those properties and their statistical spread is very much the same. Data in the ASHRAE Handbook of Fundamentals (Chap. 30) almost doesn't make distinction between fir and pine properties for example. The lowest conductivity value was found to be 0.038 W/mK, perpendicular to grain (Bird, Stewart and Lightfoot, 1960, p. 249), and the highest one was 0.35 W/mK, parallel to grain (McAdams 1954, p. 451). The density was found to vary between 416.5 kgm/m^3 (Eckert and Drake, 1972, p. 783) to 551 kgm/m^3 (McAdams, 1954, p. 451). Good agreement was found between the various sources with regard to the specific heat (see Appendix B3). Therefore the problem was what conductivity values to assign to the wooden substrate. The best thing to do in order to understand this problem is to look at the ends (cross section) of the plate material itself. The grain character indicates the extent to which the wood is anisotropic and heterogeneous. Therefore, the conductivity values used throughout this investigation were the result of judgement and evaluation relating to the agreement between the experimental data and the computation.

The first calculation was with a uniform wood conductivity, k_w, value of 0.107 w/mK. While the behavior on the last half of the scanned top surfaces was satisfactorily reproduced, the behavior near the leading edge was not. The experiment showed a very gradual increase of

the surface temperature, while the model predicted a much steeper one. The discrepancy perhaps can be explained noting the fact that the leading edge being made of green wood, its conductivity was higher than over the rest of the plate with resulting lower surface temperatures. To improve the model, two k_w values were assigned: 0.17 w/mK for the leading edge region and 0.105 w/mK for the rest of the plate. Although this improved very much the agreement between the computation and the experiment, the results were still not perfectly matched. A last attempt was made to take into account not only the difference between the wood of the leading edge and the main plate, but also its directionality. With this in mind, two groups with two values each were used for the thermal conductivity. For the leading edge: k_w = 0.173 w/mK along the grain and 0.104 w/mK across the grain. For the rest of the plate, k_w = 0.075 w/mK along the grain and 0.045 w/mK across the grain were chosen. This combination gave the best agreement with the experimental results as it can be seen in Fig. 5.10. The correlation between the experimental set of values and the calculated one is 0.88. In spite of this, the prediction is still not very good. One possible cause may be that the hetrogeneity of the wood is too high for it to be modeled by just two conductivity values. A second possibility may be related to the fact that the model of constant heat flux into the substrate doesn't accurately represent the physical reality. Since only a relatively narrow chordwise strip is heated on the plate, there may be significant heat conduction laterally to the substrate. For this to be included in the model, one has to take into account not only the chordwise heating distribution (as was done) but also the transverse distribution at least in the substrate, as shown in Fig. 5.4.

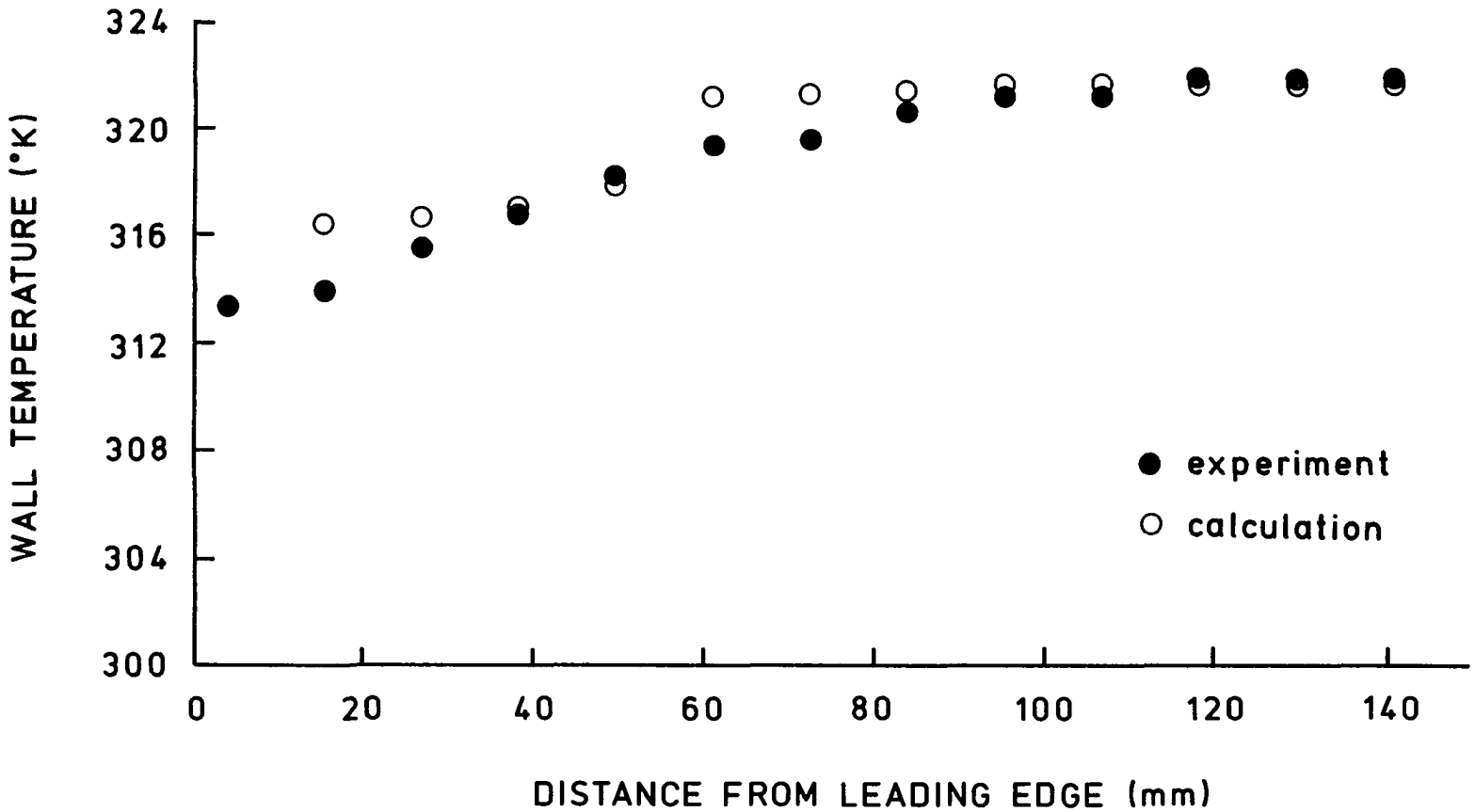

Fig. 5.10 Flat plate experiment: experimental vs. computed results

In what follows, a brief evaluation is done relating the influence of the three heat dissipation mechanisms involved in this experiment on the chordwise temperature distribution. The forced convection influence is greatest in the leading edge region, because the heat transfer coefficient decreases with $\sqrt{x}$. The radiation heat transfer will work against establishing high surface temperatures, especially towards the rear of the scanned area through the T_w^4 dependency. The conduction will work to equalize the temperatures between the lower temperatures near the leading edge and the higher temperatures downstream on the plate, through the temperature gradient mechanism.

On the time history aspect of the experiment, it is clear that initially most of the surface heating goes into the substrate to raise its temperature. It is only after about 10 seconds that the temperature distribution on the surface starts to be significantly higher than the ambient, that the convection and radiation mechanisms start to play an important role in the energy transport processes. The surface equilibrium temperature is achieved faster with increasing surface heat generation. In the present case of low heating rates, the time period to achieve it is of the order of minutes.

A further remark concerns the temperature spike that is consistently seen experimentally at the leading edge. If the previous assumption (Sec. 5.3) that the substrate there is too small to dissipate effectively the heat by conduction is true, then it is also true that the actual heat flux there is much above the mean heat flux used in the model. In fact, the heat generation value based on the circumferential area of the wire gives a value of $\dot{q}_o'' = 36528\ w/m^2$. The computer program clearly captured the temperature spike at heating rates of

10000 w/m^2 after very short periods of time. This evidence supports the model presented above.

5.6 Summary

The infrared imaging system is an effective, non-intrusive device for measurement of surface temperatures with position and time dependent temperature distributions. Its capability of mapping rapidly entire surfaces is unmatched by any other means existing today. Furthermore, for aerodynamic configurations, the surface temperatures provide important information about body interaction with the external airflow. This was basically shown for the case of a flat plate in the laminar boundary layer regime at constant wall heat generation rate.

The concept of using infrared imaging systems in aerodynamic research as a direct CFD codes validation tool was introduced. In general, it can be stated that the surface temperatures of a body in a flowfield is time dependent even for steady state flows. The modeling effort pointed out the importance of using substrate materials with known and well understood thermal properties. The wood itself proved to be a very poor choice to be used in aerodynamic experiments where the thermal aspects are of primary interest. A great degree of uncertainty in the analysis was introduced due to the internal structure of the wood and its associated directionality and non-homogeneity effects.

Chapter 6

BOUNDARY LAYER REGIMES ON A NACA 0012 AIRFOIL

The next step after the flat plate laminar boundary layer experiment was to expand the investigation to a two-dimensional NACA 0012 airfoil at various angles of attack from zero up to a post separation angle. Such an experiment offered the opportunity to validate the applicability of infrared imaging systems to aerodynamic research on a real aerodynamic geometry, and to provide some new information, for boundary layer flows extending all the way from fully attached laminar regime through transition to turbulence, and up to separation. Furthermore, the extension of this method to three-dimensional geometries and higher Reynolds numbers flows can be easily implemented following the success of these experiments.

6.1 The Experiment Viewed in Perspective

The detection of boundary layer transition from laminar to turbulent regime or its separation from the surface of interest, is still one of the most challenging subjects in aerodynamics. Almost any available experimental technique is used for this kind of studies: smoke visualization, laser Doppler velocimeters, tufts, chemical sublimation (acenaphtene), oil flow, hot films and hot wires, phase change paints, liquid crystal paints, pressure measurements, optical techniques etc. With all these methods, the subject is far from being closed and the search for more rewarding techniques is still going on.

As was already pointed out in the literature survey, infrared imaging systems have already been successfully used in the recent past to detect transition both in flight and in wind-tunnel testing. However, detection of separation with IR imaging systems is still an open subject because the heat transfer behavior itself in separated flows still resists accurate prediction. Also, no validation of the IR imaging system findings was done in the very same experiments by any independent means. Therefore, trying to detect both the transition and the separation during the same experiment is a contribution in itself, even more so when the airfoil under investigation has a NACA 0012 profile. Although quoted as the most widely investigated airfoil, firm and reproducible results with regard to the boundary layer behavior about this airfoil is still missing (McCroskey, 1987).

6.2 The Experiment Set-Up

As shown in Fig. 6.1, the experimental system consisted of a NACA 0012 airfoil mounted vertically at one end of a rotating arm, at the other end of which was mounted the infrared imaging camera. The set-up was installed in a 0.9x1.2 m (3'x4') low speed, closed circuit wind tunnel. As the arm rotated around its center, the airfoil changed its angle of attack, but the camera remained in a fixed, perpendicular position relative to the airfoil chord. The angle of attack α, could be fixed within ± 0.5 degree of the desired value. The airfoil had a chord of 0.3048 m (one foot), an aspect ratio of 1.5 and it was clamped betwen two end plates measuring 35.5 x 7.62 cm (14"x3") in order to reduce the three-dimensional flow effects of the tips. At zero angle of attack the airfoil was at a distance of about 10 cm from the wind-tunnel

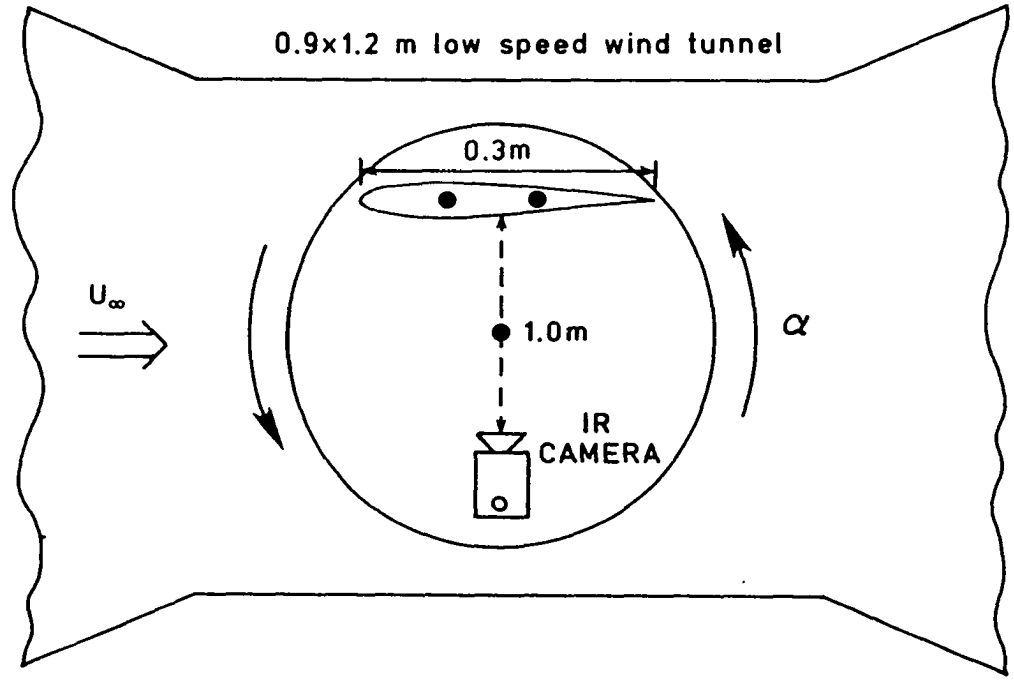

Fig. 6.1 Schematic top—view of the IR camera—airfoil mounting on a turntable used for wind tunnel flow separation studies

side wall, and the camera was similarly spaced near the opposite wall. While this arrangement did affect the airflow around the airfoil (by blockage and by wall proximity), the basic objective of the experiment, to detect separation with the IR imaging camera, was not hampered. The observations are reported as they were made i.e., with no corrections to account for the wall proximity. In order to eliminate any possible spurious reflections from the airfoil to the camera, a 0.152 mm thick black matte paper was bonded to its surface with double-sided Scotch® tape wrapped chordwise around the airfoil with a 3 cm pitch. Figure 6.2 displays the following features of the airfoil:

(1) Decimal subdivision of the upper surface arc length (further referred to as "s") was provided, where the lower and the upper divisions were marked respectively with highly reflective silver paint and ultrafine gold leaf to be visible on the IR imaging system display. A posteriori, it can be concluded (see Fig. 6.4) that both the silver paint and the gold leaf markings performed equally well, and since the silver paint is easier to apply it may be considered as the preferable choice.

(2) Above the arc subdivisions, four rows of aluminum foil tufts 0.0254mm thick and 2mm wide were threaded through the paper in increments of one-tenth of the surface arc length (0.1s) to permit their observation both visually and with the infrared imaging system.

(3) The surface was locally warmed by passing an electric current through a 0.127mm (0.005") Constantan wire that had been wrapped

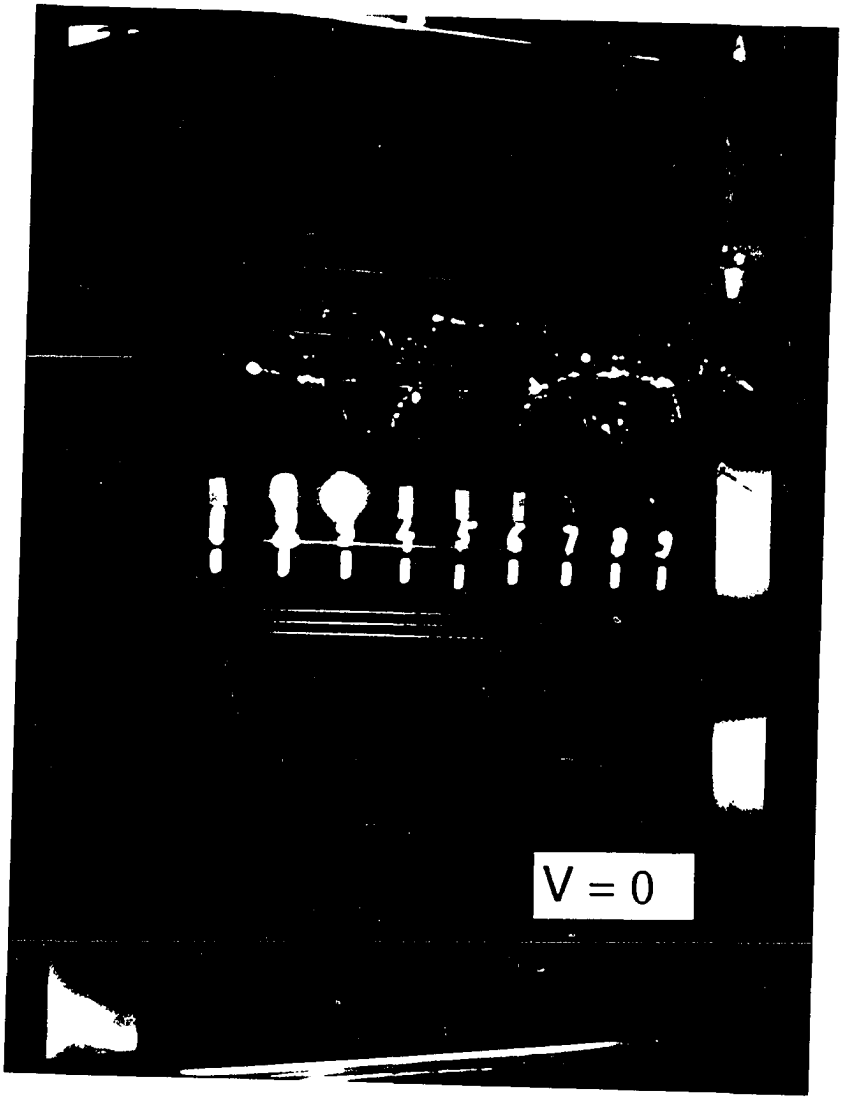

Fig. 6.2 NACA 0012 airfoil with aluminum foil tufts in still air.

chordwise around the airfoil underneath the black paper, at the following locations:

(a) below the arc markings - to allow temperature measurements chordwise on a smooth, uncontaminated airfoil surface,

(b) directly under the arc markings - to enhance their observability with the IR imaging camera, and,

(c) under the tufts, for the same reason.

The mean heating flux was approximately 500 W/m^2, with no noticeable effect on the boundary layer based on the localized and smooth behavior of the chordwise surface temperature under the arc markings (item (a) above). The span-wise coordinates of these heating wires can be seen on Fig. 6.2, marked by pencil on the black paper just below the arc markings. The uppermost and lowest lines demark the field of view of the camera.

6.3 The Experiment Description

The airfoil angle of attack was varied between 0° and 16°. Photographs of the airfoil surface were taken under steady state conditions with a 35 mm single lens reflex (SLR) camera, and of the IR imaging system display unit (oscilloscope face) using a Polaroid camera. In a separate series of experiments, the airfoil angle of attack was varied between 0° and 16° in increments of 2° at 2 seconds intervals, and the thermographies were recorded on 5 1/4" diskettes by the system's dedicated microcomputer.

The rationale behind the above steps was to validate by visual observations the tufts patterns taken with the IR imaging system, and to validate the temperature analysis performed on the microcomputer against instantaneous observations of the airfoil surface and tufts made with the IR imaging system display unit. This way, future investigations can rely entirely on observations performed with the IR imaging system. While it is true that the tufts themselves induce an early transition, their contribution to the detection of separation is irrefutable. Furthermore, transition induced by the tufts can be clearly seen on the IR imaging display.

The wind tunnel experiments were carried out at a nominal Reynolds number of 375,000, based on the airfoil chord. As the wind tunnel air heats up during operation, two opposite thermal effects take place concurrently on the airfoil surface: convective cooling of the electrically heated surfaces and convective heating of the cooler surfaces due to the heating of the free stream wind-tunnel air above ambient conditions. The lateral conduction of heat was negligible, as it could be traced back on the thermographies.

The heating-up of the wind-tunnel during its operation had a negative effect on the quantative interpretation of the computerized thermographies. In principle, the aim of this experiments is to look for surface temperature differences caused by changes in boundary layer regime. Qualitatively, the change should be from lower surface temperatures under the laminar regime to higher temperatures under the turbulent (see next section). However, at the same time there is an additional heating effect due to the heating of the freestream air in the wind tunnel. Thus, the usefulness of extracting temperature

differences from thermographies taken at different angles of attack, loses its usefulness due to lack of a common freestream temperature. In other words, as the angle of attack of the airfoil is increased, there is an increase in surface temperatures due to changes in the boundary layer regime, and at the same time an additional change due to the air heat-up. Therefore, a posteriori, it can be remarked that the computerized thermographies could not be meaninfully interpreted and their use was discarded. At the same time, it is emphasized that this argument has nothing to do with regard to the determination of the transition line from the thermographies. On the contrary, the heating-up of the air only enhances the demarcation line of the transition.

6.4 Results and Discussion

The results reported herein are based on the observations made over 20 different experiments. Figure 6.3 shows a sequence of the airfoil photographs taken of the airfoil surface with a 35 mm SLR camera, for angles of attack varying between zero to 13 degrees. These pictures partially document the tufts behavior as they could be observed visually. The word "partially" is used here because continuous visual observation of the tufts offer more information than still photographs, especially with regard to the unsteady behavior of the flow. Figure 6.4 shows a similar sequence of pictures, this time as observed on the infrared imaging system display. The pictures were taken with a Polaroid® camera and later reproduced with a 35mm SLR camera. These pictures clearly show that the tufts behavior is simultaneously observable with the IR imaging camera, and therefore it is sufficient for future experiments to rely solely upon one set of photographies only, namely those taken from the IR imaging system display.

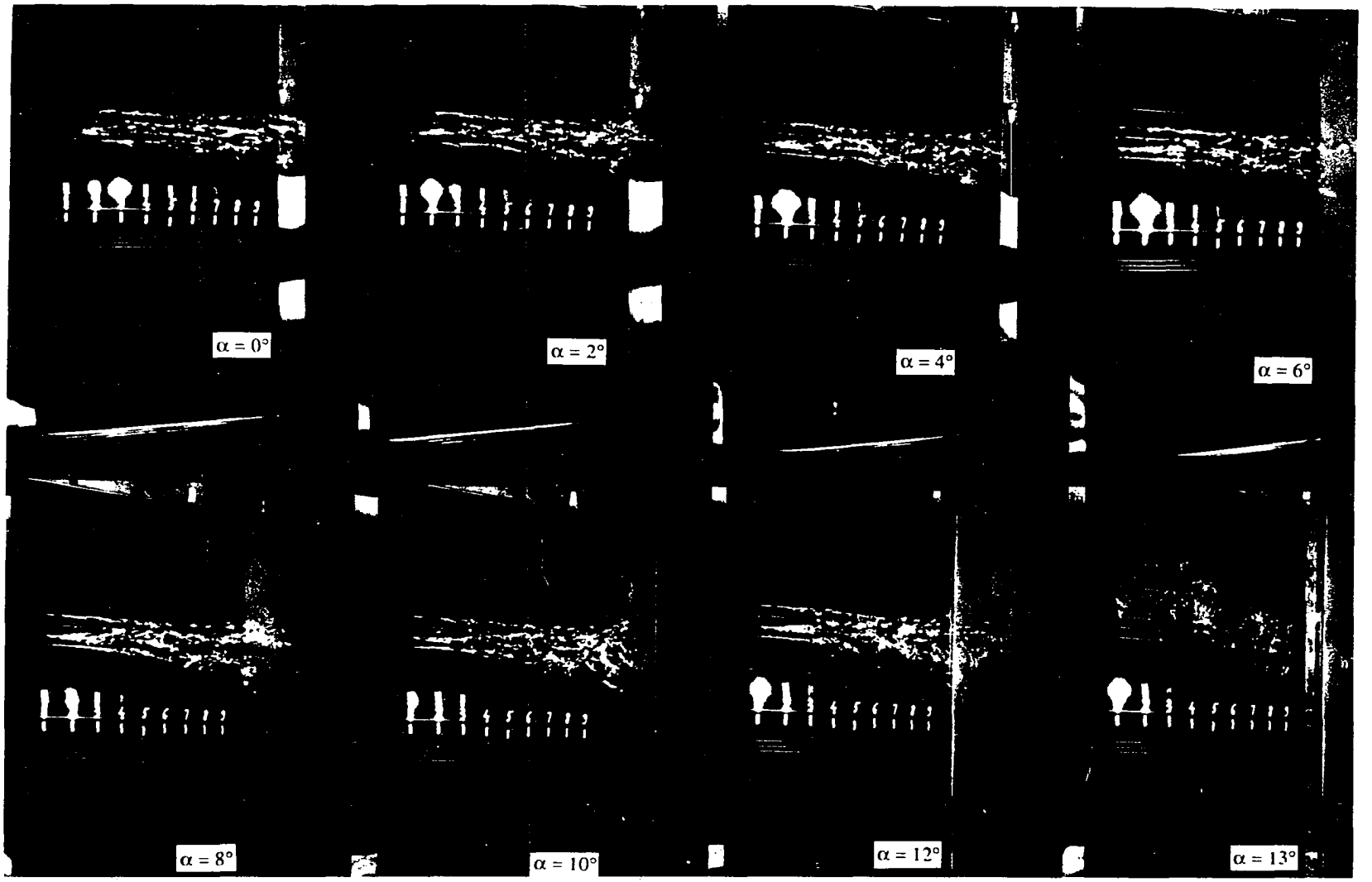

Fig. 6.3 NACA0012 airfoil with aluminum tufts at various angles of attack in wall proximity. Re_c = 375000. 35mm SLR camera photos. Air flows from left to right.

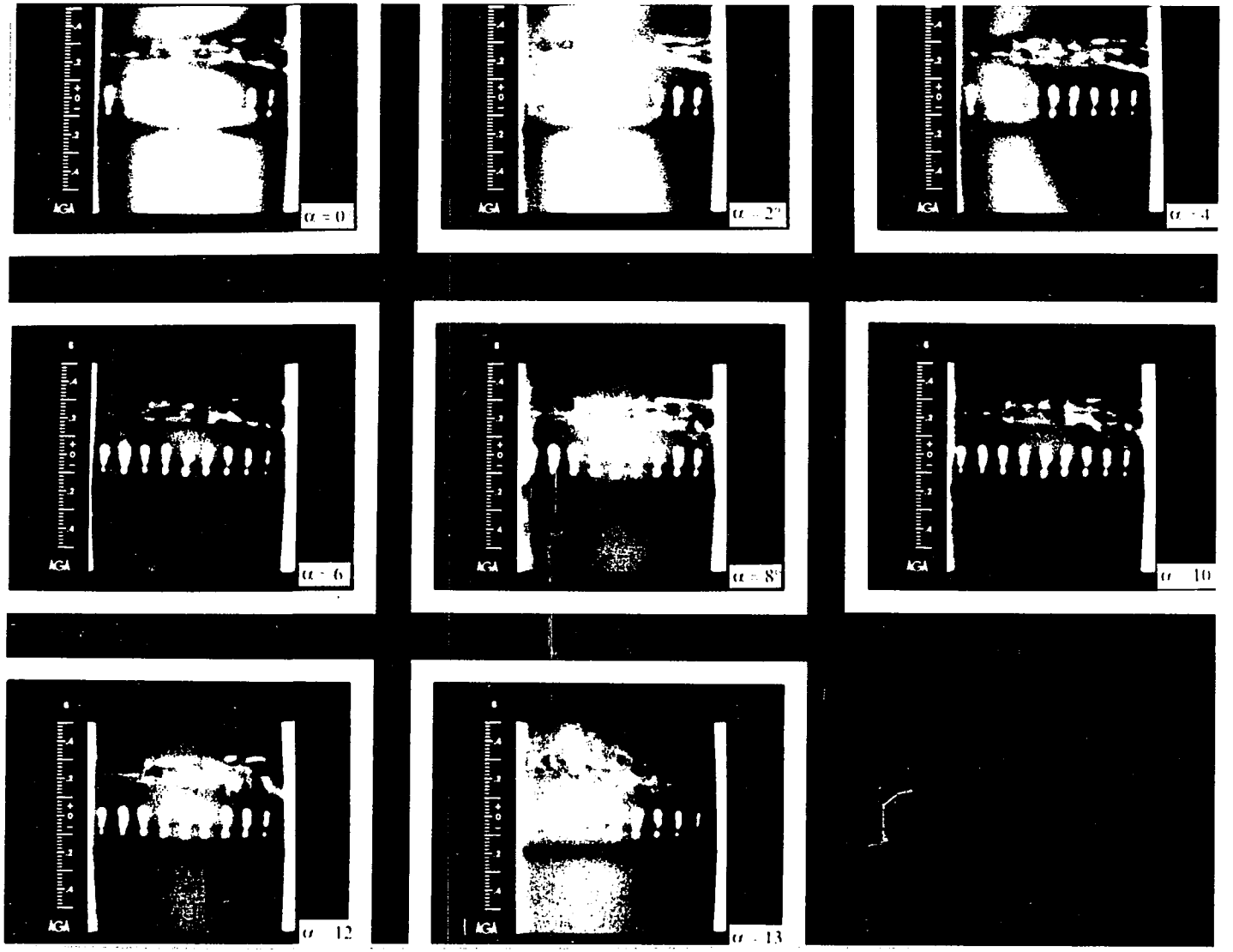

Fig. 6.4 NACA0012 airfoil with aluminum tufts at various angles of attack in wall proximity. Re_c = 375000. Photographs of the infrared imaging display in inverted mode. Air flows from left to right.

Before going into the analysis of the main results, the facts on which the transition detection by thermography is based will be briefly reviewed. According to the Reynolds analogy

$$St = \frac{c_f}{2} \quad \text{or} \quad \frac{Nu}{Re\ Pr} = \frac{c_f}{2} \tag{6.1}$$

since under our assumption Pr = 1

$$h = \frac{1}{2} c_f \frac{U \cdot k_a}{\nu_a} \tag{6.2}$$

where h is the local heat transfer coefficient c_f is the local skin friction coefficient, U is the local velocity outside the boundary layer, ν_a is the air kinematic viscosity and k_a is its conductivity. According to Eq. (6.2), the local heat transfer coefficient is directly proportional to the local skin friction coefficient. Since during transition from laminar to turbulent regime, the skin friction coefficient jumps approximately by an order of magnitude, by Reynolds analogy the heat transfer coefficient also jumps by an order of magnitude. Thus, a clear "jump" in the wall temperature should be seen on the thermography as transition is induced. The temperature jump was shown to mark the transition region by prior workers (Bouchardy et al.; 1983, Quast, 1987), and can clearly be seen in Fig. 6.4, for example at $\alpha = 4°$ at the 0.35s location, on the arc markings. Finally, regarding the thermographies displayed in Fig. 6.4, it should be mentioned that they were taken with the display unit set to the inverted mode which produces darker shades for higher temperatures. This choice was dictated by the fact that the tufts status can be better seen in the inverted mode than in the normal mode. Thus, in Fig. 6.4, the darker shades represent higher apparent temperatures than the lighter shades.

The main experimental results will be discussed after giving a brief description of what is believed to happen on the NACA 0012 airfoil at the Reynolds number of 375,000 as the angle of attack is increased. This account is based on the visual tufts observation in these experiments as well as on the accounts of Carr et al. (1977, p. 3), McCullough and Gault (1975), and Thwaites (1987) pp. 200-205. At zero angle of attack, the flow is usually laminar over most of the airfoil. As the flow approaches the trailing edge, the laminar boundary layer separates with subsequent transition to turbulent flow. The expansion of the turbulent motion causes reattachment of the boundary layer as a turbulent one which remains attached up to the trailing edge. This localized region of laminar separated flow is called the laminar separation bubble. The air motion inside this bubble is circulatory with typical velocities of one order of magnitude lower than that of the free stream velocity (Brendel and Mueller, 1988). The length of the bubble is a few percent of the chord. As the angle of attack is increased, the bubble and the transition region above it move upstream, thus increasing the airfoil area subjected to turbulent flow. At a certain point, the turbulent boundary layer fails to negotiate the adverse pressure gradients and part of the turbulent boundary layer separates, usualy near the trailing edge. This phenomenon is known as turbulent separation. As the angle of attack is further increased, the bubble moves upstream as does the point of turbulent separation, thus causing the gradient of the lift curve versus the angle of attack to decrease. As the bubble reaches the leading edge, and the angle of attack is still increased, the separation point of the turbulent boundary layer moves more and more upstream, the bubble remaining

relatively small and attached close to the leading edge. At a certain angle of attack (stall angle), the adverse pressure gradient can reach values where reattachement of the turbulent boundary layer is no longer possible. This causes the bubble to burst over the entire surface of the airfoil from the leading to the trailing edge, causing what is known as "leading-edge bubble-bursting stall."

The main findings of the experiments (visual and IR imaging observations) are summarized below, followed by a discussion of some interesting points worthy of elaboration:

$\alpha = 0$ Laminar flow up to 0.8s on the clean surface,
Tufts induced transition at 0.6s

$\alpha = 2°$ Transition at 0.7s on the clean airfoil (lower part),
Tufts induced transition at 0.5s,
High amplitude tufts fluttering after 0.7s

$\alpha = 4°$ Transition at 0.5s on the clean airfoil,
Tufts induced transition at 0.3s,
Higher amplitude tufts fluttering after 0.7s

$\alpha = 6°$ Transition at 0.2s on the clean airfoil,
Tufts induced transition at 0.2s,
Turbulent separation seen on tufts at 0.8s

$\alpha = 8°$ Transition at 0.1s on all the airfoil,
Turbulent separation at 0.7s

$\alpha = 10°$ Fully developed turbulent flow all over the airfoil,
Turbulent separation at 0.6s

$\alpha = 12°$ Turbulent separation at 0.3s with flow buffeting, "Steady" separation at 0.5s

$\alpha = 13°$ Bubble burst; complete separation.

The first observation relates to the fact that the region of flow reversal due to separation could be very well seen in the tufts motion. Similarly, fully developed turbulent boundary layer flow could be identified in the tufts motion as a considerable increase in their flutter rate and amplitude. As indicated by the tufts behavior, the turbulent boundary layer separation point was not stable with respect to time. Just after the separation had first been observed, oscillations of the separation line back and forth over one-tenth of a the surface could be observed. Just prior to separation, these oscillations grew in amplitude up to one quarter of the surface.

The second observation refers to the detection of the laminar separation bubble. In Fig. 6.4, this bubble can clearly be seen on the $\alpha = 6°$ thermography at 0.15s as a lighter shade curved strip. Since at the separation point the first derivative of the velocity, $\partial u/\partial y$, is zero, so is the local skin friction coefficient c_f, and also the heat transfer coefficient h. Therefore, the bubble appears as an area of lower temperatures due to the lower local convective heating on a cool surface. However, its observability depends on a very fine tuning of the "thermal level" knob of the display unit, which may be detrimental to the capture of other features, and may raise questions with regard to the reproducibility under any arbitrary conditions. Incidentally, the extent of the bubble for $\alpha = 6°$ can clearly be seen in this case to be about 10% of the upper surface.

The third observation relates to the fact that for steady state conditions such as those under which the photographs in Fig. 6.4 were taken, no substrate heating was necessary for enhanced observability. It seems that the heating of the wind tunnel, which in this case was 1.2K/minute was more than enough to get a sharp image on the system's display. Also, the substrate chordwise heating can be seen to have a well defined and localized effect (see Fig. 6.4).

The fourth observation relates to the stall angle of attack. For the present test Reynolds number, stall at 13° is somewhat premature. Hansman and Craig (1987) for example report a stall angle of 14° for the NACA 0012 at a Reynolds number of 310,000. This premature stall could be expected considering the fact that the airfoil was placed near to and spanwise parallel to the wind tunnel wall. This assembly geometry caused the airfoil to operate "in ground effect" which has a net effect of increasing the actual angle of attack (Rae and Pope, 1984, p. 418). In order to check the correctness of this assumption, the airfoil was temporarily moved close to the center of the wind-tunnel. A few runs at the same Reynolds number showed repetitively that in this position the airfoil did indeed stall at 14 degrees.

A closer look at Fig. 6.4 provides more detailed insight and helps correlate the observations with the flowfield features. For this purpose, the clean, undisturbed surface of the airfoil in the lower half of each thermography is noted.

The thermographies for α = 0, 2 and 4 degrees clearly show two heated zones. The first, starting at the leading edge is the effect of the convective heating under the laminar boundary layer regime. The

second, along the trailing edge and exhibiting a curved boundary shape is due to the effect of convective heating under the turbulent boundary layer regime. Just upstream of that curved boundary shape is the region where the transition from the laminar to turbulent regime takes place. As the angle of attack is increased from zero to two and from two to four degrees, the transition region, as expected, advances upstream. The next four thermographies from $\alpha = 6°$ to $\alpha = 12°$ display the flow regime where trailing edge turbulent separation is encountered. The main vortex resulting from the separation is located in that area, and since the turbulent mixing there is quite vigorous, the net effect is that heat is convected from the freesteam to the airfoil surface. In order to get a visual impression about the intensity of the turbulent mixing, the reader can consult Schlichting (1968, p. 36) where a visualization of a separated flow about an airfoil is reproduced from Prandtl-Tietjens. The value of the heat transfer coefficient in that area of separated flow is difficult to determine. However, measurements made by Schmidt and Wenner (see Schlichting, 1968, p. 298) on cylinders in the supercritical range (Re = 426,000) show a sixfold increase in the Nusselt number in the wake region immediately following the separation point, relative to the value immediately preceeding the separation point itself. This fact explains at least qualitatively why there is a net heating effect in the region affected by the trailing edge turbulent separated flow. The thermographies taken at $\alpha = 6°$ and $\alpha = 8°$ show the separation bubble moving upstream, and in this case remaining small as long as the flow remains attached on the forward part of the airfoil (Carr et al., 1977). As the angle of attack is further increased to $\alpha = 10°$ and $\alpha = 12°$, the stagnation point moves downward around the

leading edge and followed by the bubble, thus getting out of the field of view of the IR imaging camera. As the angle of attack is increased to $\alpha = 13°$, the stall angle is reached. However, the separation process is not immediate. It was observed on the tufts motion that at this angle of attack, the flow was extremely unsteady, the points of turbulent separation violently moving back and forth stream-wise before the flow separated itself completely from the airfoil. It did not look like the turbulent boundary layer failed to reattach (as is described in some references), rather it appeared as if the separated flow tried to penetrate into the attached flow region and "peel it off" from the surface. The separation occurred usually spontaneously, without any change in the airfoil condition, after a very few seconds from the moment the airfoil reached $\alpha = 13°$. The hystersis effect of the reattachment was also clearly seen, although no singular value for the reattachement angle could be fixed. It varied between 11 to 12 degrees. The reattachment itself was also preceeded by extremely unsteady flow and strong buffeting. Usually, it could take the flow three to four failed attempts until it managed to reattached. These findings are documented in Fig. 6.5. Based on the tufts observation, the only thing that can be said about the air motion in the separated flow regimes is that it was extremely unsteady and chaotic as can be seen in both Fig. 6.3 for $\alpha = 13°$ and Fig. 6.5.

The experimental results have been compared with predictions of the Eppler code (Eppler and Sommers, 1980). This code is accepted today as a good code with regard to inviscid and viscous flow calculations about airfoils. The code was run at a Reynolds number of 400,000. There is good agreement between the code and the experimental results regarding

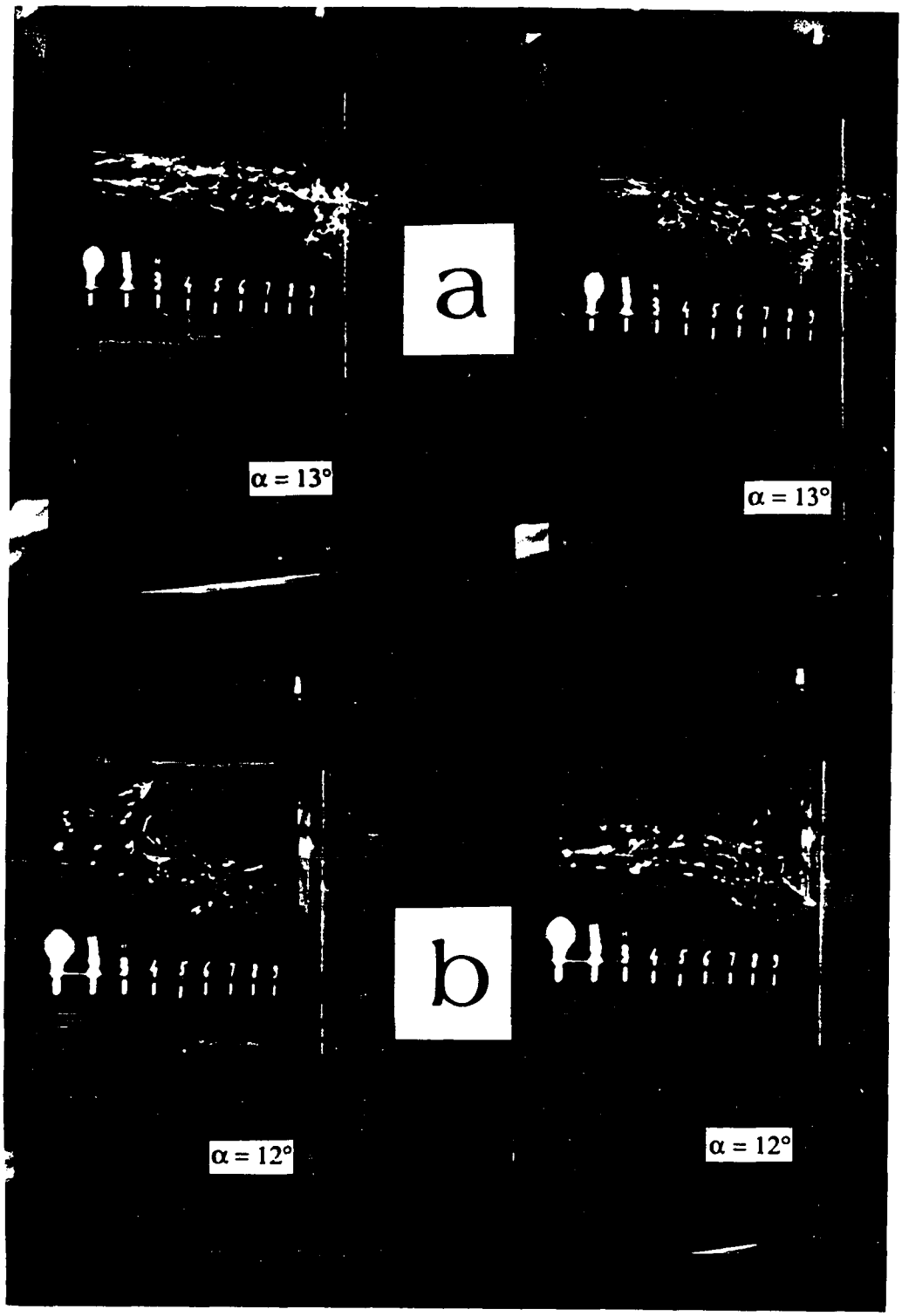

Fig. 6.5 NACA0012 airfoil (a) at separation (b) at reattachement incidence. Photographs for each set taken five seconds apart under identical conditions.

the stall angle. The code predicts it at 14 degrees, while this experiment showed it to be 13 degrees near the wall and 14 degrees in the middle of the test section. At angles of attack below the stall, the code consistently underpredicted the extent of the turbulent separation as well a its onset. The experiment detected the separation onset at six degrees (say seven degrees to account for the wall proximity) while the code predicted it at ten degrees angle of attack. The degree of agreement between the experimental results and the code prediction regarding the extent to which the airfoil surface is affected by the turbulent flow varies with the angle of attack. Up to four degrees, the code underpredicted the extent of turbulent flow approximately by a factor of two (for partial support of this claim see Ladson 1988, p. 90, Fig. 30(a)). For six and eight degrees, the agreement starts to be very good (20% to 10% deviations) and from ten degrees and up the agreement is excellent. These results are summarized in Table 6.1.

This chapter will be concluded with a final remark concerning the interpretation of the thermographies. Looking at Fig. 6.4, one can observe that the temperature information contained in each individual thermography is not enough in order to allow a meaningful interpretation in itself. For example, the thermography taken at 10 degrees angles of attack can be ambiguously interpreted as indicating laminar flow with transition to turbulent flow at 0.75s, the actual case being transition to turbulent flow near the leading edge and separation at 0.75s (The tufts indicating the separation at 0.65s). However, a sequence of thermographies, covering the whole range of angles of attack, from zero up to separation, do provide enough data in order to evaluate the

Table 6.1 Transition and separation studies over a NACA 0012 airfoil at different angles of attack: experiment vs. Eppler code (Re_c = 400,000)

α	s_{turb}[1] thermography	s_{turb} Eppler	$s_{separated}$[1] tufts	$s_{separated}$ Eppler
0°	0.2	0.4	0.0	0.0
2°	0.3	0.6	0.0	0.0
4°	0.5	0.8	0.0	0.0
6°	0.8	1.0	0.2	0.0
8°	0.9	1.0	0.3	0.0
10°	1.0	1.0	0.4	0.1
12°	1.0	1.0	0.7	0.5
14°	1.0	1.0	1.0	0.9

[1]In wall proximity.

development of the boundary layer regime, from almost entirely laminar, through partially laminar, turbulent and separated and up to fully separated flow.

6.5 Summary

The separation studies performed on the NACA 0012 airfoil showed that aluminium foil tufts can be observed with infrared imaging systems. This fact opens the possibility to use the infrared imaging system as a flow visualization and surface temperature measurement device at the same time. As shown by other researchers, the transition and the laminar separation bubble are indeed observable with the IR imaging system. A rather intense heat transfer process is seen to exist on the upper airfoil surface under the turbulent separated regime. Both the flow separation and the reattachment were observed to be time-dependent phenomena. This research opened a question with regard to the actual mechanism that leads to the total flow separation over an airfoil at the stall angle. While the phenomenon is referred to in the literature as the failure of the turbulent boundary layer to reattach after the transition bubble, the observation of the tufts behavior indicated a "peeling off" effect of the separated flow region on that part of the boundary layer that is still attached.

Chapter 7

CLOSURE

7.1 Review of the Main Results

The essence of the heated wire technique is to place a very thin and very long electrically heated wire in an airflow, the measurement of the temperature distribution along the wire with the IR imaging camera being a direct indication of the flow speed behavior. Furthermore, since the heat conduction and radiation are negligible compared to the convection, Nusselt number correlations can be used to calculate that airflow velocity component that is perpendicular to the wire. This experimental method may be considered as non-intrusive since the wire end supports, and the IR imaging camera, are out of the flowfield. More importantly, the wire itself is very long, very thin and slightly heated, and therefore it doesn't really disturb the flowfield significantly. This method is not to be confused with the hot wire technique, where the support itself is immersed in the flow at the point of interest.

The heated wire technique was evaluated using as a target flow a laminar flow circular jet. This type of flow produced large temperature gradients along the wire, up to 2200K/m. Starting at a temperature gradient of about 350K/m, it was observed that the IR imaging camera has difficulties in producing accurate temperature results. Furthermore, the measurement error grew nonlinearly with the temperature gradient.

It was determined that this phenomenon is associated with the very nature of this IR imaging camera and probably has to do with its minimum resolvable temperature difference performance (Ohman). The roots of this behavior could be tracked through the field of view and instantaneous field of view to the size and the characteristics of the camera detector element itself. However, this actual measurement error is always on the negative side of the output, i.e., the readings are always less than the true temperature. Since the measurement error is well behaving with respect to the temperature gradient, it is possible to produce a calibration curve of the error versus the temperature gradients. Therefore, at least to a first order, the experimental data can be corrected to get a temperature distribution that is closer to the reality. This process can be repeated by trial and error, until the final corrected temperature distribution produces such a temperature gradient distribution that when substracting the errors, corresponding to the adjusted temperature values, the original experimental distribution is recovered.

The inverse approach of using the temperature readings and Nusselt number correlations to deduce the velocity distribution of the jet was shown to work in principle. With regard to this approach, it was shown how important it is to work with accurate data, because of the great sensitivity of the velocity function to the temperature values. Unfortunately, error sources include not only the IR imaging system, but also the heat transfer correlations themselves. As it was found out from the literature survey, this subject is far from being completely understood and therefore this problem should be looked upon from the broader aspect of the convective heat transfer discipline. The heated

wire concept was also shown to work for more general flowfields e.g., cylinder wakes in wind-tunnel experiments, with very promising results.

Infrared imaging thermography has been previously used to determine convective heat transfer rates without paying attention to the development of boundary layer flow. This work has shown that it is possible to track the thermal boundary layer development over a surface by measuring the surface temperature distribution with the IR imaging system. The method was proved on a flat plate at zero angle of attack, slightly heated chordwise at a constant power rate. The attempt to reproduce the experimental results with the computer calculation showed how important is to work with a homogeneous substrate whose thermal behavior is well understood; the use of unknown wood characteristics introduced large uncertainties in the computed results. In analyzing the experimental results, it is important in this case to account for all of the three modes of heat transfer: convection, conduction and radiation. Also, it is important to remember that due to the development of the thermal boundary layer over the surface of interest, the balance between the relative contributions of the three may change. In general, the surface temperature distribution was shown to be time dependent even for steady state flows, due to the evolving nature of the substrate thermal coupling with boundary layer heat exchange. Therefore, a single thermography may not be enough in order to extract quantitative data about the flowfield, i.e., a time sequence is required. This method was also applied to the mapping of surface temperatures downstream a rearward facing step with very good results. The temperature profile correctly showed the lowest heat transfer rate to occur just after the step and the highest rate at the location of the

turbulent boundary layer reattachment. Thereafter, the influence of the redevelopment of the turbulent boundary layer could be observed too.

These experiments suggest that the infrared imaging system may serve as an experimental tool for validation of CFD codes since the predicted temperature distribution may be corrected for the directional emittance effects of the radiation. As a result, the calculated surface temperature distribution as assumed to be produced by the IR imaging camera may be directly compared with the results of an actual thermography resulting from an experiment run under identical conditions. Generally, it is easier to run first the experiment and then to run the codes, since a precise tuning of the experimental condition may be sometimes an impossible task.

The concept of detecting low speed boundary layer transition over airfoils using IR imaging systems is about five years old. The present research extended the range of application to turbulent separation and laminar complete separation as well. It was shown to be possible to detect the various boundary layer regimes, i.e., laminar, transition bubble, turbulent and separated flow, all on one thermography imaging a NACA 0012 airfoil at 6 degrees angle of attack in ground effect at a chord Reynolds number of 375000. The development of tufts that can be "seen" with the IR imaging camera greatly enhances the capability of this tool in aerodynamic research, because the method serves simultaneously in the temperature measurment and the visualization roles. Based on the observation of the tufts behavior, it was seen that the flow separation and reattachment are phenomena that develop in time. The flow prior to both of them is highly unstable and unsteady, a phenomenon commonly known as buffeting. With regard to the mechanism of

the total flow separation, also known as leading edge laminar bubble burst, it was observed that rather than dealing with a failure of the turbulent boundary layer to reattach, there is a pulsating behavior of the turbulent separated boundary layer flow back and forth chordwise, that tries to "peel-off" the remaining portion of the attached flow from the airfoil surface.

Finally, the reader is reminded that the infrared imaging camera is basically a device sensitive to the number of photons originating from the instantaneous field of view which reach the detector. It is through this mechanism that the IR imaging camera output is sensitive to the surface temperature. Therefore, in extracting quantitative data from the thermographies it is important to remember the factors that may influence the readings, namely emittance values and reflections, directional emittance effects, depth of field and proper focusing etc.

7.2 The Original Contributions of this Research

The heated wire concept is a completely new experimental technique and takes advantage of the IR imaging camera capability to measure the temperature distribution over large areas with no physical contact with the surface investigated, in this case the heated wire. A significant finding enabled the measurement error to be represented as a function of the temperature gradient, and provided a method of correction for the experimental results in order to get the actual temperature distribution. The surface thermography was shown to be a very suitable tool for the determination of thermal boundary layer development, and for the study of separated flows following a backward facing step. The detection of boundary layer flows over airfoils was expanded to the

study of separated flows. The development of tufts "visible" with the IR imaging camera as well as by standard optical means provided a new method of validating some of the findings of the surface thermography.

7.3 Recommendations for Future Work

Since most of the work performed during this program was new in its nature, it is felt that each one of the various experiments reported herein should be revisited, concentrating on one at a time, stressing the depth rather than the span of the research.

The heated wire technique can be applied to virtually any kind of subsonic flow of interest. Boundary layers (laminar or turbulent), confined flows, free shear layers, wakes, jets etc. can be studied using this method. Of course, the first item to consider is the temperature gradient induced error. The precise behavior of this function is required before starting any new experiment. It should also be remembered that each calibration is valid only for the specific conditions under which it was performed. One question to be answered is whether there is a possibility to produce one universal curve that will show the measurement error as a function of the temperature change per instantaneous field of view rather than per unit length at the target. For a resolved target, this task may be easy to accomplish, and with some effort it may even be possible to determine a correction factor that will account for various degrees of unresolved targets. One method to check this possibility is to map the same target with various IR imaging camera objectives, thus changing both the field of view and its ratio to the instantaneous field of view. Referring to the heated wire experiments, it may be useful to know that the infrared imaging camera

may be transformed to a one-dimensional scanning device by stopping the rotation of one of its scanning prisms. By stopping the horizontal prism for example, it is possible to get a scanning rate of 2500 Hz of a certain line, and this raises the possibility of making frequency response experiments using the heated wire technique.

One of the more serious problems with the inverse approach of deducing flow velocities from temperature measurements is that the heat transfer rate is greatly influenced by the free stream turbulence level (Schlichting, 1968, p. 299). Thus, it is possible to use a Nusselt number correlation based on the wire diameter and deduce results based on the assumption that the flow is laminar, while in reality the flow is turbulent and behaving differently with respect to the heat transfer mode. One of the problems with the laminar flow jet experiment was that at a diameter based pipe Reynolds number of about 1000, the flow starts its transition to turbulence, but fully accomplishes it only at a Reynolds number of about 3000 (Blevin, 1984, p. 231). Therefore, a change in the flow velocity, could produce different results not only because the velocity was changed, but also because the level of the turbulence was changed.

In general, it is felt that this method is very suitable for heat transfer research, such as the influence of the freestream turbulence level, or to study the process at low Reynolds or Grashof numbers.

With regard to using surface thermography for boundary layer research, it is very important to have agreement between the expected surface thermal response and the phenomenon investigated. A variety of possibilities are available including thin skin or solid models, that

can be either cooled or heated prior to, or during the whole duration of the experiment in order to follow the development of the thermal boundary layer.

The boundary layer regime detection experiments should really concentrate on the separation signature. The infrared "visible" tufts method should be qualified also on flight tests, although some trouble can be expected in the air because the tufts will be unresolved by the camera. This fact, combined with their low emittance may cause the tufts to become "invisible" to the IR imaging camera during flight tests. Regarding the flight tests, it should be emphasized that the ultimate goal in developing this experimental tool is that by scanning an airplane wing in flight, the test engineer will be able to determine the nature of boundary layer behavior at a specific station i.e., laminar, turbulent or separated. This is the essence and the success criterion for the use of infrared imaging systems in aeronautical engineering.

7.4 Conclusions

The purpose of this study was to explore new applications in which infrared imaging systems could contribute to and enhance aerodynamic research. Two different experimental approaches have been studied: the heated wire technique and the surface thermography. The heated wire technique is a completely new approach to the study of flows with position dependent velocities such as jets, boundary layers, shear flows, wakes etc. The use of surface thermography was extended to research on boundary layer flow detection spanning all the various flow regimes; laminar, transitional, turbulent and separated. In order to

confirm the thermographic results, a visualization method was developed using tufts detectable by the IR imaging camera, thus making this system a simultaneous, temperature measurement as well as a flow visualization tool.

REFERENCES

AGA Thermovision® 782 Operating Manual, 1984.

Anon, "Infrared Imaging System Will Record Flow Fields During Shuttle Reentry," Aviation Week and Space Technology, December 7, 1987, p. 65.

ASHRAE Handbook of Fundmentals, 1972, American Society of Heating, Refrigerating and Air-Conditioning Engineers.

ASME: Fluid Meters, Their Theory and Application, ASME, 1971 (6th Edition).

Balageas, D. L. and Ory, D., "Improvements in the Determination of Convective Transfer From Infrared Thermography," La Recherche Aerospatiale, No. 1980-3, May-June 1980, pp. 73-79.

Bird, R. B., Stewart, W. E. and Lightfoot, E. N., Transport Phenomena, John Wiley, 1960.

Blevins, R. D., Applied Fluid Dynamics Handbook, Van Nostrand, 1984.

Bouchardy, A-M., Durand, G. and Gauffre, G.," Processing of Infrared Thermal Images for Aerodynamic Research," Applications of Digital Image Processing, April 19-22, 1983, Geneva, Switzerland, SPIE, Vol. 397.

Boyland, D. E., Carver, D. B., Stallings, D. W. and Trimmer, L. L., "Measurement and Mapping of Aerodynamic Heating Using a Remote Infrared Scanning Camera in Continuous Flow Wind Tunnels," Proceedings of the AIAA 10th Aerodynamics Testing Conference, San Diego, California, April 19-21, 1978, pp. 213-231.

Brandon, J. M., Manuel, G. S. Wright, R. E. and Holmes, B. J., "In-flight Flow Visualization Using Infrared Imaging," AIAA 4th Flight Test Conference, May 18-20, 1988, San Diego, California, AIAA Paper No. 88-2111.

Brendel, M. and Mueller, T. J., "Boundary Layer Measurements on an Airfoil a Low Reynolds Numbers," AIAA Journal, Vol. 25, No. 7, July 1988, pp. 612-617.

Burmeister, L. C., Convective Heat Transfer, John Wiley, 1983.

Bynum, D. S., Hube, F. K., Key, C. M. and Dyer, P. M., "Measurement and Mapping of Aerodynamic Heating in VKF Tunnel B with Infrared Camera," AEDC TR-76-59, November 1976.

Carlomagno, G. M. and De Luca, L., "Heat Transfer Measurements by Means of Thermography," Proceedings of the 4th Flow Visualization Congress, Paris, August 1986, pp. 611-616.

Carr, L. W., McAlister, K. W. and McCroskey, W. J., "Analysis of the Development of Dynamic Stall Based on Oscillating Airfoil Experiments," NASA TN D-8382, January 1977.

Carter, L. D., "Supersonic Boundary-Layer Transition Detection Using Thermographic Phosphorescent Paint," M.S. Thesis, University of Tennessee, March 1975.

Champagne, F. H., Sleicher, C. A. and Wehrman, O. H., "Turbulence Measurements with Inclined Hot Wires," J. Fluid Mechanics (1967), Vol. 28, Part I, pp. 153-175.

Chocol, C. J., "Remote Infrared Imagery of Shuttle During Entry," Proceedings of the Joint Automatic Control Conference, Denver, Colorado, June 17-21, 1979, (AICE), pp. 251-255.

Compton, D. L., "Convective Heating Measurement by Means of an Infrared Camera," NASA TM X-2507, February 1972.

Compton, D. L., "Use of an Infrared-Imaging Camera to Obtain Convective Heating Distributions," AIAA Journal, Vol. 10, No. 8, 1972, pp. 1130-1132.

Eaton, J. K. and Johnston, J. P., A Review of Research on Subsonic Turbulent Flow Reattachment, AIAA Journal, Vol. 19, No. 9, Sept. 1981, pp. 1093-1100.

Eckert, E. R. G. and Drake, R. M., Jr., Analysis of Heat and Mass Transfer, McGraw-Hill, 1972 (Second Edition).

Eppler, R. and Sommers, D. M., "A Computer Program for the Design and Analysis of Low-Speed Airfoils," NASA TM 80210, August 1980; also see supplement to, NASA TM 81862, December 1980.

Fand, R. M., Morris, E. W. and Lou, M., "Natural Convection Heat Transfer from Horizontal Cylinders to Air, Water and Silicone Oils for Rayleigh Numbers Between $3x10^2$ and $2x10^7$," Int. J. Heat Mass Transfer, (1977) Vol. 20, pp. 1173-1184.

Flaig, J. W., "Infrared Flow Visualization for VTOL Applications," AIAA/NASA Ames V/STOL Conference, Palo Alto, California, June 6-8, 1977, pp. 314-321, AIAA Paper No. 77-618.

Gartenberg, E. and Roberts, A. S., Jr., "Phenomenological Aspects of Infrared Imaging in Aeronautical Research," AIAA/NASA/AFWAL Conference on Sensors and Measurements Techniques for Aeronautical Applications, September 7-9, 1988, Atlanta, Georgia, U.S.A, AIAA Paper No. 88-4674.

Gartenberg, E. Roberts, A. S. Jr. and Selby, G. V., "Infrared Surface Imaging as a Flowfield Diagnostic Tool," Proceedings of the 12th International Congress on Instrumentation in Aerospace Simulation Facilities (ICIASF 87), June 22-25, 1987, Williamsburg, Virginia, pp. 393-349.

Green, M. J. Budnik, M. L. Young, L. and Chiasson, M. P., "Supporting Flight-Data Analysis for Space Shuttle Orbiter Experiments at NASA Ames Research Center," NASA TM 89395, April 1983.

Hansman, R. J., Jr. and Craig, A. P., "Low Reynolds Number Tests of NACA 64-210, NACA 0012 and Wortman FX67-K170 Airfoils in Rain," J. of Aircraft, Vol. 24, No. 8, August 1987, pp. 559-566.

Hender, D. R. and Okabe, C. M., "Expanded Uses of Infrared Scanning Data in Aerodynamic Heating Materials Tests," AIAA 18th, Thermophysics Conference, June 1-3, 1983, Montreal, Canada, AIAA Paper No. 83-1542.

Hsieh, C. K. and Ellingson, W. A., "A Quantitative Determination of Surface Temperatures Using an Infrared Camera," Modern Utilization of Infrared Technology III, SPIE Vol. 124 (1977) pp. 228-235.

Jones, R. A. and Hunt, J. L., "Use of Fusible Temperature Indicators for Obtaining Quantitative Aerodynamic Heat-Transfer Data," NASA TR R-230, February 1966.

Kays, W. M. and Crawford, M. E., Convective Heat and Mass Transfer, McGraw-Hill, 1980 (Second Edition).

Klein, J. and Tribus, M., "Forced Convection from Non-Isothermal Surfaces," University of Michigan Research Institute, August 1952, Project M 992-B.

Ladson, C. L., "Effects of Independent Variation of Mach and Reynolds Numbers on the Low-Speed Aerodynamic Characteristics of the NACA 0012 Airfoil Section," NASA Technical Memorandum 4078, October 1988.

Levinstein, H., "State of the Art of Infrared Detectors," Modern Utilization of Infrared Technology III, SPIE, Vol. 129, 1977, pp. 52-56.

Lloyd, J. M., Thermal Imaging Systems, Plenum Press, 1975.

Martinez, A., Dye, W. H., Vaughn, J. E., Hersey, D. W. and Lutz, G. R., "Results of Test 0H69 Obtained in the AEDC VKF Hypersonic Tunnel B Using the Infrared Scanning Method to Obtain Heat Transfer Data on the 0.040 Scale Model 82-0 of the Space Shuttle Forebody," Vols. I and II, NASA-CR-151410 and NASA-CR-151411, July 1978.

McAdams, W., Heat Transmission, 3rd. Edition, McGraw-Hill, 1954.

McCroskey, J. W., "A Critical Assessment of Wind Tunnel Results for the NACA 0012 Airfoil," NASA TM 100013, October 1987.

McCullough, G. B. and Gault, D. E., "Examples of Three Representative Types of Airfoil-Section Stall at Low Speed," NACA TN 2502, September 1951.

Meroney, R. N., "Studying the Convective Heat Transfer from a Building Model with Infrared Camera Techniques," ASME Transactions 78-WA/HI-58.

Merzkirch, W., Page, R. H. and Fletcher, L.S., "A Survey of Heat Transfer in Compressible Separated and Reattached Flows," AIAA Journal, Vol. 26, No. 2, February 1988, pp. 144-150.

Mordoff, K., H., "German Researchers Seek to Improve Prediction of Laminar Flow Changes," Aviation Week and Space Technology, January 18, 1988, pp. 40-41.

Morgan, V. T., "The Overall Convective Heat Transfer from Smooth Circular Cylinders," Advances in Heat Transfer, Vol. 11, Academic Press, 1975.

Myrick, D. L. and Kantsios, A. G., "Incorporating Geometric and Radiative Effects into Infrared Scanning Computer Analysis," SPIE, Vol. 371, Thermosense V, 1982, pp. 211-215.

Myrick, D. L. and Throckmorton, D. A., "Comprehensive Analysis of Shuttle Orbiter Leeside Surface Infrared Imagery Obtained During Atmospheric Entry," International Conference on Thermal Infrared Sensing for Diagnostics and Control, Thermosense VII, SPIE, Vol. 581, Cambridge, Massachussets, September 12-20, 1985, pp. 116-121.

Nutt, K. W., "Space Shuttle Orbiter SILTS Pod Flow Angularity and Aerodynamic Heating Tests," AEDC TSR-79-V70, November 1979.

Ohman, C., "Measurement Versus Imaging in Thermography or What is Resolution," to be obtained from the author at AGEMA Infrared Systems AB, Development Department, Box 3, S-182 11 Danderyd, Sweden, or Eklund Infrared, 142 Sunset Avenue, Verona, NJ 07044.

Page, R. H., Ostowari, C. and Carbone, J. S., "Radial Jet Flow," Proceeding of the 4th Flow Visualization Congress, Paris, August 1986, pp. 513-521.

Quast, A., "Detection of Transition by Infrared Image Technique," Proceedings of the 12th International Congress on Instrumentation in Aerospace Simulation Facilities (ICIASF 87), Williamsburg, Virginia, June 22-25, 1987, pp. 125-139.

Sasaki, M., Takahara, K., Kumagai, T. and Hamano, M., "Film Cooling Effectiveness for Injection from Multirow Holes," Journal of Engineering for Power, January 1979, Vol. 101, pp. 101-108.

Schlichting, H., Boundary Layer Theory, McGraw-Hill, 1968.

Schmitt, R. L. and Chanetz, B., P., "Experimental Investigation of Three Dimensional Separation on an Ellipsoid-Cylinder Body at Incidence," AIAA 18th Fluid Dynamics and Plasmadynamics and Lasers Conference, July 16-18, 1985, Cincinnati, Ohio, AIAA-85-1686.

Seraudie, A., Blanchard, A. et. Dor, J. B., "Qualification d' Essais en Ambiance Cryogenique a la Soufflerie T2," 23eme Colloque d'Aerodynamique Appliquee, Modane, November 12-14, 1988. Association Aeronautique et Astronautique de France, Note Technique No. 86-07.

Sparrow, E. M. and Cess, R. D., Radiation Heat Transfer, Hemisphere (McGraw-Hill), 1978.

Spence, T. M., "Applications of Infrared Thermography in Convective Heat Transfer," M.S. Thesis, Naval Postgraduate School, Monterey, California, March 1986.

Stallings, D. W. and Carver, D. B., "Infrared and Phase-Change Paint Measurements of Heat Transfer on the Space Shuttle Orbiter," AEDC-TSR-78-V13, June 1978.

Stallings, D. W., Mathews, R. K. and Jenke, L. M., "Recent Developments in Aerothermodynamic Test Techniques at the AEDC von Karman Gas Dynamics Facility," International Congress on Instrumentation in Aerospace Facilities 8th (ICIASF79), Monterey, California, September 24-26, 1973, pp. 1-10.

Stallings, D. W. and Whetsel, R. G., "Use of Infrared Imagery in Continous Flow Wind Tunnels," Thermal Infrared Sensing Diagnostics (Thermosense V), Detroit, Michigan, October 25-27, 1982, SPIE, Vol. 371, pp. 203-210.

Swenson, B. 1. and Edsinger, L. E., "Preliminary Analysis of Remote Infrared Imagery of Shuttle During Entry - An Aerothermodynamic Flight Experiment," NASA TM 73251, August 1977.

Thermosense V, (Proceedings of) SPIE, Vol. 371, 1982.

Thomann, H. and Frisk, B., "Measurement of Heat Transfer with an Infrared Camera," Int. J. Heat Mass Transfer, Vol. 11, Pergamon Press, 1968, pp. 819-826.

Throckmorton, D. A., "Heat Transfer Procedures in Phase B Shuttle Studies with Emphasis on Phase-Change Data Improvement," NASA TM X-2507, February 1972.

Throckmorton, D. A., Zoby, E. V. and Kantsios, A. G., "The Shuttle Infrared Leeside Temperature Sensing (SILTS) Experiment," AIAA 23rd Aerospace Sciences Meeting, January 14-17, 1985, Reno, Nevada, AIAA-85-0328.

Thwaites, B. (editor), Incompressible Aerodynamics, Dover, 1987.

APPENDICES

Appendix A

APPENDIX TO CHAPTER 4: THE LAMINAR FLOW JET EXPERIMENT

A1: Error Calculations

These calculations ignore the errors that may originate in the camera's difficulty to track high temperature gradients.

1. Wire temperature read-outs from Disco II.®

   (a) Due to uncertainty of the ambient temperature

   $\Delta T_a = 0.05^0C \quad \Delta T_w = 0.9^0C$

   (b) Due to emittance input accuracy (through the transmittance factor in Disco II). The transmittance last significant digit is 1%. A transmittance difference of 0.5% implies a $\Delta T_w = 0.2^0C$

   (c) Due to temperature induced changes in the surface emittance - unknown in nature

   (d) Due to improper focusings - practically zero.

   (e) Due to the AGA infrared camera accuracy $\Delta T_w = 0.2^0C$

   Therefore:

$$\Delta T_w = \sqrt{0.9^2 + 0.2^2 + 0.2^2} = 0.9^0C$$

2. Mean jet velocity assumed at a certain point (pixel)

   (a) Due to uncertainty in total pressure and temperature measurements ahead of the sonic nozzle:

   $\Delta u = 0.09$ m/sec.

   Note: The total temperature induced error is 2 orders of magnitudes lower than that induced by the pressure error. The pressure error has three contributions:

   i) reading accuracy ± 1 psig

   ii) pressure fluctuations ± 1 psig

   iii) Gage accuracy assumed a 3% i.e., ± 0.9 psig.

   Altogether this accounts for ± 1.68 psig.

   (b) Due to uncertainty in the nozzle's discharge coefficient 1%:

   $\Delta u = 0.02$ m/sec

   (c) Due to the camera's resolution (translates into half a pixel on the computer's screen)

   $\Delta u = 0.36$ m/sec

   Therefore:

   $$\Delta u = \sqrt{(0.09)^2 + (0.02)^2 + (0.36)^2} = 0.37 \text{ m/sec}$$

3. (a) Error in the calculated temperature profile due to velocity uncertainities: ±1% from the absolute temperature in deg K.

   (b) Error in deduced velocity from temperature measurements: ±15% from the local velocity.

The error in the calculated temperature was estimated with data from experiment #3 with Δu = 0.37 m/sec. The error in the deduced velocity was estimated in the same way with ΔT_w = 0.9K.

4. The relatively high errors encountered in this experiment should be credited in their greatest part to the purpose of the experiment, that was to evaluate to what extent the IR imaging system can detect relatively high temperature changes that occur over a small portion of the camera field of view. When viewed in this light, the system's performance is quite satisfactory. This fact can be better understood by reconsidering the magnitude of the error induced by the uncertainty in determining the exact location of the measured spot (the "half pixel" uncertainty, see item above). If, for example, the jet would have been mapped along the whole width of the field of view of the IR imaging camera, this error could be reduced by an order of magnitude. This of course, would require a different objective lens.

5. The error in determining the velocity distribution in the core flow of the jet varied between 2.8% on the centerline and 12.5% near the wall. According to the manufcturer's specifications, the Pitot static tube may induce an error of ±2%. The rest of the error originates in the accuracy of reading of the difference between the water columns in the U-shaped manometer (±0.5 mm).

A2: Miscellaneous Calculations

(1) Radiation losses estimation:

$\alpha = \varepsilon = 0.05$

$E = \varepsilon\sigma(T_w^4 - T_a^4)A = 0.05 \times 5.668 \times 10^{-8} (373^4 - 293^4) \cdot \pi \cdot 7.62 \times 10^{-5} \times 1.0$

$= 0.008$ w/m length of wire.

(2) Conduction losses estimation (per pixel distance) for

$\dot{q}_{elec} = 9.33$ w/m (maximum heating rate):

1 pixel at 0.5 m focus = 1.154 mm.

$$\dot{Q} = - kA[\text{grad } T_{x_2} - \text{grad } T_{x_1}] \cdot \frac{1}{\Delta x_{1-2}}$$

$$T(^0C) = 78.1 - 10.2 \cos[\frac{x(mm)}{12.694} \pi]; \qquad (r^2 = 98.3\%; \quad \sigma = 1K)$$

$$\text{grad } T = 10.2 \left(\frac{\pi}{12.694 \times 10^{-3}}\right) \sin[\frac{x(mm)}{12.694} \pi] \text{ (K/m)}$$

$$\dot{\Delta Q}_{\substack{\text{conduction} \\ \text{max}}} = 50 \cdot \frac{\pi}{4} [7.62 \times 10^{-5}]^2 \times 10.2 \frac{\pi}{12.694 \times 10^{-3}} [0.989 - 0.910] \frac{1}{1.154 \times 10^{-3}}$$

$= 3.97 \times 10^{-2}$ w/m length of wire

(3) The free convection estimations were based on Kays and Crawford (1980) p. 328:

$$Nu = 0.518 \left[1 - \left(\frac{0.599}{Pr}\right)^{0.6}\right]^{-5/12} (Gr_D \, Pr)^{1/4} \qquad (A.1)$$

with the correction for thick boundary layer compared to the cylinder diameter

$$\bar{Nu} = \frac{2}{\ln (1 + 2/Nu)} \qquad (A.2)$$

The transcendental Eqs. for ΔT assuming $\overline{T_f}$ = 323K is

$$\Delta T = 887\ i^2 \ln \left[1 + \frac{2}{0.029(\Delta T)^{0.25}}\right] \qquad (A.3)$$

where i the electrical current in Amperes.

(4) The coefficient of determination r^2 (adjusted for degrees of freedom) is given by:

$$r^2 = 1 - \frac{\text{Sum of squares of the residuals } /(n-p)}{\text{Sum of squares of the total values } /(n-1)} \qquad (A.4)$$

where n is the degrees of freedom and p is the number of the coefficients fit in the regression equation.

(5) Calculation of the predicted wire temperatures in Figs. 4.6 and 4.7 and of the deduced velocity profiles in Figs. 4.10, 4.11 and 4.12.

The correlation (Eq. 4.1)

$$Nu = 0.795\ Re^{0.384} \qquad (A.5)$$

can be explicitly written

$$\frac{h\ d}{k_a} = 0.795 \left(\frac{U\ d}{\nu_a}\right)^{0.384} \qquad (A.6)$$

where h is the heat transfer coefficient, d is the wire diameter, k_a is the conductivity of the air, U is the local velocity of the air and ν_a is the kinematic viscosity of the air.

Defining $\Delta T = T_{wire} - T_{air}$

and

$$h = \frac{\dot{q}}{A\Delta T}$$

where $\dot{q}$ is the heat generated per unit length of wire ($\dot{q} = i^2R$) and A is the circumferential area of the wire per unit length ($A = \pi d$), one gets

$$\Delta T = \frac{\dot{q}}{0.795\pi\, k_a} \left(\frac{\nu_a}{d}\right)^{0.384} U^{-0.384} \qquad (A.7)$$

This formula was used as is to deduce air velocities from the wire temperature measurements (Figs. 4.10-4.12). To predict the wire temperatures in Figs. 4.6 and 4.7, the velocity profile was assumed to have a parabolic distribution:

$$U(r) = U_{max}\left[1-\left(\frac{r}{R}\right)^2\right] \qquad (A.8)$$

where U_{max} is the centerline velocity of the air in the pipe and has twice the value of the mean velocity.

A3: Approximating Functions for the Temperature Distributions

Assuming a cosine function approximation for the temperature variation along the wire, with the maximum temperatures occurring at $X = 0, \ell$ (0 and 2π radians respectively), and the minimum at $X = \ell/2$ ($\pi/2$ radians), the temperature profile can be approximated by:

$$T(x) = 0.5\left[(T_{max} + T_{min}) + (T_{max} - T_{min})\cos\frac{2\pi x}{\ell}\right] \qquad (A.9)$$

In Figs. 4.6 and 4.7, zero radians correspond to pixel #-11, π radians to pixel #0, and 2π radians to pixel #11. Therefore

$$\text{grad } T(x) = -(T_{max} - T_{min}) \frac{\pi}{\ell} \sin \frac{2\pi x}{\ell} \qquad (A.10)$$

The evaluation for the four experiments is given in Table A.1 below.

Table A.1 Approximating functions for the wire temperature distribution and temperature gradient

Experiment #	$\dot{q}$ w/m	T(X) °C	grad T(X) K/m
1	3.47	$43.6 + 4.6 \cos \frac{2\pi x}{\ell}$	$- 1138.4 \sin \frac{2\pi x}{\ell}$
2	4.71	$53.4 + 5.3 \cos \frac{2\pi x}{\ell}$	$- 1311.7 \sin \frac{2\pi x}{\ell}$
3	6.17	$61.7 + 7.7 \cos \frac{2\pi x}{\ell}$	$- 1905.6 \sin \frac{2\pi x}{\ell}$
4	9.33	$77.7 + 9.5 \cos \frac{2\pi x}{\ell}$	$- 2351.1 \sin \frac{2\pi x}{\ell}$

$\ell = 0.0254$ m
$\Delta x = 0.001154$ m (1 pixel)

Appendix B

APPENDIX TO CHAPTER 5: THE FLAT PLATE EXPERIMENT

B1: Error Calculations

1.1 Surface temperature read-outs from Disco II (software package for IR data reduction)

(a) Due to uncertainty of the ambient temperature, practically zero ($\Delta T_\infty << \Delta T_w$).

(b) Due to uncertainty of emittance value.

$$\Delta\varepsilon = 0.02 \qquad \Delta T_w = 0.6^0C$$

(c) Due to temperature induced changes in the surface emittance - unknown in nature.

(d) Due to unproper focusing - practically zero.

(e) Due to the AGA camera resolution

$$\Delta T_w = 0.2^0C$$

(f) Due to error in location

$$\Delta T_w = 0.15^0C$$

Therefore,

$$\Delta T_w = \sqrt{0.6^2 + 0.2^2 + 0.15^2} = 0.65^0C$$

1.2 Error of the slope of θ vs $x^{1/2}$ (mean value)

$$\Delta \frac{d\theta}{d(x^{1/2})} = \frac{2x\ 0.65}{0.4 - 0.2} = 6.5\ \frac{^0C}{m^{1/2}}$$

1.3 Error of velocity measurement

Estimated at 2%

$$\Delta U = 21 \times 0.02 = 0.42\ m/sec$$

1.4 Error in the (calculated) convected heat flux (worst case);

$$\dot{q}''_o = \frac{d\theta}{d(x^{1/2})} \frac{k\ Pr^{1/3}\ U^{1/2}}{2.2019\ \nu^{1/2}}$$

$$\Delta \dot{q}''_o = \frac{k\ Pr^{1/3}}{2.2019\ \nu^{1/2}} \{U^{1/2} \cdot \Delta \left(\frac{d\theta}{d(x^{1/2})}\right) + \frac{d\theta}{d(x^{1/2})} \frac{1}{2\ U^{1/2}} \Delta U\}$$

$$= \frac{0.02709 \cdot 0.709^{1/3}}{2.2019 \cdot (16.95 \times 10^{-6})^{1/2}} (20.9^{1/2} \cdot 6.5 + \frac{50.07}{2 \cdot 20.9^{1/2}} \cdot 0.42)$$

$$= 2.66\ (29.72 + 2.3) = 85.2\ \frac{W}{m^2}$$

This is about one fifth of the mean convected heat-flux value and it comes almost entirely from the error in temperature measurements, which originate in the uncertainty of the emittance value (see items 1.1 and 1.2 above). This is a well known difficulty and is discussed in Sparrow and Cess (1978).

B2: Miscellaneous Calculations

1. Determination of the temperature distribution along a flat plate in the laminar boundary layer regime with constant heat flux, equation (5.1).

Starting from equation (9-39) in Kays and Crawford (1980)

$$T_o(x) - T_\infty = \frac{0.623}{k} Pr^{-1/3} Re^{-1/2} \int_o^x \left[1 - \left(\frac{\xi}{x}\right)^{3/4}\right]^{-2/3} \dot{q}_o''(\xi)\, d\xi \qquad (B.1)$$

for $\dot{q}_o''(\xi) = \text{const}$, and with $y = \frac{\xi}{x}$; $dy = \frac{1}{x} d\xi$ the integral becomes

$$x \int_o^1 (1 - y^{3/4})^{-2/3} dy \qquad (B.2)$$

Now $z = y^{3/4}$ and $dz = \frac{3}{4} y^{-1/4} dy \rightarrow dy = \frac{4}{3} dz\, (y^{1/4})$ and the integral becomes

$$x \int_o^1 (1 - z)^{-2/3} \cdot \frac{4}{3} z^{1/3} dz \qquad (B.3)$$

Since $\beta_1 (m,n) = \int_o^1 z^{m-1}(1-z)^{n-1} dz = \beta_1(m,n) = \frac{\Gamma(m) \cdot \Gamma(n)}{\Gamma(m+n)}$, we get for the integral

$$\frac{4x}{3} \int_o^1 (1 - z)^{\frac{1}{3}-1} z^{1\frac{1}{3}-1} dz \qquad n = \frac{1}{3} \qquad m = 1\frac{1}{3} \qquad (B.4)$$

Since $\Gamma(n + 1) = n\, \Gamma(n) \rightarrow \Gamma(\frac{1}{3}) = 3\Gamma\,(1\frac{1}{3})$, we get

$$\frac{4x}{3} \frac{3\Gamma(1\frac{1}{3})\, \Gamma(1\frac{1}{3})}{\Gamma\,(1\frac{2}{3})} = \frac{4x}{3} \frac{3[\Gamma(1\frac{1}{3})]^2}{\Gamma(1\frac{2}{3})} = \frac{4x}{3} \frac{3(0.89338)^2}{0.90330} = 3.5343X \qquad (B.5)$$

Inserting this value for the integral in (B.1) and defining $\Theta(x) = T_o(x) - T_\infty$ one gets

$$\Theta(x) = 2.2019 \frac{\dot{q}''_o}{k} \times Pr^{-1/3} Re^{-1/2} \qquad (B.6)$$

which is precisely equation (5.1).

2. Calculation of the velocity boundary layer thickness.

Following Schlichting, (1968) p. 26, the laminar velocity boundary layer thickness can be well approximated by

$$\delta = 5\ Re_x^{-1/2}\ x \text{ or}$$

$$\delta = 5\left(\frac{\nu}{u}\right)^{1/2} x^{1/2}$$

The numerical value for this experiment was calculated according to

$$\delta(m) = 0.004375\ [x(m)]^{1/2} \qquad (B.7)$$

B3: Description of the Computer Program for the Flat Plate Experiment

Figure B.1 shows the mesh discretization of the flat plate and indicates the individual elements or groups of elements for which specific algorithm formulae were derived.

1. Leading Edge (constant temperature assumption):

$$T_{0,0}^{p+1} = T_{0,0}^{p} + 4\ A\ k_w \frac{tg\alpha}{\Delta x}\left(T_{1,0}^{p} - T_{0,0}^{p}\right) + 3.756\ A\ k_a\ Pr^{1/3}\left[\left(\frac{U}{\Delta x \nu}\right) \cdot \right.$$

$$\left. \cdot \left(1 + \frac{1}{\cos\alpha}\right)\right]^{1/2} \left(T_a - T_{0,0}^{p}\right) + 8A\varepsilon\sigma\left(1 + \frac{1}{\cos\alpha}\right)\left(T_a^4 - T_{o,o}^{p\,4}\right)$$

$$+ \dot{q}''_o\left(1 + \frac{1}{\cos\alpha}\right) 4A \qquad (B.8)$$

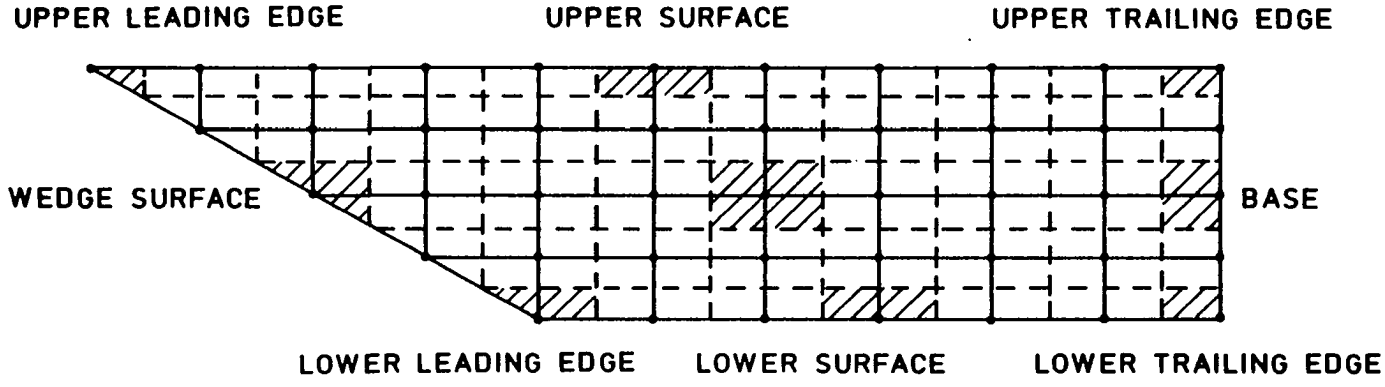

Fig. B.1 Mesh discretization and typical cells used for the flat plate model analysis

$$A \equiv \frac{\Delta\tau}{\rho_w c_w \Delta x \, tg\alpha} \tag{B.9}$$

2. Upper Surface (arbitrarly specified temperature distribution assumption):

$$T^{p+1}_{i,o} = T^{p}_{i,o} + \frac{2 A k_w}{\Delta x \, tg\alpha}(T^{p}_{i,1} - T^{p}_{i,o}) + \frac{A k_w tg\alpha}{\Delta x}(T^{p}_{i-1,o} + T^{p}_{i+1,o} - 2T^{p}_{i,o}) + A \sum_{\ell=1}^{i} \{0.664 k_a Pr^{1/3} (\frac{U}{\nu i \Delta x})^{1/2}[1 - (\frac{\ell-\frac{1}{2}}{i})^{3/4}]^{-1/3} \cdot (T_{\ell-1,o} - T^{p}_{\ell,o})\} + 0.664 A k_a Pr^{1/3} (\frac{U}{\nu i \Delta x})^{1/2} (T_a - T^{p}_{o,o}) + 2 A \varepsilon \sigma (T^4_a - T^{p\,4}_{i,o}) + 2 A \dot{q}''_o \tag{B.10}$$

3. Upper Trailing Edge (constant temperature assumption with correction factor):

$$T^{p+1}_{i,o} = T^{p}_{i,o} + \frac{2 A k_w}{tg\alpha \, \Delta x}(T^{p}_{i,1} - T^{p}_{i,o}) + \frac{2 A k_w tg\alpha}{\Delta x}(T^{p}_{i-1,o} - T^{p}_{i,o}) + 0.664A C_{corn}(1 + tg\alpha) k_a Pr^{1/3}(\frac{U}{\nu x})^{1/2} (T_a - T^{p}_{i,o}) + 2 A \varepsilon \sigma (1 + tg\alpha)(T^4_a - T^{p\,4}_{i,o}) + 2 A \dot{q}''_o (1 + tg\alpha) \tag{B.11}$$

4. Wedge Surface (power function freestream velocity and wall temperature variation, see Burmeister 1983, pp. 308-309):

$$T^{p+1}_{i,j} = T^{p}_{i,j} + \frac{2 A k_w tg\alpha}{\Delta x}(T^{p}_{i+1,j} - T^{p}_{i,j}) + \frac{2 A k_w}{tg\alpha \, \Delta x}(T^{p}_{i,j-1} - T^{p}_{i,j}) + \frac{2 A B P_r^{\lambda} k_a}{\cos\alpha}(\frac{C_{flo} U}{\nu})^{1/2} (\frac{j \Delta x}{\cos\alpha})^{\frac{P-1}{2}} (T_a - T^{p}_{i,j}) + \frac{2 A \varepsilon \sigma}{\cos\alpha}(T_a - T^{p\,4}_{i,j}) + \frac{\dot{q}''_o \cdot 2 A}{\cos\alpha} \tag{B.12}$$

For $\alpha = 30°$ $\lambda = 0.3445$ $C_{flo} = 2.0$

Assuming constant heat flux B = 0.4782

5. Interior Points (pure conduction assumption):

$$T^{p+1}_{i,j} = T^{p}_{i,j} + \frac{\alpha_w \Delta\tau}{(\Delta x)^2}\left(T^{p}_{i+1,j} + T^{p}_{i-1,j} - 2T^{p}_{i,j}\right) +$$

$$+ \frac{\alpha_w \Delta\tau}{(\Delta y)^2}\left(T^{p}_{i,j+1} + T^{p}_{i,j-1} - 2T^{p}_{i,j}\right) \qquad (B.13)$$

$$\Delta y \equiv \Delta x \; tg\alpha \qquad (B.14)$$

6. Base (identical with upper trailing edge):

$$T^{p+1}_{i,j} = T^{p}_{i,j} + \frac{2\,A\,k_w\,tg\alpha}{\Delta x}\left(T^{p}_{i-1,j} - T^{p}_{i,j}\right) + \frac{k_w A}{\Delta x\; tg\alpha}\left(T^{p}_{i,j-1} +\right.$$

$$\left. + T^{p}_{i,j+1} + 2T^{p}_{i,j}\right) + 0.664\,A\,C_{corn}\,k_a\,Pr^{1/3}\left(\frac{U}{\nu x}\right)^{1/2}\left(T_a - T^{p}_{i,j}\right) +$$

$$+ 2\,\varepsilon\,\sigma\,A\,tg\alpha\left(T_a^4 - T^{p}_{i,j}{}^4\right) + 2\,A\,tg\alpha\,\dot{q}''_o \qquad (B.15)$$

7. Lower Leading Edge (see wedge surface):

$$T^{p+1}_{i,j} = T^{p}_{i,j} + \frac{4\,A\,k_w\,tg\alpha}{3\Delta x}\left(T^{p}_{i+1,j} - T^{p}_{i,j}\right) + \frac{8\,A\,k_w}{3\;tg\alpha\;\Delta x}\left(T^{p}_{i,j-1} - T^{p}_{i,j}\right) +$$

$$+ \frac{4\cdot 0.664\,A}{3}\,k_a\,Pr^{1/3}\left(\frac{2U}{\nu\Delta x}\right)^{1/2}\left(T_a - T^{p}_{i,j}\right) +$$

$$+ \frac{4\,A}{3\,\cos\alpha}\,B\,Pr^{\lambda}\,k_a\left(\frac{C_{flo}\,U}{\nu}\right)^{1/2}\left[\frac{\Delta x}{\cos\alpha}\,(i - 0.25)\right]^{\frac{p-1}{2}}\left(T_a - T^{p}_{i,j}\right) +$$

$$+ \frac{8}{3}\,A\,\varepsilon\,\sigma\left(1 + \frac{1}{2\,\cos\alpha}\right)\left(T_a^4 - T^{p}_{i,j}{}^4\right) + \frac{8}{3}\,A\,\dot{q}''_o\left(1 + \frac{1}{2\,\cos\alpha}\right) \qquad (B.16)$$

8. Lower Surface (see upper surface):

$$T^{p+1}_{i,n} = T^{p}_{i,n} + \frac{2\,A\,k_w}{\Delta x\;tg\alpha}\left(T^{p}_{i,n-1} - T^{p}_{i,n}\right) + \frac{A\,k_w\,tg\alpha}{\Delta x}\left(T^{p}_{i-1,n} + T^{p}_{i+1,n} -\right.$$

$$\left. - T^{p}_{i,n}\right) + A\sum_{\ell=n+1}^{i}\left\{0.664\,k_a\,Pr^{1/3}\left(\frac{U}{\nu(i-n)\Delta x}\right)^{1/2}\cdot\right.$$

$$\cdot \left[1 - \left(\frac{\ell - \frac{1}{2} - n}{i-n}\right)^{3/4} \left(T^p_{\ell-1,n} - T^p_{\ell,n}\right)\right\} +$$

$$+ 0.664\ A\ k_a\ Pr^{1/3} \left(\frac{U}{\nu(i-n)\Delta x}\right)^{1/2} \left(T_a - T^p_{n,n}\right) +$$

$$+ 2\ A\ \varepsilon\ \sigma\ \left(T_a^4 - T_{i,n}^{p\,4}\right) + 2\ A\ \dot{q}''_o \qquad \text{(B.17)}$$

9. Lower Trailing Edge (see upper trailing edge):

$$T^{p+1}_{i,j} = T^p_{i,j} + \frac{2\ A\ k_w}{tg\alpha\ \Delta x}\left(T^p_{i,j-1} - T^p_{i,j}\right) + \frac{2\ A\ k_w\ tg\alpha}{\Delta x}\left(T^p_{i-1,j} - T^p_{i,j}\right) +$$

$$+ 0.664\ A\ C_{corn}\ (1 + tg\alpha)\ k_a\ Pr^{1/3}\ \left(\frac{U}{\nu(x - y/tg\alpha)}\right)^{1/2} \left(T_a - T^p_{i,j}\right) +$$

$$+ 2\ A\ \varepsilon\ \sigma\ (1 + tg\alpha)\ \left(T_a^4 - T^{p\,4}_{i,j}\right) + 2\ A\ \dot{q}''_o\ (1 + tg\alpha) \qquad \text{(B.18)}$$

The time step $\Delta\tau$ was chosen to be one-tenth of what was required by the stability criterion derived for upper surface elements considering conduction and convection modes combined, namely:

$$\Delta\tau = 0.1\ (\Delta y)^2/2\alpha_w(1 + tg^2\alpha + h\ \Delta y/k_w) \qquad \text{(B.19)}$$

with

$$h = 0.332\ k_a\ Pr^{1/3}\left(\frac{U}{\nu\Delta x}\right)^{1/2} \qquad \text{(B.20)}$$

The following numerical values were used for the constants in the program:

length of plate	$x = 0.322$ m
thickness of plate	$y = 0.019$ m
step in y direction	$\Delta y = 0.7326575 \times 10^{-3}$ m
step in x direction	$\Delta x = \Delta y/tg\alpha$
leading edge angle	$\alpha = 30°$

total experiment time	$t = 30$ sec
air kinematic viscosity	$\nu = 16.67 \times 10^{-6}$ m^2/sec
air conductivity	$k_a = 26.87 \times 10^{-3}$ w/mK
air Prandtl number	$Pr = 0.709$
air velocity	$U = 20.92$ m/sec.
air temperature	$T_a = 302K$
surface heat flux	$\dot{q}_o'' = 949$ w/m^2
surface emittance	$\varepsilon = 0.75$
Stefan-Bolzmann constant	$\sigma = 5.6697 \times 10^{-8}$ w/m^2K^4
wood density	$\rho_w = 432.5$ kgm/m^3
wood specific heat	$c_w = 2720$ J/kgmK

For a discussion of the wood properties, see Section 5.5. The computer program was validated through a series of runs in which the most important parameters assumed different numerical values, and the results were checked to see that they make physical sense. The mesh size was varied 50% up and down from the nominal value, and the surface temperature readings changed by no more than ±0.3K at individual surface stations. Other parameters included: the wood physical properties, the heating rate, and the duration of the experiment.

Finally, it will mentioned that only the forward half of the plate was scanned by the IR imaging camera and therefore only that part of the temperature distribution could be compared with the computed results. Therefore, the treatment of the upper and lower trailing edges as well as the base was irrelevant to the present purpose. Consequently, the adjustable factor C_{corn}, in the respective functions (B.11), (B.15) and (B.18), that was intended to provide a smooth temperature transition between the trailing edge and the base), was arbitrarly set equal to one.

VITA

Ehud Gartenberg is a graduate of the Technion, Israel Institute of Technology in Haifa, Israel where he got his B.Sc and M.Sc. degrees, both in Aeronautical Engineering. He has eleven years of experience in wind tunnel, ground and flight testing of aerodynamic configurations and propulsion systems. His research focused on developing and introducing new and unproven experimental methods for application in aerodynamic and fluid mechanics research. He has published nine papers in journals and proceedings of international conferences and congresses.